Doctoral Dissertation
Doctoral Program in Materials Engineering (29th Cycle)

Physico-Chemical properties of hybrid organic/inorganic nanotubes of imogolite type

By

Elnaz Bahadori

******

Supervisor (s):
Prof. B. Bonelli

Doctoral Examination Committee:
Prof. D. P. Debecker. , Referee, Université catholique de Louvain (Belgium)
Prof. A. Vicente, Referee, Université de Caen, CNRS (France)
Prof. S. Esposito, Università degli studi di Cassino e del Lazio Meridionale (Italy)
Prof. F. Savorani, Politecnico di Torino (Italy)
Prof. S. L. Fiorilli, Politecnico di Torino (Italy)

Politecnico di Torino
2016

Declaration

I hereby declare that, the contents and organization of this dissertation constitute my own original work and does not compromise in any way the rights of third parties, including those relating to the security of personal data.

Elnaz Bahadori

2016

* This dissertation is presented in partial fulfillment of the requirements for **Ph.D. degree** in the Graduate School of Politecnico di Torino (ScuDo).

I would like to dedicate this thesis to my lovely family

Acknowledgment

First of all, I would like to thank my supervisor, Prof. Barbara Bonelli for all her supports, helps, kindness and patience during the past three years. I am very grateful for so many things that I learned from her. My sincere thanks also go to Dr. Marco Armandi for always being my guide in different theoretical and experimental aspects of my work. Further, I would like to thank Dr. Serena Esposito for helping me kindly during my work in polytechnic university of Turin.

I would like to thank all the members of the Laboratory of Inorganic Chemistry (LAC) in ETH University of Zürich for their helps with different characterization techniques. I specially thank Prof. Dr. Hansjörg Grützmacher for giving me the possibility to work in his laboratory (LAC-ETH) as a research scholar for 6 months, during my PhD research. A special thank to Dr. Thomas Gianetti, whom I learn a lot from in both theoretical aspects and also laboratory skills in ETH of Zürich.

I would also like to thank Prof. Diana Sannino, for all her supports in my research about photocatalysis that I obtained in their laboratory in University of Salerno as a research scholar for one month. Special thanks to Dr. Vincenzo Vaiano from University of Salerno, for all his help and time that he allocates for me day and night, in the past and also in present even from far.

Abstract

In the beginning of 1950s [1, 2], the usage of microscopic and spectroscopic methods allowed the identification of nanosized tubular clay minerals, such as halloysite, chrysotile and imogolite. However, the concept of nanosized tubular clay minerals was not so popular and a few papers were only published on this topic. After the first observation of carbon nanotubes (CNTs) in 1991 [3], the interest for nanosized tubular clay minerals, which could be synthesized besides being present in nature, was renewed.

Nanosized tubular clay minerals, as their name implied, are tubular nanostructures clay minerals with dimensions in the 1 - 100 nm range [4, 5] and a hollow tubular structure. So far, among all clay minerals both halloysite and imogolite have attracted more attention for their applications in fabrication of clay polymer [6] nanocomposites [7], catalysis and adsorption [8, 9]. The reason for their popularity is attributed to their unique, one-dimensional tubular structure and properties, which are modifiable by altering the internal and external surfaces [9-11].

Proper imogolite is a hydrous aluminum silicate with chemical formula $(OH)_3Al_2O_3SiOH$ [2, 12], occurring as single walled nanotubes (NTs) with Al(OH)Al and Al-O-Al groups at the outer surface, and silanols (SiOH) at the inner one. This thesis is aimed at assessing the catalytic behavior of the hybrid organic/inorganic analogue of imogolite, *i.e.* methyl-imogolite (MeIMO, $(OH)_3Al_2O_3SiCH_3$), with an inner surface lined by $Si\text{-}CH_3$ groups (hydrophobic) and an outer surface resembling that of imogolite (hydrophilic). The special structure of MeIMO leads to enhanced adsorption properties that render it suitable for gas separation/storage [9]. Furthermore, MeIMO NTs have higher degree of long range order [13], higher production yield, larger pores (> 0.2 nm) and surface area (~ 600 $m^2.g^{-1}$) with respect to proper imogolite [9].

Modification of the outer surface of MeIMO NTs includes either formation of covalent bonding or electrostatic interaction. The former is achieved by the reaction of MeIMO with organosilanes [11], whereas the latter is possible due to the

protonation of outer surface of NTs in water, which leads to charge matching between a proper counter-ion and the outer surface of NTs [14]. These specific properties may be exploited in several applications, mainly for removal of organic pollutant from water by the electrostatic interaction of anion/cations with the charged surface of NTs [15-19].

The second topic of this work concerns another modification of the outer surface by isomorphic substitution (IS) of octahedral Al^{3+} in the outer surface by Fe^{3+}. Fe-doped MeIMO was obtained by both ionic exchange (IE) and direct synthesis (DS) method with two Fe contents, i.e. 0.70 wt.% (Fe-0.70-MeIMO) and 1.4 wt% (Fe-1.4-MeIMO). Although IS of Al^{3+} by Fe^{3+} is a common process in almost all natural alumino-silicates, little is known about Fe doped imogolite NTs. Several studies have been recently performed dealing with the synthesis, surface characterization and applications of Fe doped imogolite NTs. So far, no specific study has been devoted to the surface properties of Fe-doped MeIMO NTs, nor to their application as heterogeneous catalyst.

The presence of Fe^{3+} in the structure of NTs induces new chemical and solid state properties. Based on theoretical calculations on Fe-doped imogolite NTs, IS of Fe for Al may create "defective sites" both inside and outside NTs, and reduce the band gap of imogolite (an electrical insulator) from 4.7 eV to 2.0-1.4 eV [20]. On the other hand, the first experimental studies, mainly due to Ookawa and later to Shafia *et al.*, indicate that NTs are preserved up to 1 wt % Fe isomorphically substituted in the NTs. Higher Fe contents lead to the unavoidable formation of iron oxo-hydroxides particles/clusters [21-24].

This study confirms that in Fe-doped MeIMO as obtained by both IE and DS methods, Fe^{3+} species in the NTs structure decrease the band gap of MeIMO from 4.9 to 2.4 eV. Moreover, with 1.4 wt % Fe, some Fe_xO_y oligomeric clusters and Fe_2O_3 particles are forming. Decreasing the Fe content to 0.7 wt % shows that isolated Fe^{3+} species are more abundant by DS method, whereas by ionic exchange Fe tends to form more oligomeric iron oxo/hydroxide clusters or Fe_2O_3 particles. This particular behavior of Fe-doped MeIMO could help one to choose the proper method for specific application.

The thermal stability of MeIMO and Fe-doped MeIMO NTs has also been studied. Mechanisms of collapse of NTs (at T > 300 °C dehydroxylation and NTs deformation result in collapse of structure) have been investigated with samples at different Fe loading and also in different heating environment (either in air or in vacuum). According to the obtained results, thermal treatment in air results in the faster cleavage of MeIMO NTs by burning the inner methyl groups to CO_2.

Whereas, thermal treatment in vacuum, triggers the cleavage of NTs from another route which is detectable by more positive chemical shift in ^{29}Si MAS NMR analysis.

Although the wall structure of collapsed samples is partially damaged or disordered, and finally collapsed at around 400 °C, the phases stemming by the thermal collapse of NTs show considerably high surface area and high porosity, due to residual microporous regions likely derived from unaffected pristine NTs within the layers [25]. Furthermore, the analysis of IR spectra of pyridine adsorption on collapsed samples show the presence of strong Lewis/Brønsted acidic sites.

Another interesting aspect is the deformation of NTs due to dehydroxylation, which may lead to the alteration of light adsorption capacity and to the reduction of band gap in deformed NT with respect to original one. This has been investigated by theoretical calculation (SCC-DFTB) of dehydroxylated imogolite NTs [26]: in the literature, it has been observed by practical band gap evaluation obtained by UV-Vis spectroscopy on MeIMO NTs. Therefore, the dehydroxylated imogolite or MeIMO NTs is considered as a semiconductor and controlling the degree of dehydroxylation in the heat treatment process may open the possibility to adjust and control the electronic and mechanical properties of NTs. All these observations trigger the future investigations on the different structural phases arrived from thermal treatment of NTs.

In order to investigate the photocatalytic application of Fe-doped MeIMO NTs, the samples obtained by IE method have been studied for the photo-Fenton oxidation of tartrazine dye, an important pollutant of both wastewater and groundwater.

The obtained results imply that IS of Al^{3+}/Fe^{3+} at low Fe content (i.e. 0.7 wt. % Fe) starts the photo-Fenton process and provides total discoloration and mineralization of tartrazine dye. Whereas, at higher Fe content (i.e. 1.4 wt. % Fe) the higher amount of Fe oxo-hydroxide clusters play a detrimental effect on tartrazine mineralization, due to both a lower photo-Fenton activity of the clusters with respect to isolated Fe^{3+} species and their ability to catalyze the (undesired) decomposition of H_2O_2 to oxygen and water. Remarkably, Al-OOH groups at the outer surface of bare MeIMO also enhance the photocatalytic activity towards the dye mineralization.Tartrazine removal was studied also in the presence of the buckled phases stemming from NTs thermal collapse. The results were interesting and show the high dye adsorption and degradation in the presence of collapsed phase, mainly due to new coordination environments for both Al and Fe sites, leading an active site towards the photo-Fenton reaction.

Contents

List of Figures

List of Schemes

List of Tables

Chapter 1

Physico-chemical Properties of Imogolite-Type Nanotubes

1.1 Introduction

Nanotubes (NTs) have attracted significant attention in the last decades, due to their specific physical properties, which are a combination of their nanoscale dimension, hollow cylindrical form, structure, porosity and composition. These specific aspects allowed to consider their use as building blocks in several applications for nanostructured assemblies, *e.g.* high strength nanocomposites, field emitting surfaces, electrode materials, sensors, nano transistors, and energy storage devices [28-30]. Discovery of carbon nanotubes (CNTs) in 1991 by Iijima [3] has opened a new horizon in a world of science and technology, due to their particular properties and application in electronics, composite materials, electrochemistry and molecular separations [31-37].

Despite such attractive properties, several intrinsic limitations of CNTs inhibit their application, such as high temperature process with low product yield [38-40], their color limits their applications as nano fillers in transparent hybrid materials [41], low compatibility in bio-applications, some negative environmental aspects, potential toxicity [41, 42], and the difficulty in the surface functionality [43, 44].

The existing barriers facing the use of CNTs encouraged the research for analogue structures among inorganic materials, especially metal oxide NTs, with a lower synthesis cost and mild synthesis conditions (usually hydrothermal or

solvothermal), higher surface reactivity (similar to a metal oxide/hydroxide), higher flexibility for surface modification, and controllable dimensions (the average length in the ~20-500 nm range) for better performance in fabrication of thin membranes [45, 46].

Two inorganic NTs namely imogolite NTs [12] and halloysite NTs [47] with the single-wall structure, have been rise attentions in the last years. Imogolite NTs with unique and attractive properties for molecular adsorption and membrane formation, controllable and monodisperse dimensions [48, 49], high hydrophilicity [8], and fast mass transport (*e.g.* for water and alcohols) [50, 51], show a potential application in different fields of science and technology. The inner surface of the aluminosilicate SWNT contain silanol (Si-OH) groups and can be expected to resemble those of metal oxide/hydroxide and silicate materials. Therefore, potentially can be functionalized in a manner analogous to the well-known techniques for functionalization of mesoporous and microporous silicas [52-55]. On the other hand, the hydroxyl groups at the external surfaces of aluminosilicate SWNTs may possess good affinity to hydrophilic polymers [56], which could open the possibilities for producing NTs/polymer membranes.

1.2 Nanosized tubular clay minerals

Nanosized tubular clay minerals, as the name implies, are clay minerals with tubular hollow nanostructure with a length varies from 1 nm to several microns [4]. In the beginning of 1950s, the structure of nanosized tubular clay, such as halloysite, imogolite and chrysotile [2] have been identified, using several analytical techniques.

Halloysite is a dioctahedral clay mineral with Al:Si ratio 1:1 as depicted in Scheme 1-1 [57]. Gibbsite octahedral sheet, $Al(OH)_3$, comprises the main framework of the halloysite NTs. The outer surface of the this sheet can be modified by siloxane groups yielding $Al_2Si_2O_5(OH)_4 \cdot nH_2O$ [57]. Tubular halloysite varies in length from the submicron scales to several microns, even > 30 μm [57, 58], and the external diameter ranging approximately from 10 to 100 nm [59, 60]. The outer surface of halloysite is formed by Si-O-Si groups and bears a negative charge at pH 6 – 7, while the inner cylinder core is related to Al_2O_3, and is slightly positively charged [61].

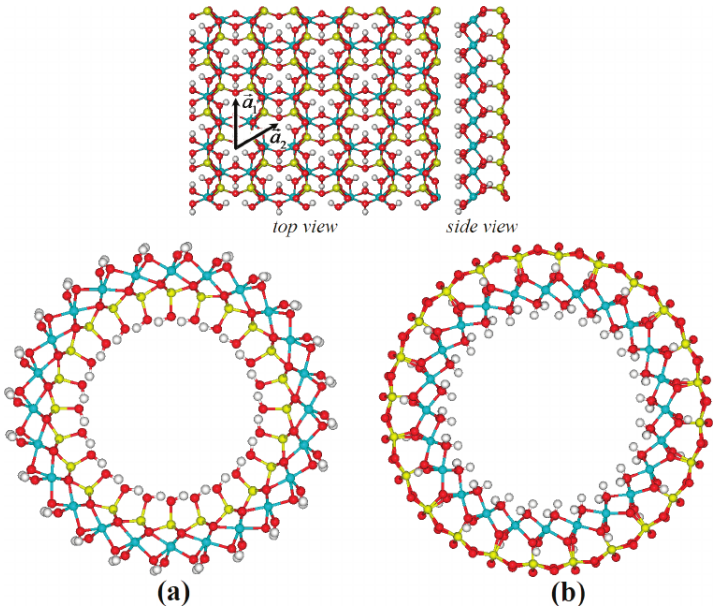

Scheme 1-1: Monolayer structure of halloysite and cross section views of (a) a (12,0) imogolite NT and (b) a (12,0) halloysite NT. White atoms are H, red O, blue Al, and yellow Si (41)

Imogolite consists of single walled aluminosilicate nanotubes with an inner diameter of approximately 1.0 nm, which naturally occurs in weathered volcanic rocks soils. The NTs consist of curved gibbsite sheets, in which the $(SiO_3)OH$ groups substitutes the inner hydroxyl surface of gibbsite sheets [62].

Chrysotile is another clay mineral, which is normally transformed through hydrothermal alteration process from ultra-basic rock forming minerals, like olivines. Chrysotile is in fact a hydrous magnesium phyllosilicate with chemical formula $Mg_3(OH)_4Si_2O_5$ [63], and consist of SiO_2 and $Mg(OH)_2$ layers. The octahedral $Mg(OH)_2$ groups form the outer surface of the tubes and the SiO_4 groups are located in the inner part [64]. The inner diameter of NTs varies from 7-8 nm and the outer diameter from 22-27 nm [65].

1.3 Imogolite-type NTs

Imogolite is a hydrated aluminosilicate clay mineral with a fibrous structure with the Al:Si atomic ratio of 2:1 and chemical formula of $(HO)_3Al_2O_3SiOH$ (Scheme 1-2). The name “imogolite” was first used by Yoshinaga and Aomine in 1962 [12] for a constituent present in the clay fractions of the soil (“imogo”) found in glassy volcanic ash (Figure 1-1).

From the 1970s an intense research activity in this subject was carried out by V.C. Farmer and others [66-70], in order to find the molecular structure and properties of imogolite. Based on their results, imogolite results to be a paracrystalline mineral, which appears as long thread- or fiber-like structures and may be from 400 nm up to several microns long with a constant inner diameter of 1.0 nm [8, 71]. The outer diameter is *ca.* 2.0 nm in natural imogolite, whereas it varies around 2.5-2.7 nm in synthetic samples, due to the presence of different inter-tubes impurities [2].

In 1972, Cradwick *et al.* [2] presented a structural analysis of imogolite. According to their analysis, the imogolite NTs consist of orthosilicate groups at the inner surface, while the outer surface consists of gibbsite units (Scheme 1-2) [8]. The tubular structure of imogolite was initially explained by the connection of larger octahedral sites in the gibbsite sheet with the smaller silicon tetrahedron: this misfit in size causes a contraction of the gibbsite sheet, in which the O-O distances between two shared oxygens shorten to less than 3 Å. This change in geometry causes the gibbsite sheet to curl and form a tube. Bridged hydroxyl groups Al-OH-Al are found on the outer tube walls, whereas the inner tube surface consists of ≡Si-OH groups [2].

There are two possible distances between SiOH groups inside the NTs, one between two SiOH within the same circumference (the distance 0.25 nm), the other between two SiOH of two adjacent circumferences (the distance 0.44 nm) (Scheme 1-2). This aspect leads to high SiOH density in imogolite structure, which is twice the average density of SiOH groups at the surface of hydrated amorphous silica [8]. The high hydrophilicity of inner surface of imogolite hinders the diffusion of species within inner cavity, such as catalyst and adsorbents; therefore a primary dehydration step is always required in order to remove the inner surface adsorbed water molecules.

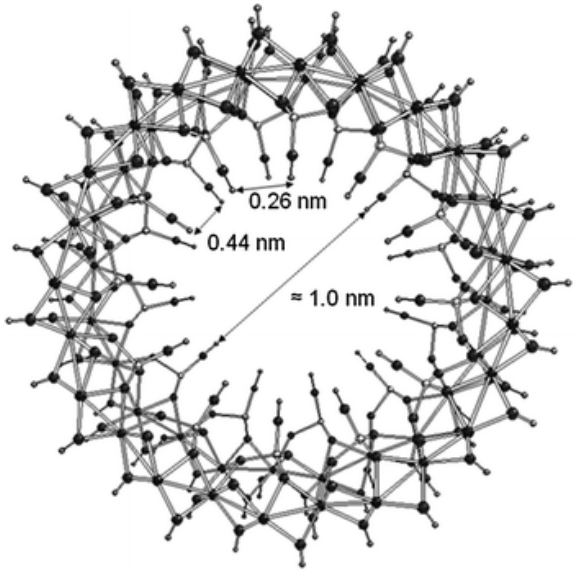

Scheme 1-2: Section view of imogolite NT with 1.0 nm the inner diameter of A pores and two possible circumferences, both containing 12 imogolite units: the calculated distance are: (i) the 0.44 nm, the distance between two SiOH groups of two adjacent circumference, (ii) the 0.26 the distance between two SiOH in the same the circumference [8]

TEM micrographs (Figure 1-1) have shown that imogolite NTs arrange in bundles with nearly hexagonal packing. Tubes tend to aggregate with different degrees of order and are rarely found in isolated units [72-75]. Furthermore, the number and dispersion of bundles appears to be pH dependent [76, 77]. Consequently, due to particular network, imogolite NTs, reflect 3 different kind of porosities [78, 79] and surfaces, as reported in Scheme 1-3 [80]:

(i). pores A are intra-tube pores with 1.0 nm diameter, lined by silanols, which are very hydrophilic and able to interact with H_2O, NH_3 and CO [80, 81];

(ii). pores B are inter-tube spaces with very small dimensions (0.3-0.4 nm wide) among three aligned NTs within a bundle, and hardly accessible to even small molecules like water [8, 78].

(iii) pore C are slit mesopores among bundles and can interact with larger molecules, like phenol [8] and 1,3,5-triethylbenzene [80].

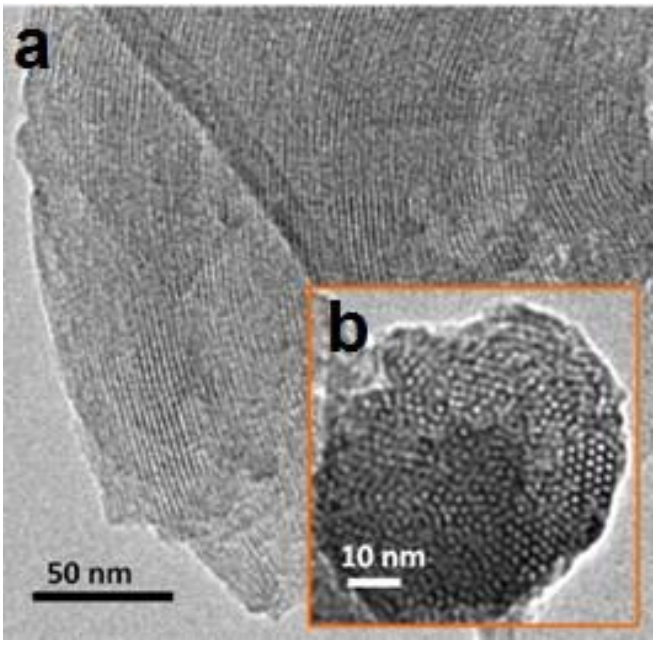

Figure 1-1: HRTEM images of an IMO bundle formed by parallel NTs (a) forming a hexagonal array (b) [23]

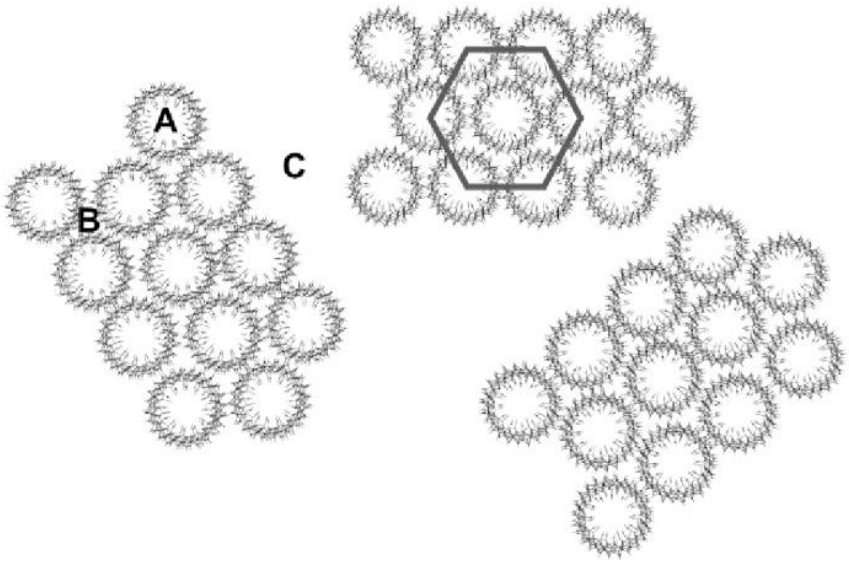

Scheme 1-3: imogolite NTs hexagonally packed in bundles. The cell parameter "a", corresponds to the distance between the centers of two NTs within a bundle. Pores A, B and C correspond to proper imogolite nanopores (Φ=1.0 nm); pores among three aligned NTs (Φ=0.3 nm) and (disordered) slit mesopores between bundles, respectively [82]

The particular structure of imogolite leads to a high surface area (250-800 m^2 g^{-1}) [83] and the high anion adsorption capacity, due to the outer gibbsite groups that is positively charged in water in a wide range of pH. Because of this, the outer surface of imogolite, in its pure form, has a net positive charge below pH 10 [23, 84, 85], which favors the adsorption of anions in the 'natural' pH range.

1.4 Allophane: a poorly crystalline aluminum silicate clay (proto-imogolite)

Allophane is a non-lamellar aluminosilicate, which is a product of the weathering or hydrothermal alteration of volcanic glass and feldspars [83, 86]. The chemical structure of allophane was long unknown, since being non-crystalline could not be detected by X-ray diffraction techniques [87], although chemical analysis showed the presence of aluminum (Al), silicon (Si), oxygen (O) and hydrogen (H).

Imogolite was differentiated from coexisting allophanes on the basis of its dispersion characteristic in warm dilute alkali solution, in which it proved more resistant than the allophane impurities. Further, X-ray diffraction analysis of imogolite showed several broad intense lines and electron microscope investigations visualized the presence of threads with dimension between 10 and 20 nm.

Allophane is the short-range-order group of clay-size minerals, which contain water, alumina and silica [88]. The structure of allophane has a spherical or ring-shaped morphology with a diameter of 4–5 nm. XRF, NMR and XPS studies have affirmed that aluminum occupies different structural sites: octahedral, tetrahedral and even pentahedral. In natural allophanes, the total ratio of Al_{VI}/Al depends on their composition and decrease with decreasing Al/Si ratios [89-93]. Allophane are categorized in three types:(i) the aluminum-rich allophanes with a Al/Si ratio of about 2 and the same structure as imogolite; (ii) the silicon-rich allophanes, with the Al/Si ratio of about 1 and contain polymerized silicate; (iii) and the stream-deposit allophanes, whit the Al/Si ratios of 0.9–1.8, that Al substitutes for some Si in the polymeric tetrahedral [94].

The coordination of Al in allophanes structure is different from imogolite, since a significant proportion of the Al is in tetravalent coordination [88, 95]. Therefore the surface of allophane is permanently negative charged. The Al-rich, or 'proto-imogolite' allophane, has a chemical structure which defines as 'fragments of imogolite tubes' with the Al : Si ratio is normally between 2 and 3 [83, 88]. The higher Al : Si ratio in allophane with respect to the imogolite is due to the

substitution of the O_3SiOH tetrahedra of the inner surface with hydroxyls groups [83, 88]. This substitution results in the formation of small (4 - 5.5 nm thick) spherules structures instead of fibers (Scheme 1-4 and Figure 1-2) [83].

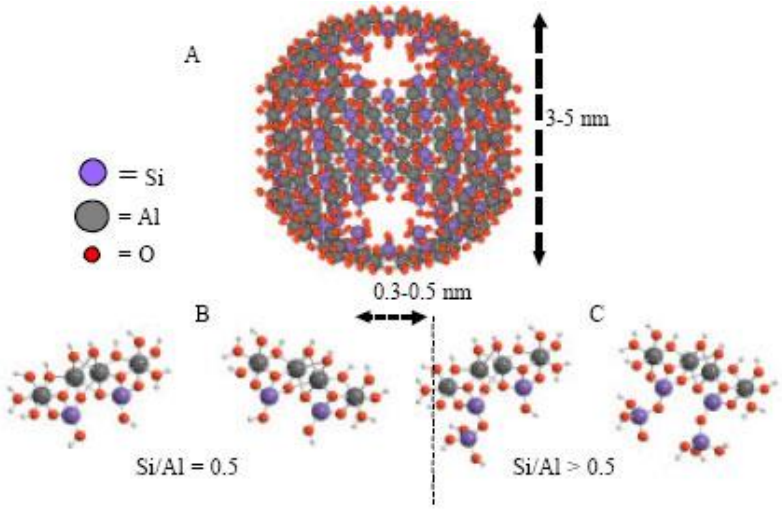

Scheme 1-4: Chemical structure of nano-ball allophane (A) Full structure, (B) and (C) Atomic arrangement in cross section at pore region [96]

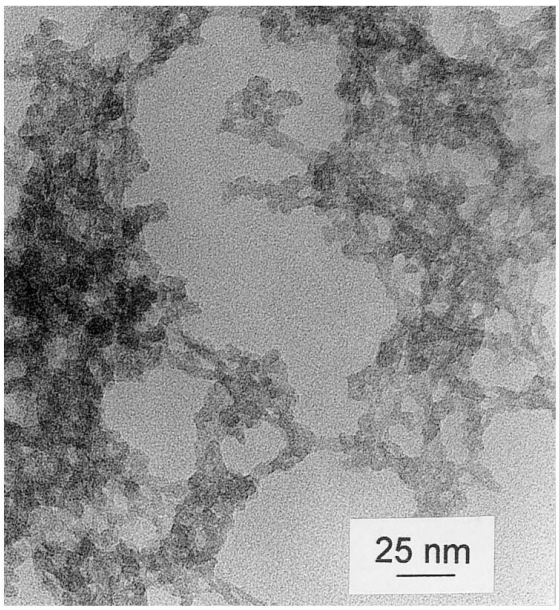

Figure 1-2: HR-TEM photograph of synthetic allophane with Al:Si=2, associated in fractal aggregates [97]

1.5 Mechanism of formation of imogolite

The basic structure of imogolite structure consists of gibbsite sheets with orthosilicic acid groups. The synthesis of imogolite NTs involves a simple hydrolysis step followed by a growth step at 95 °C - 100 °C [98]. However, the phenomenology and mechanism of the formation of imogolite NTs are still not well-understood. Two different mechanisms are hypothesized in the literature: the former claims kinetic aspects to drive the formation; the latter emphasizes the role of a self-assembly process under thermodynamic control.

In the first mechanism, the formation of a precursor is expected to take place at an early stage of the reaction, providing a number of nuclei that induce the development and the growth of NTs by polymerization. NTs length, which is monodisperse during all synthesis process, would therefore increase substantively with synthesis time and by constant addition of growth units to the end of NTs [48].

Conversely, in the self-assembly process, the proto-imogolite clusters formed at the initial stage are considered as building blocks of the NTs structure. Therefore NTs with the specific dimensions are expected to self-assemble (Scheme 1-4). In this mechanism, the formation of proto-imogolite clusters is highly dependent on factors that influence the thermodynamic equilibrium, such as concentration of the precursors and/or temperature.

In order to understand the mechanism of formation of imogolite NTs, several studies have been done on the mechanism of self-assembly of aluminogermanates as a model.[99] The corresponding results imply that the Al atoms are hydrolysed and polymerised, and form the structure similar to gibbsite. The driving forces of tubular imogolite formation is the minimum strain energy relaxation caused by the Al−O and Si−O bond distance variation when the hydroxyl groups at the surface of gibbsite are substituted by SiOH groups to generate proto-imogolite clusters, and hydrogen-bonding networks [100]. Based on MAS-NMR and FTIR analysis done by Lee *et al.* [101] the size of the NT diameter is directly depends on SiOH substitution which is, in turn, influenced by the temperature [99, 101, 102].

The formation energy of imogolite NTs from 2D planar gibbsite sheets is endothermic (43.45 Kcal mol^{-1}); therefore, by increasing the synthesis temperature, SiOH substitution increases; consequently, the diameter of imogolite NTs increases [101]. (Scheme 1-5) However, the optimum temperature range to obtain imogolite in few days is in the range of 95-100 °C [98, 103]. For instance, it needs 7 years for the synthesis of imogolite with a diameter close to the natural ones at 25 °C [104].

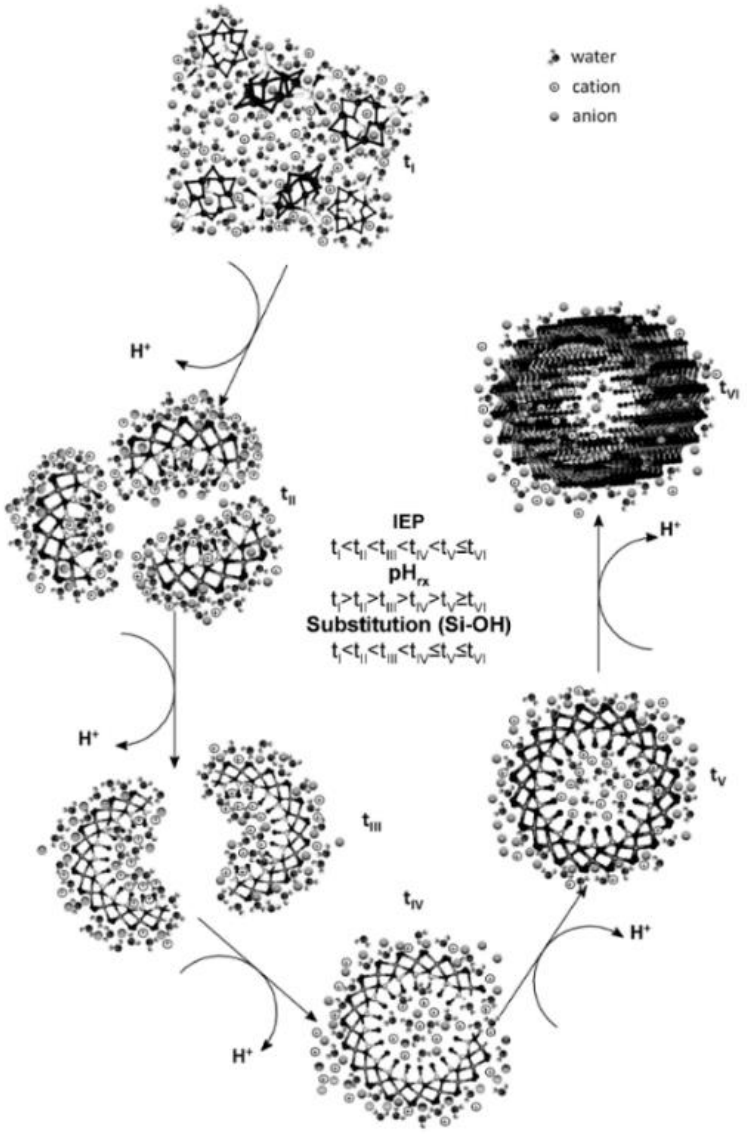

Scheme 1-5: Structural evolution of the precursors formed during the synthesis of imogolite [105]

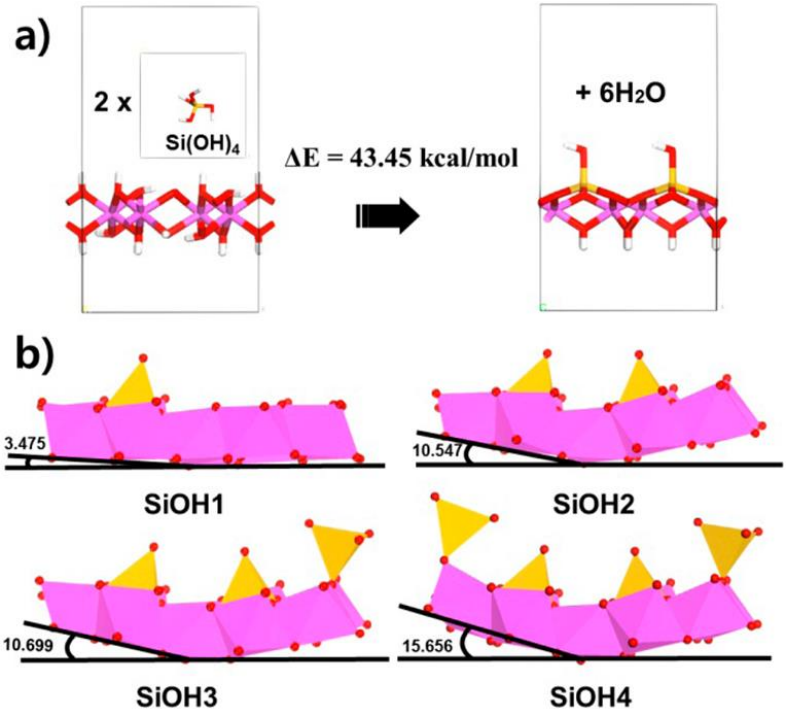

Scheme 1-6: (a) Formation energy of two dimensional planar gibbsite-like imogolite from a planar gibbsite sheet, 43.45 kcal mol^{-1}, and (b) curvature of proto-imogolite clusters based on the degree of substitution of silanol group. Increasing in the curvature from 3.48° to 15.66° by an increase in the number of silanol groups [101]

The Nair's group reported that the shape of proto-imogolite clusters can be controlled by anionic ligands, and that the proto-imogolite cluster shape is directly related to the diameter of the NTs [49]. According to their research, binding of different types of anionic ligands to proto-imogolite clusters resulted in alteration of cluster curvature, which may affect the final shape and arrangement of the aluminosilicate NTs [49].

Farmer and Fraser [106] found that during imogolite formation from proto-imogolite, pH drops from 4.5 to 3.0 and explained this finding by the formation of -Al-O-Al- bridges that favor the loss of a proton (Scheme 1-6). Nevertheless, addition of anions such as chloride or very weak bases significantly inhibits the formation of imogolite [106], which suggests that strong ion-pairing prevents the intramolecular reaction.

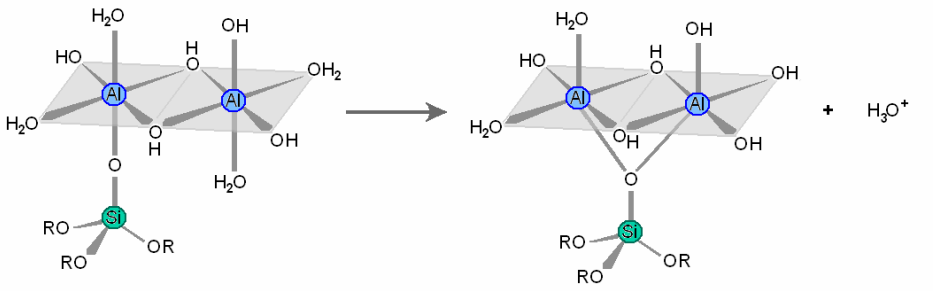

Scheme 1-7: Formation of an -Al-O-Al- bridge that favors the loss of a proton [106]

1.6 Modification of imogolite NTs

In order to increase the technical applications, several modifications have been proposed on synthetic materials. Consequently, an outer-surface modification on NTs could increase their compatibility with solid- or liquid-phase, such as nano-composite; whereas the inner-surface modification enhances the surface reactivity, which would be advantageous for shape/size selective separations and catalysis.

Imogolite NTs modification of inner and outer surface is possible in mild conditions, and provides an opportunity to enhance reactivity and alter the hydrophilicity, pore structure and electrical conductivity [107]. However, physisorbed water, especially in the inner surface of NTs due to the high surface silanol density (~9.1 OH/nm^2) may interfere the functionalization process [8, 108, 109].

All kind of modifications of imogolite NTs can be applied by two main procedure: direct synthesis modification and post synthesis modification.

1.6.1 Modification of inner pores of imogolite NTs

In imogolite NTs, the small dimension of inner pores (*ca.* 1.0 nm), combined with high hydrophilicity, hinders the accessibility of small probes molecules, such as CO, CO_2, NH_3, unless NTs are dehydrated in the 270 °C-300 °C temperature range. Therefore, obtaining a larger inner pores dimension with less hydrophilicity is considered as one of the main targets, which can be achieved by either direct synthesis or post synthesis method.

1.6.1.1 Direct synthesis method

Direct synthesis methods are based on changing the silicon precursor in the syntheses bath. Therefore, Si atoms can be replaced by other atoms, like Germanium [81, 110], or the hydroxyl groups can be replaced by organic

functionalities [9]. Consequently, direct synthesis methods open a possibility to modify inner surface of NTs and changing the hydrophilicity, polarity and size of A pores.

Germanium-imogolite ($OH_3Si_{1-x}Ge_xOH$) is an example of imogolite type NT, in which silicon atoms are replaced by germanium atoms, partially or totally, by means of germanium precursors like tetraethoxygermanium (TEOG) or germanium tetrachloride ($GeCl_4$) [81, 111, 112]. Germanium-imogolite may appear as both SW and double-walled (DW) NTs [110, 113, 114]. By increasing Ge substitution, the diameter (3.3 nm) increases, whereas the NTs length decreases in that even NTs with 20 nm length can be synthesized [81, 111, 112]. This material has a high potential in artificial ion channel devices, due to hydrophilic interior surface combined with the short length of NTs [111].

Another successful example of inner surface modification of NTs and the alteration of hydrophilicity was obtained with the substitution of silicon precursor with an organosilane (*e.g.* triethoxymethylsilane). This modification introduces a new imogolite type material, named methyl-imogolite (MeIMO), which was synthesized for the first time by Bottero *et al.* [9]. Methyl-imogolite has a chemical composition of $(OH)_3Al_2O_3SiCH_3$, with completely hydrophobic inner surface, lined by methyl groups and theoretically unmodified outer surface same as imogolite one. Furthermore, the inner diameter of NTs increase (*ca.* 2.0- 2.5 nm) due to substitution of larger methyl groups instead of hydroxyl groups; therefore, the size of B pore increases respectively. The larger B pores increase the accessibility for adsorption of probe molecules like ammonia and CO_2 [107, 115]. MeIMO has simple synthesis procedure and higher yield, with respect to imogolite.

Recently, Kang *et al.* [116] synthesized new imogolite type material with synthesis precursor namely $(CH_3CH_2O)_3$-Si-CH_2-NH_2 (Aminomethyl triethoxysilane, AMTES) in which the inner Si-OH groups have been replaced by Si-CH_2-NH_2 up to 15 %. The new synthesized material are named ANT, which refers to "amine functionalized NT". The new synthesized material has a shorter tubes length (average length *ca.* 50 nm) as observed by TEM analysis (Scheme 1-7). Amino methyl substitution resulted in loss of micropores surface area, due to larger amino methyl groups with respect to SiOH groups (38.1 $Å^3$ with respect to 16.9 $Å^3$ estimated by atomic van der Waals radii). Besides, amino groups positively affect the selective adsorption of carbon dioxide from both CO_2/CH_4 and CO_2/N_2 mixtures [116].

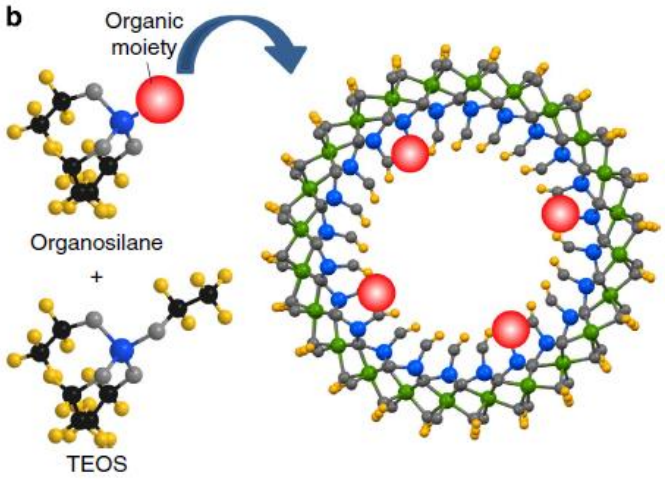

Scheme 1-8: Forming NTs by incorporation of the organic moieties in the inner surfaces, using a mixture of TEOS and a designed organosilane [116]

Amara *et al.* (2015) [117] introduced a new hybrid imogolite with the composition $(OH)_3Al_2Si_{1-x}Ge_xCH_3$ in which the chemical composition of the A pores has been changed by using the mixture of TEMS and triethoxymethylgermane (TEMG) to a solution containing Al precursor and acidified with $HClO_4$. Varying the amount of TEMG precursor allows controlling the inner diameter of the final material.

1.6.1.2 Post synthesis methods

For post synthesis modification of inner pores, it is mandatory to carry out a proper dehydration of the material in order to remove molecularly adsorbed water. Thermally, this occurs at 270 °C-300 °C. Furthermore, the small dimension of the inner pores (*ca.* 1.0 nm), limits the size of organic linker for entering the A pores [10].

The unique example of the inner pores modification by post synthesis method had been done by Kang *et al.* (2011) [10], by grafting organic functionalizer on well dehydrated imogolite NTs in the inert atmosphere of glove box with the continues stirring for 24 h. The functionalizing reagent R (acetyl chloride, trimethylmethoxysilane or trichlorosilane) was added in the molar ratio R: imogolite hydroxyl group = 2:1. The new material had a smaller inner pore volume due to larger molecular dimension of functionalizing reagent. Furthermore, organic groups decreased the hydrophilicity of inner pores [10].

1.6.2 Modification of the outer surface of imogolite NTs

Outer surface functionalization of imogolite NTs improves their application in the field of clay polymer nanocomposites [118], transparent films [119], films of aligned NTs [14]. In order to enhance the surface compatibility with organic solvents, for the applications of imogolite in polymer nanocomposites, hydrophobization of the outer surface of NT is mandatory [118]. Furthermore, isomorphic substitution (IS) of transition metals like iron (Fe) instead of Al in the outer surface, may decrease the bandgap of material, for applications in catalysis and photocatalysis [21, 22, 24, 85].

In general, the modification of the outer surface of imogolite NTs reported so far could be divided into three categories: (i) grafting with 3-APTES (3-aminopropylsilane, NH_2-$(CH_2)_3$-$Si(OEt)_3$), the most common organosilane for the modification of oxides [120, 121]; (ii) functionalization with alkylphosphonic acid; (iii) isomorphic substitution of Aluminum with Fe^{3+} ions. The latter is a unique modification, which can be obtained by both direct synthesis and post synthesis method [21-24].

1.6.2.1 Post synthesis modification of outer surface of imogolite NTs

The first outer surface modification was reported by Johnson and Pinnavaia, who in 1990 employed 3-APTES in water acidified by acetic acid [122]. The acidic condition allows a very good dispersion of imogolite NTs due to the positively charged outer surface, as well as fast and complete hydrolysis of 3-APTES and inhibition of polymerization. The physico-chemical characterization of the material (by FTIR spectroscopy and solid state NMR) confirmed the outer surface functionalization. The main limitation was the instability of 3-APTES monomers in aqueous solution. Later, the same authors reported that the functionalizing indeed was not limited to the outer surface only, but also involved to a certain extent the inner surface of NTs [120]. At the beginning of the process, 3-APTES species grafted at the outer surface of NTs, then grafting of 3-APTES moieties at the inner surface also occurred. The presence of SiOH groups at the mouth of NTs may result in the partial functionalization of a proportion of inner surface. Therefore, in order to avoid this process, having the inner hydrophobic surface is critical.

Later Qi et l. in 2008 [121] and Zanzottera *et al.* in 2012 [11], reported grafting of 3-APTES on imogolite and methyl-imogolite in toluene respectively, in order to prevent undesired hydrolysis. In the case of imogolite, NTs reacted with 3-APTES

leading to a material named Imo-APTES. Subsequent immobilization of osmium tetroxide (OsO_4) on the outer surface of Imo-APTES introduced a new material named Imo-APTES-OsO_4, which showed a good catalysis behavior in droxylation of olefins including the reaction of olefins with chiral ligands trough asymmetric dihydroxylation [121].

In the case of MeIMO, due to stability of inner Si-CH_3 bonding toward hydrolysis, no hydrolysis and subsequently no reaction with 3-APTES was observed. By full functionalization of MeIMO surface the nominal chemical composition of the new material should be NH_2-$(CH_2)_3$-$Si(O)_3Al_2O_3SiCH_3$. However, Zanzottera *et al.* [11] chose instead one-third of the content of 3-APTES, which corresponds to the functionalization of all Al(OH)Al groups (Scheme 1-8). They claimed that using lower amount of 3-APTES prevents the condensation of 3-APTES molecules and formation of undesired phases. Furthermore, due to specific structure of imogolite NTs, probably not all the external Al(OH)Al groups (*e.g*, those within B pores) may react with 3-APTES. Therefore, even with lower loadings, the aminopropyl groups are likely to cover the all surface. MeIMO-NH_2 showed a moderate increase in thermal stability and lower surface area (450-530 $m^2\ g^{-1}$) with respect to imogolite, as well as the ability to react with CO_2 and forms carbamates [11].

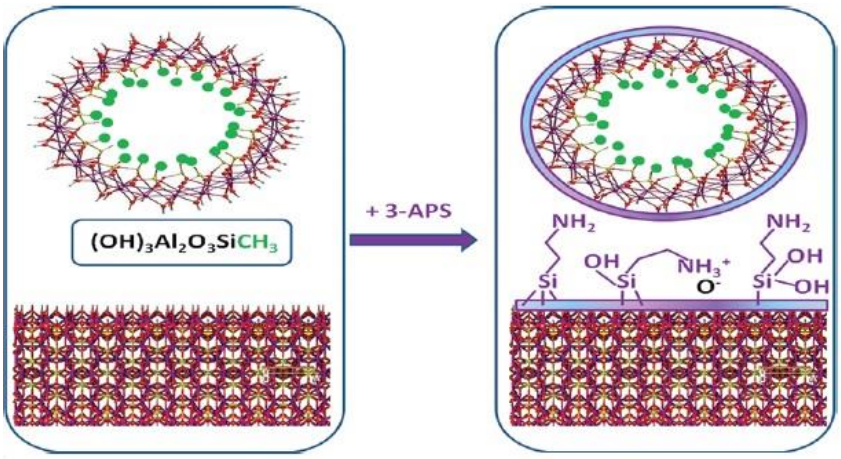

Scheme 1-9: Functionalization of MeIMO with 3-APTES in toluene leads a material bringing three kinds of groups in the outer surface [11]

In 2005, Yamamoto *et al.* [119] reported the successful modification of the outer surface of imogolite by using alkyl phosphonic acid in hydrophobic solvents such as hexane and chloroform. Phosphoric acid groups show strong interaction

with Al–OH groups in the outer surface and the acidic pH provides a good dispersion of NTs in the solvent (Scheme 1-9).

Park *et al.* (2007) [14] report another example of phosphoric acid groups for producing the two dimensional imogolite composite material by reaction between either octadecyl phosphonic acid (ODPA) or tetradecyl phosphonic acid (TDPA). The obtained imogolite polymer nanocomposite were well dispersed in organic solvent with well aligned NTs in a film obtained with aligned NTs on graphite support. However, using ODPA shows more ordered films, with respect to TDPA, due to longer alkyl chains, which improve the intercrossing with respect to TDPA. The surface modification of imogolite with ODPA was confirmed by force-distance curve measurement between the cantilever tip and imogolite surface before and after adsorption of ODPA. The results revealed that the adhesion force between imogolite and cantilever tip was much larger than between ODPA-chemisorbed on imogolite surface (Scheme 1-10). Adsorption of ODPA change the hydrophilicity due to hydrophobic alkyl groups that substitute hydroxyl groups [14].

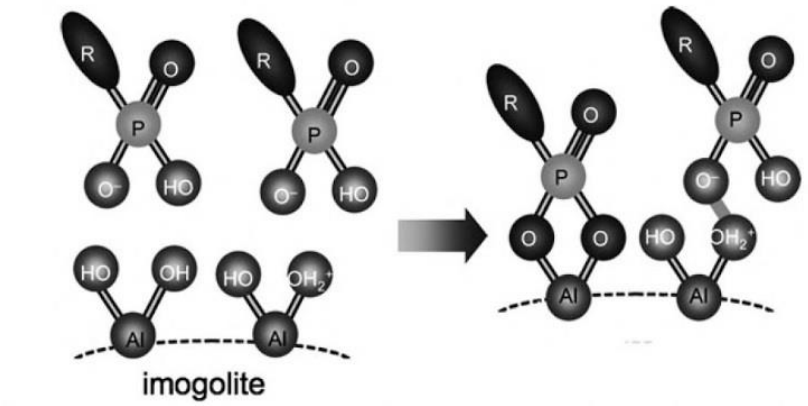

Scheme 1-10: Interaction mode between imogolite surface and alkyl phosphonic acid

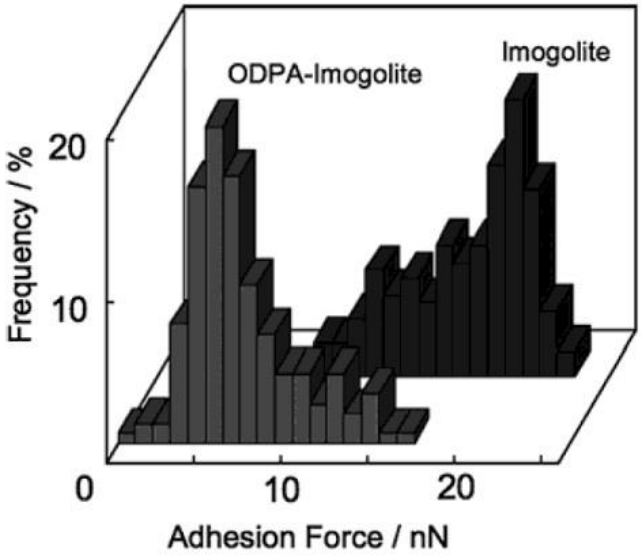

Scheme 1-11: Histogram of adhesion forced between imogolite surface and cantilever tip before and after adsorption of OTDA

A further step is needed in order to obtain imogolite polymer nanocomposite and enhance the affinity toward organic moieties. The outer surface of imogolite is functionalized with organic groups bearing a negatively charged head, which can react with outer surface of other imogolite NTs and reactive end can undergo further polymerization [119]. This method introduces a new imogolite poly (methyl methacrylate) hybrid material [123]. For instance, immobilization of ATRP (atom transfer radical polymerization) on imogolite surface develops an amphiphilic surface-attachable ATRP initiator, which is soluble in water and plays an important role for the homogenous modification of imogolite NTs. PVC/PMMA-g-imogolite nanohybrid was prepared by using this PMMA grafted imogolite as shown in Scheme 1-11. The new modified imogolite-based materials are expected to be important in the synthesis of organic/inorganic hybrid materials [6, 119].

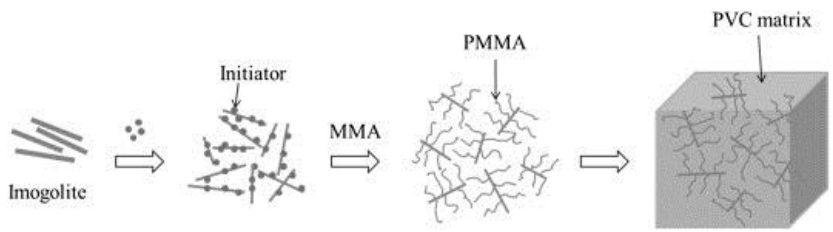

Scheme 1-12: Fabrication procedure for PVC/PMMA-g-imogolite nanohybrid

Another new modification of the outer surface refers to isomorphic substitution of Al^{3+} with Fe^{3+} ions, which is a common process in all natural aluminosilicates and brings interesting physico-chemical properties to the new material. However, only few papers have been published in this area. By substitution of iron in place of aluminum three Fe(OH)Al and three Fe-O-Al groups should form and the new material demonstrates new chemical and solid state properties (Scheme 1-12) [21, 22, 24, 85]. All this notwithstanding, the nature and electronic effects generated by Al^{3+}/Fe^{3+} IS are not fully understood yet.

Several authors agree that up to 1 wt. % Fe may isomorphically substitute for Al, whereas at higher Fe loadings (> 1.4 wt% Fe), iron oxo-hydroxide clusters formation occurs along with IS, and NTs formation is hampered at high Fe contents [21, 23, 24]. Nonetheless, Shafia *et al.* obtained Fe-doped imogolite NTs by both direct synthesis and post-synthesis ionic exchange [23, 24, 85], the latter result opening the possibility to dope imogolite without perturbing the (delicate) hydrolysis equilibria leading to NTs formation. Furthermore, the band gap (E_g) of imogolite, as an insulator with E_g = 4.9 eV, decreased to 2.4-2.8 eV in Fe-doped NTs that ultimately show semiconducting properties [23, 24]. Shafia *et al.* also investigated the synthesis and application of Fe-doped imogolite NTs in the degradation of Acid Orange 7: remarkable catalytic properties where observed under dark conditions, due to the formation of very reactive Al-OOH groups in the presence of H_2O_2 [85].

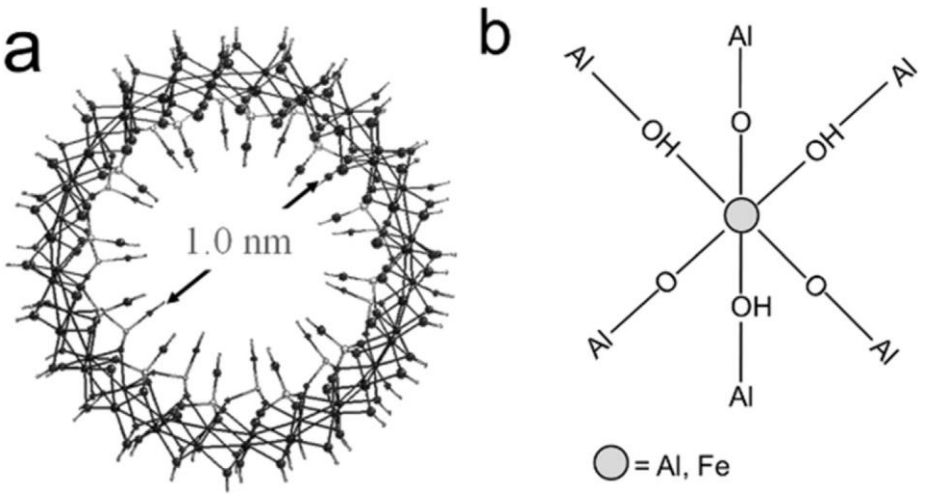

Scheme 1-13: Section a: front view of an imogolite NT, with an inner diameter of 1.0 nm with the SiOH and Al(OH)Al groups at the inner and outer surface, respectively. Section b: isomorphic substitution of one Al(VI) at the outer surface of imogolite by one Fe^{3+} ion and formation of three Fe-OH-Al groups and three Fe-O-Al groups [23, 24]

1.7 Topics covered in my thesis

During my PhD thesis, I mainly focused on synthesis, application and thermal stability of methyl-imogolite (MeMO), with higher microporosities and larger specific surface area, with respect to imogolite ones. One of the main critical obstacles facing the synthesis of this material is reproducibility of NTs with high percentage of purity. The optimum synthesis process in order to get the highly pure MeIMO NTs and complete physico-chemical analysis performed on this material was done during this PhD research (Chapter 2).

Since Fe doped imogolite type NT showed an interesting catalytic performance, loading of iron in MeIMO structure has been also studied for the first time in this PhD thesis. Iron doping was obtained by means of ionic exchange (IE) and direct synthesis method (DS) with two Fe contents, namely 0.7 and 1.4 wt. % and thorough physico-chemical analysis was performed in order to investigate the structure of these new materials. (Chapter 3).

Since thermal stability is an issue for many catalytic applications, the thermal stability of MeIMO and iron doped MeIMO with two methods (DS and IE), and in different atmosphere (air and vacuum) was fully investigated by a means of thermal analysis (TG/DTG) and the calcined samples treated in high temperature analyzed (by means of TEM, Solid state NMR, UV-vis spectroscopy, BET and XRD) (Chapter 4).

The investigation of different acidic sites on the surface of NT has been performed by FT-IR spectroscopy. Furthermore the catalytic activity toward the interaction with NaAO7 dye in water has been studied (Chapter 5).

Finally the catalytic application of MeIMO and iron doped MeIMO have been investigated in adsorption and discoloration of azo dye (A07) and photocatalytic performance for discoloration and mineralization of Tartarazine dye in photo-Fenton process (Chapter 6).

Chapter 2

Synthesis and Characterization of Methyl-Imogolite

2.1 Introduction

Bonelli and co-workers (2009) patented a new modified imogolite NTs by synthesis method and replacing TEOS (Tetraethyl orthosilicate) precursor with TEMS (Triethoxymethylsilane) [9, 107] (Scheme 2-1). The new type of imogolite-like NT is named methyl-imogolite (MeIMO: $(OH)_3Al_2O_3SiCH_3$), and is chemically modified at the inner surface with methyl groups replacing hydroxyl groups; therefore, it presents an inner hydrophobic surface and outer hydrophilic surface, due to $SiCH_3$ and Al(OH)Al groups respectively (Scheme 2-2) [9, 80, 124].

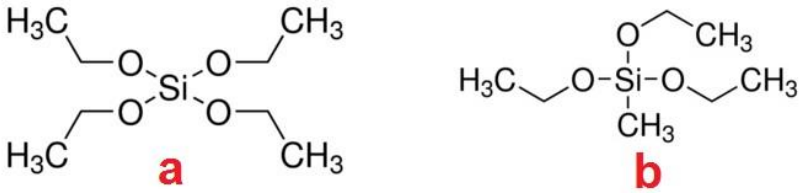

Scheme 2-1: Structural representation of TEOS (a) and TEMS (b) precursors

MeIMO NTs have larger diameter with respect to imogolite, due to the substitution of methyl groups in the structure ($Ø_{MeIMO} \cong$ 2.0-2.5 nm, $Ø_{IMO} \cong$ 1.0 nm) [125]. There are two main factors for tubular imogolites formation: (i) the hydrogen bond (HB) networks is constructed by the arrangement of inner hydroxyl

(OH) groups. This favors the strain energy-minimum, which is the preference for zigzag chirality; (ii) the variations of the atomic bond distance between the inner and outer Al-O and Si-O bonds [100, 125]. Since in MeIMO with inner methyl groups there should be no HB contribution, the most significant factor is likely the second one. Consequently, in MeIMO, energy-minimum decreases with increasing the tubular curvature followed by an increase of the NT diameter [100, 125].

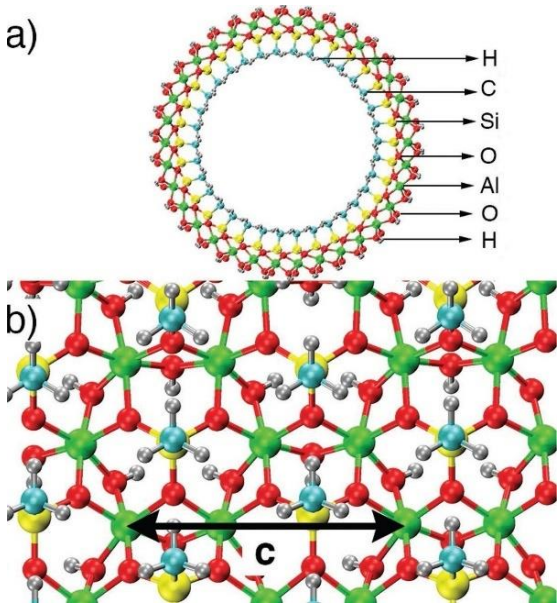

Scheme 2-2: Frontal view of a MeIMO single-walled NT, exposing Si-CH_3 at the inner surface and Al-OH-Al, Al-O-Al groups at the outer surface [126]

MeIMO is as an example of organic/inorganic hybrid material with a nanometric diameter combined with a length of several microns, with specific surface properties and both larger pores and higher specific surface area with respect to imogolite NTs [9].

The structure of MeIMO NTs increases the potential of this material in different applications, such as gas chromatography and gas separation [9]. The special arrangement of NTs in dehydrated samples gives rise to three kinds of pores (Scheme 2-3): (i) intra-tube pores (pore A, *ca.* 2.0 nm) that are not accessible to probe molecules like CO, CO_2, NH_3 and H_2O, due to poor affinity within these molecules and inner surface of NTs, because of non-polarity and hydrophobicity of Si-CH_3 groups [9]. On the contrary, in imogolite (as mentioned in chapter 1) A pores are accessible to gas molecules only after dehydration and evacuation at 300 °C [8]. (ii) B pores, which in imogolite structure are not accessible to even small molecules, such as water [78, 79]; however, in MeIMO these pores are slightly

larger (*ca.* 0.3-0.45 nm) (Scheme 2-4) and accessible to molecules like carbon monoxide (CO), carbon dioxide (CO_2) and ammonia (NH_3) [107, 115]. (iii) C surface, with similar amphoteric properties in both materials (MeIMO and imogolite), due to the presence of Al-O-Al and Al-OH-Al groups. Therefore, the outer surface can react with both acidic molecules [i.e. with carbon dioxide (CO_2), by forming carbonate like species] and with basic molecules [like ammonia (NH_3), by forming ammonium species].

Bonelli *et al.* [9] studied MeIMO capacity for the adsorption of methane at 30 °C with increasing pressure range (5-35 bars). According to their studies, MeIMO has a higher adsorption capacity (~about 2.5 times higher) with respect to imogolite, due to three times larger inter-tube cavities in this material comparing to imogolite (Scheme 2-4) [107]. Furthermore, these pores can provide a confined environment to the carbon dioxide molecule, and relatively large van der Waals interactions between the molecule and the walls [107].The comprehensive representation of different types of porosities and their potential accessibility to acidic and basic molecules are shown in Scheme 2-5.

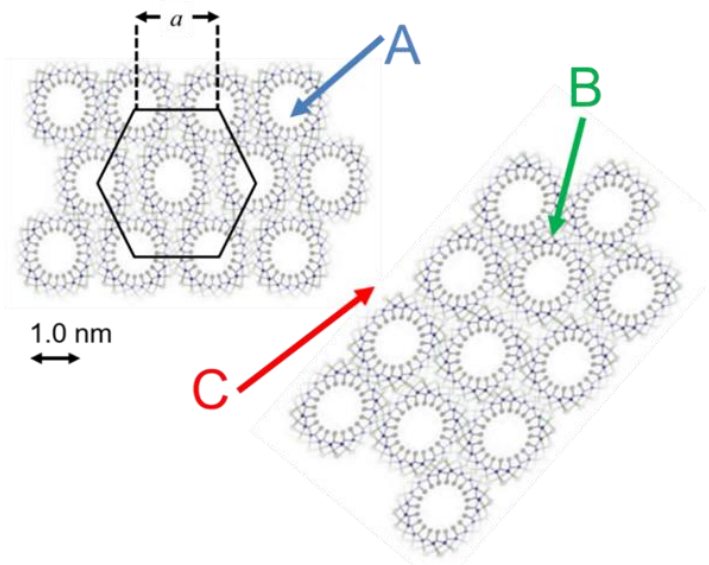

Scheme 2-3: MeIMO NTs hexagonally packed in bundles. The cell parameter *a* corresponds to the distance between the center of two adjacent NTs. Pores A, B and C correspond to proper NTs micropores (ϕ = 2.0 nm), pores among three aligned NTs within a bundle ($\phi \cong$ 0.30-0.45 nm) and slit mesopores between bundles, respectively

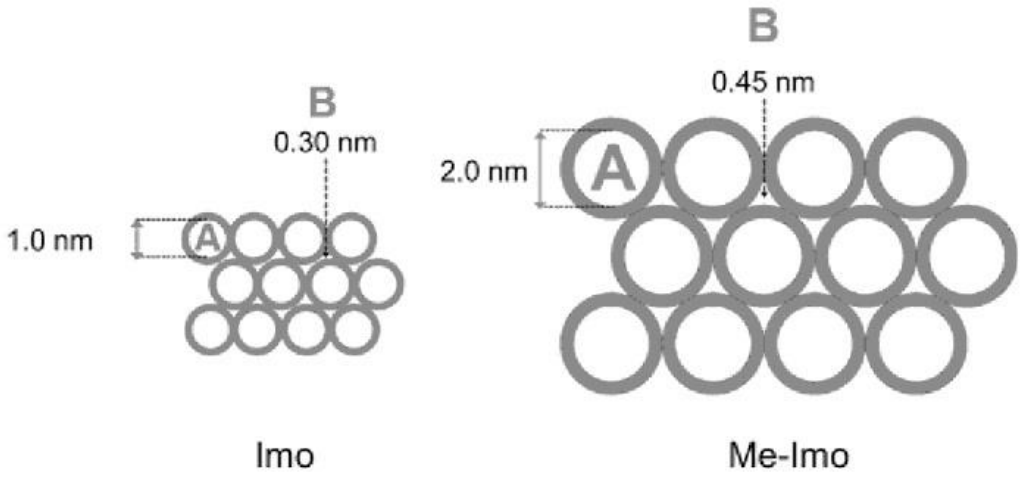

Scheme 2-4: Representation of imogolite and MeIMO bundles, show that the hexagonal packing of nanotubes in dehydrated samples, give rise to larger intertube cavities (pore B) in MeIMO with respect to imogolite [107]

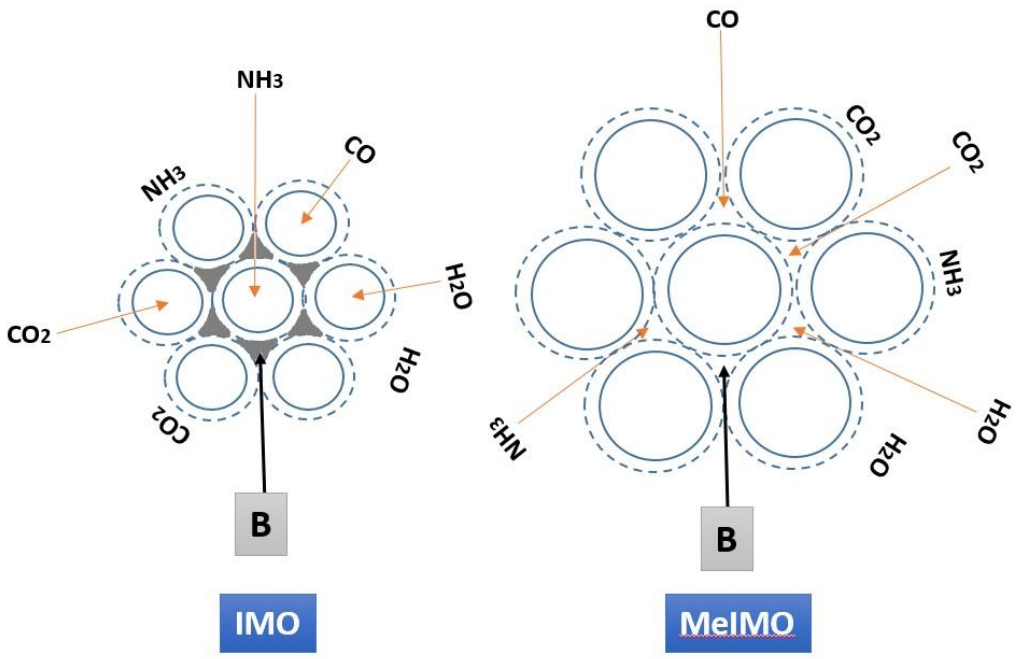

Scheme 2-5: The accessibility of A, B and C surface in imogolite and MeIMO to different probe molecules, like CO, NH_3, CO_2 and H_2O [80]

Previous studies on imogolite NTs, show that AlSi and AlGe Imogolite-NTs present an intriguing real space separation of the valance band energy (VBE) and conduction band energy (CBE), which enhanced electron-hole (e–h) separation via optical charge-transfer excitations across the NT-walls [127-129]. Based on linear-scaling density functional theory (DFT) study on imogolite, the NT wall are permanently polarised due to the different nature of inner and outer wall surface [126]. Furthermore, increasing the NT polarization improves the selective oxidation and reduction of different reactants within different cavities of the NT [130, 131]. However, any specific information are to date unknown for methyl-imogolite wall-polarization, VBE–CBE separation, and optical properties.

Recently, Elliot *et al.* [126], established the DFT modeling on VBE–CBE separation and optical properties of MeIMO and compared the results with those of rutile and anatase TiO_2, whose mixture is well-known to lead an effective water photolysis [132-134]. Their results demonstrate that methylation of inner surface, NT curvature and local permanent polarizations may not affect the band-separation, band-alignment, and the occurrence of charge-transfer excitations [126]. Indeed, MeIMO NTs induce a lower H_2O direct photo-oxidation and respectively higher H_2O photo-reduction ability with respect to TiO_2. Moreover, increasing the NT polarization to values comparable with state of the art ferroelectric photocatalyst and tuning NT-reactant electronic alignments, by altering the NT radius and wall-thickness, enhance the e-h separation. Therefore, MeIMO may introduce a novel hybrid organic–inorganic NT for polarization-enhanced photocatalytic application, which will stimulate further experimental interest and investigations [126].

In this chapter, the physico-chemical properties of the synthesized methyl-imogolite NTs were characterized by means of several techniques, including XRD, TEM, adsorption/desorption of N_2 at -196 °C, FTIR and solid state NMR spectroscopies, and compared to imogolite NTs.

2.2 Synthesis of MeIMO

Synthesis of MeIMO was made according to a procedure proposed by Bonelli *et al.* [9, 124].

In order to synthesize *ca.* 3 gr of MeIMO NTs, in a dry-box at room temperature (r.t.), a 80 mM aqueous solution of $HClO_4$ in double distilled water is prepared (pH = 1.0) by slowly adding 1.3 mL of perchloric acid (70 wt. %) to 187.7 mL of double distilled water.

In a smaller beaker within the dry-box, 8 mL of aluminum-tri-*sec*-butoxide (97%, ATSB, as source of aluminum) [135, 136] and 3.2 mL triethoxymethylsilane (99%, TEMS, as source of Si) are mixed in the molar ratio Al:Si = 2 : 1.1. A slight excess of TEMS (10 wt%) is used in order to prevent the preferential formation of gibbsite during hydrolysis [135, 137]. Immediately after out of dry-box, with a Pasteur pipette the whole mixture is dropwise added to the aqueous solution of $HClO_4$ under stirring (the final molar ratios are Si : Al : $HClO_4$ = 1.1 : 2 : 1). By adding the mixture to the $HClO_4$ aqueous solution, white clusters form and pH increases to 5.0. The final mixture is stirred at r.t. for about 18 h, until a transparent solution is obtained. Under stirring, 1.3 L of double distilled water are added to dilute the solution to 20 mM with respect to Al. The obtained 20 mM Al solution is stirred for about 20 min. The mixture is poured into a polytetrafluoroethylene autoclave (with thick walls) and placed in a stove for 4 days at 95-100 °C without stirring. Decreasing the temperature decrease the formation rate of NTs, whereas increasing the temperature results in impurities (aluminum oxide polymorphs) formation. After 4 days, NTs are collected by filtration (0.02 micron filter) and washing with double distilled water. The solid product is dried in oven at 50-60 ° C for 1 day. The final MeIMO powder has a white color.

2.3 Textural properties of MeIMO NTs

2.3.1 FE-SEM and HR-TEM characterization

The FE-SEM and HR-TEM (High resolution-transition electron microscopy) image combined with SAED (Selected Area Electron Diffraction) pattern of MeIMO are shown in Figure 2-1 and Figure 2-2, respectively. As shown in Figure 2-1, once NTs formed, they organize into a porous network of interwoven bundles of closely packed NTs, similar to those of imogolite.

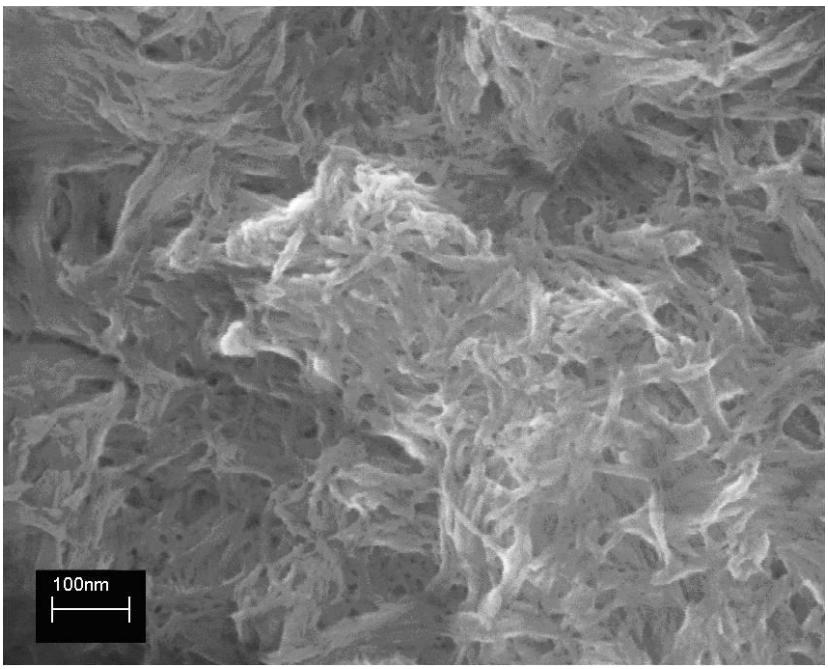

Figure 2-1: FE-SEM image of MeIMO bundles of NTs

HR-TEM images show wide domains of aligned NTs with considerable length (Figure 2-2). NTs have *ca.* 2-2.5 nm diameter and sub micrometric length (*ca.* 200 nm) [11, 138]. NTs tend to aggregate with different degrees of order. Sidorkin *et al.*[139] reported that the Si–O bond length in $(HO)_3Si–X$ and $(CH_3O)_3Si–X$ series of compounds is directly affected by the electronegativity of the X substituent. Therefore, the presence of methyl groups instead of hydroxyls–induces the same effect and results in the structural relaxation, and shifts the energy-minimum towards NTs with a higher number of units in circumferences. Indeed in MeIMO, bonds are freer to arrange in close packed configuration with respect to those of imogolite [13]. It has been demonstrated that the number and dispersion of bundles in solution appears to be pH dependent [76, 77, 140, 141]. According to studies done by Karube *et al.* [142] imogolite NTs flocculate under alkaline conditions and disperse under acidic conditions, having a point of zero net charge (PZNC) around pH 6.

The *inset* of Figure 2-2, shows selected area diffraction pattern (SAED) of bundles formed by few NTs, which demonstrate crystallinity within them. The first broad reflection corresponds to the scattering of individual tubes. The second ring corresponds to the tubes associated in parallel bundles given a comparably sharp reflection. The third reflection corresponds to center-to-center tube separation, and

could be taken as characteristic signatures that differentiate the NTs from any amorphous materials [68, 103].

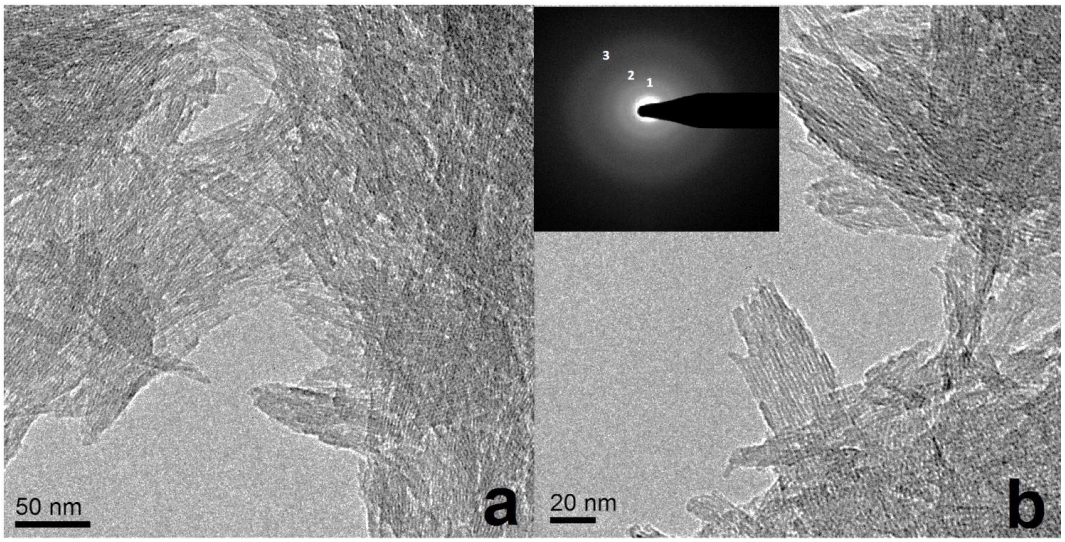

Figure 2-2: (a,b) HR-TEM micrographs of MeIMO taken with two different magnifications. *Inset* (c) SAED taken from a bundle of few NTs

2.3.2 Powder X-ray diffraction (XRD)

Figure 2-3 reports powder XRD patterns of the powder MeIMO sample in comparison with imogolite NTs in a range of 2.5 – 20° 2θ. The XRD pattern corresponds to a hexagonal packing of NTs. The most intense peak is attributed to the d_{100} reflection, from which the cell parameter *a*, corresponding to the center-to-center distance between two aligned NTs, is calculated as $a = 2d_{100}/\sqrt{3}$ (Table 2-1). The (100) reflection is at slightly smaller 2θ angles in MeIMO NTs with respect to imogolite NTs, due to substitution of larger methyl groups instead of hydroxyls. The same behavior has been observed in Ge-imogolite NTs, where silicate groups (Si–O bonds) are partially substituted by germanate groups (Ge-O bonds) [112]. Two broader signals at higher 2θ values are assigned to the d_{001} and d_{211} reflections, stemming from repetition of MeIMO structural units along NTs [2, 25, 48, 119, 141]. The intensity of all peaks and specially the main peak are higher for MeIMO NTs as compared to imogolite NTs. This phenomenon is attributed to the higher degree of long-range order with more ordered packing of the NTs and higher number of units in circumferences for MeIMO NTs with respect to imogolite NTs [13].

According to Table 2-1, the cell parameter *a* values in MeIMO and imogolite are 2.97 nm and 2.62 nm, respectively and the calculated diameters for MeIMO and imogolite are *ca.* 2.0-2.5 nm and *ca.* 1.0 nm, respectively [125]. It means that in MeIMO, NTs are closer to each other. A possible reason could be the fact that within imogolite NTs more ClO_4^- ions are present between NTs to balance the positive charge of external surface (higher than in MeIMO). This fact can lead to a larger inter-tube distance in imogolite with respect to MeIMO NTs.

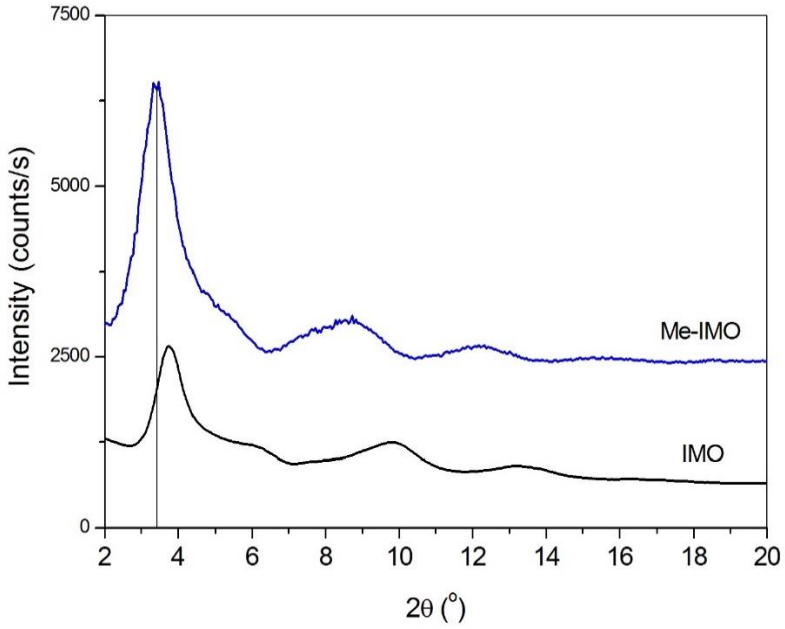

Figure 2-3: Low-angles XRD patterns of imogolite and MeIMO. Vertical lines correspond to d_{100} main reflection of NTs structure

2.3.3 Porosity characterization by N_2 adsorption/desorption isotherms

To determine BET SSA (Brunauer-Emmett-Teller Specific Surface Area) and porous volume, N_2 isotherms were measured at -196 °C on both samples (MeIMO and imogolite), previously outgassed at 250 °C, a temperature allowing the removal of water and other atmospheric contaminants still preserving NTs structure [8, 25, 143]. Microporous volume was calculated according to the *t*-plot method. NL-DFT (Non Local Density Functional Theory) method was used to determine Pores Size Distributions (PSDs), by applying a N_2-silica kernel for cylindrical pores on isotherms adsorption branch. The same method was also used to measure the ratio between microporous surface area and total SSA.

N_2 sorption isotherms at -196 °C and corresponding pore size distribution are reported in Figure 2-4a and 2-4b respectively. The related values of BET SSA and pores volume being reported in Table 2-1.

As-synthesized MeIMO sample (Figure 2-4a) shows type IV isotherms with type H4 hysteresis loop, typical of microporous systems with some mesoporosity [144]. Imogolite has instead a type I isotherm, typical of a (mostly) microporous materials. According to the isotherms, the SSA and microporous volume of MeIMO is twice of those reported imogolite treated at the same outgassing temperature, due to larger inner pore cavities. PSD curves of MeIMO show a family of nanopores with diameter of *ca.* 2.0-4.0 nm range. A wide range of mesoporosity (*ca.* 2.5-5.0 nm) is also detectable, due to heterogeneous C pores and indicating that MeIMO is mostly a mesoporous material. According to previous studies, the microporous volume increases with increasing the outgassing temperature, whereas larger mesopores are less affected by thermal treatment [9].

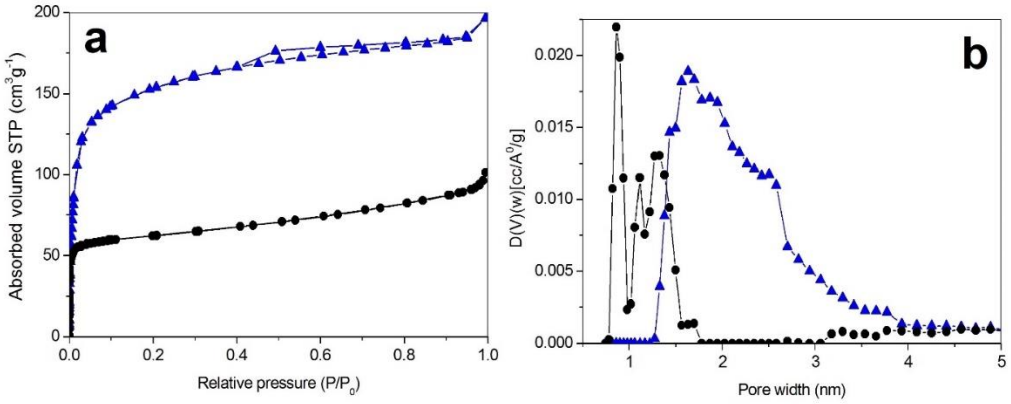

Figure 2-4: N_2 isotherms at -196 °C (a) and corresponding PSDs (b) as obtained by applying the NL-DFT method on samples MeIMO (blue triangles), imogolite (black circles)

Table 2-1: Samples textural properties as derived by XRD patterns and N_2 sorption isotherms at -196 °C

Sample	d_{100}, nm (±0.01)	a (nm)	(100) reflection (°)	BET SSA ($m^2 g^{-1}$)	Microporous volume ($cm^3 g^{-1}$)[b]	Total Pore Volume ($cm^3 g^{-1}$)
imogolite	2.27	2.62	3.8	237	0.08	0.14
MeIMO	2.58	2.97	3.4	580	0.11	0.28

2.3.3.1 Formation of aluminum oxide polymorphs

Based on several studies on imogolite structure, numerous factors are recognized to influence the polymorphic nature of an initial aluminum hydroxide precipitate including pH, temperature, kinetics, the presence and absence of ligands and foreign ions, particularly anions [103]. Moreover, formation of imogolite NTs is affected by different variables like temperature, Si concentration in the bulk solution and polymerization time [103].

According to studies done by Farmer *et al.* [106] enthalpy and free energy of the reaction have been measured for imogolite ($(HO)_3Al_20_3SiOH$) and boehmite (AlO(OH)) from equilibrium silicon concentration and at different temperatures in solution (reaction 2-1), and consequently calculated for gibbsite ($Al(OH)_3$), halloysite ($Al_2Si_2O_5(OH)_4$) and kaolinite ($Al_2Si_2O_5(OH)_4$) (Table 2-2).

$$(OH)_3Al_2O_3 + H_2O \leftrightarrow 2AlOOH + Si(OH)_4 \quad (2-1)$$

Accordingly, at 25 °C and in a solution containing 20 μg cm^{-3} SiO_2, halloysite, imogolite and gibbsite are equilibrium with each other. At T< 25 °C and in sufficient silica concentration (for preventing decomposition to gibbsite), halloysite is more stable than imogolite. At T> 25 °C and specific range of silica concentration imogolite is more stable than halloysite, while with respect to kaolinite both are metastable [106]. Their results were in agreement with previous observation that imogolite, halloysite and gibbsite can co-exist in soil [145].

Table 2-2:.Enthalpy and free energy of formation of soil components (kJ mol^{-1}) [103]

Minerals	**$\Delta H°_f$ (25 °C)**	**$\Delta G°_f$ (25 °C)**
H_2O	-285.8	-237.2
$Si(OH)_4$	-1459.0	-1308.7
Boehmite	-988.9	-914.2
Imogolite	-3189.6	-2926.7
Gibbsite	-1293.1	-1154.9
Kaolinite	-4120.1	-3799.4
Halloysite	-4101.5	-3780.8

In Wada's experiment [104], it was shown that a 7 year long synthesis at 25 °C leads to synthetic imogolite having a diameter close to the natural ones. More recently, both Nair *et al.*[99] and Rose *et al.* [102] reported that the growth of imogolite NTs may be a thermodynamically driven self-assembly process, in which controlling the temperature controls the nanoparticle condensation and allows for the self-assembly process. According to their studies [99, 102], proto-imogolite clusters formed at the initial stage of the synthesis are able to assemble into a NT structure.

Synthesis of MeIMO as well as imogolite [101] depends on kinetics and thermodynamics of formation, however, up to now no studies have been done for better understanding of formation mechanism of MeIMO NTs. Temperature, as one of the principal thermodynamic parameters, plays an important role in formation and diameter modulation of proto-MeIMO cluster, which in turn is a function of the degree of $SiCH_3$ substitution in the structure.

The $SiCH_3$ substitution in the proto-methyl-imogolite structure highly depends on the synthesis temperature. At low temperature the $SiCH_3$ substitution is low, whereas by increasing the temperature (up to 95 °C) the $SiCH_3$ substitution increases and sets the stage for formation of stable NT structure. However, any distribution in equilibrium thermodynamic and kinetic conditions, results in formation of other phases. Therefore, in order to achieve an effective synthesis of MeIMO, several criteria must be met by both the aluminum and silicon sources. One of the most common phases formed from unsuccessful synthesis process is one specific type of aluminum oxide polymorph called Nordstrandite with triclinic crystalline unit cell, observed as a star shape phase in FE-SEM microscopy (Figure 2-5), and typical reflection centered at ca 18.5 2θ, in XRD pattern (Figure 2-6) [146, 147].

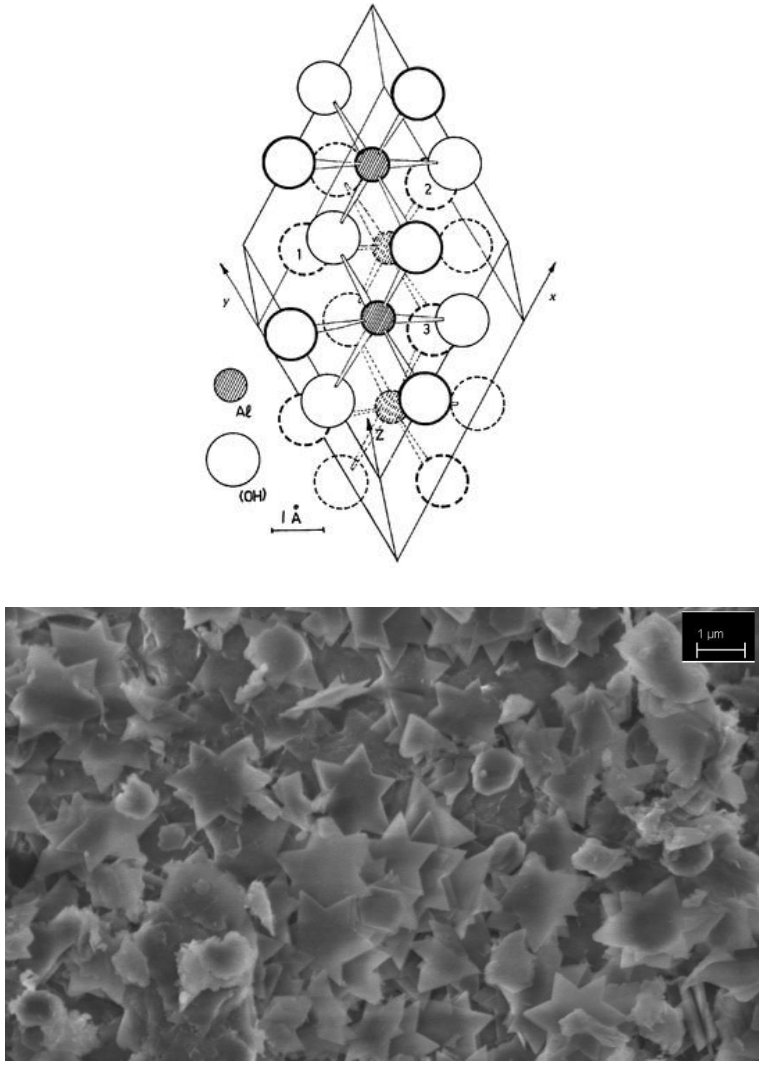

Figure 2-5: Structure of nordstrandite ($Al(OH)_3$), projected on xy plane, b: FE-SEM image of nordstrandite phase

In this PhD thesis, the effect of temperature and polymerization time on formation of MeIMO was investigated. The optimum temperature and time achieved in the presence of Al:Si= 1.1:2 molar ratio, was between 95-100 °C and 4 days. NTs formation rate decreases to much below 95 °C, whereas above 100 °C, the formation of aluminum oxide polymorph is highly probable.

According to XRD patterns, increasing the temperature above 105 °C (Sample 1: 105 °C <T<110 °C) results in the formation of high amount of aluminum oxide polymorphs (nordstrandite) as derived by a lower intensity of the main peak of the XRD pattern. Conversely, in sample 2 (98 °C <T<105 °C, 4 days) a negligible

amount of nordstrandite is detectable and Sample 3 (95 °C <T<100 °C, 4 days) has no trace of formation of nordstrandite.

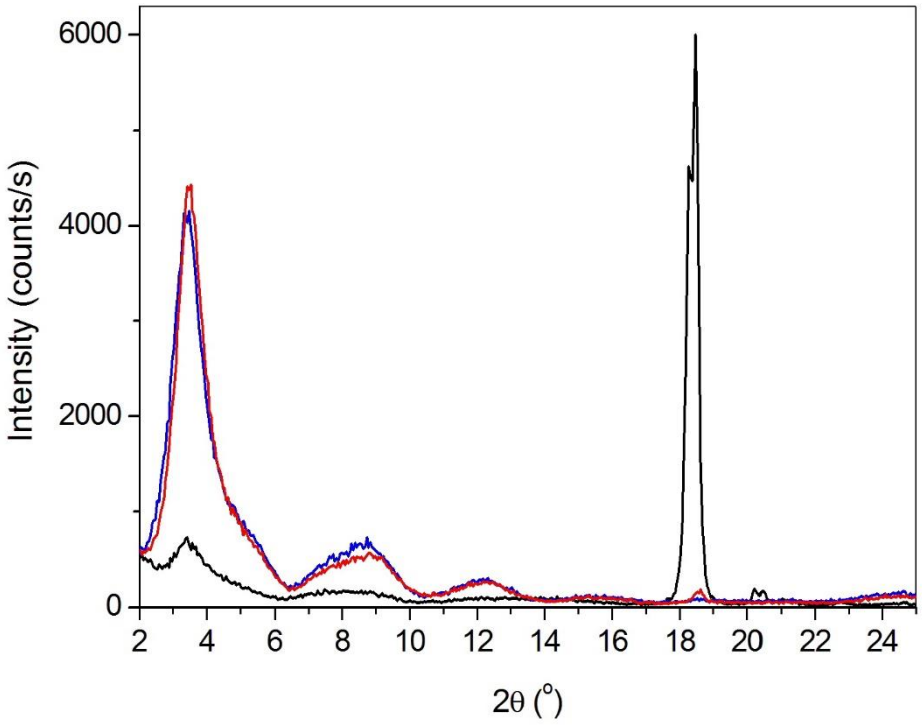

Figure 2-6: Low-angles XRD patterns of MeIMO synthesis in different temperatures with different times: sample 1-black line (105 °C <T<110 °C and 4 days), Sample 2-red line (98 °C <T<105 °C and 4 days), Sample 3-blue line (95 °C <T<100 °C and 4 days)

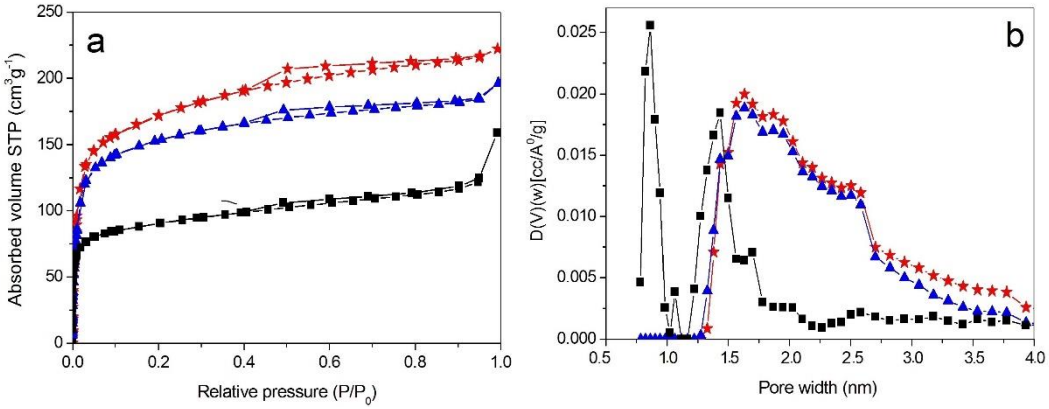

Figure 2-7: N_2 isotherms at -196 °C (a) and corresponding PSDs (b) as obtained by applying the NL-DFT method on sample 1-black squares (105 °C <T<110 °C and 4 days), Sample 2-red stars (98 °C <T<105 °C and 4 days), Sample 3-blue triangles (95 °C <T<100 °C and 4 days)

Figure 2-7a and 2-7b report the N_2 isotherms at -196 °C and corresponding pore size distributions, respectively. Sample 1, with the highest amount of aluminum oxide polymorph, has the lowest amount of micropores (in a range of 2.0-2.5 nm) and also the lowest total pore volume. On the contrary, samples 2 and 3 have higher amount of micropores in a range of 1.8-2.7 nm. The related BET SSA and pores volume are reported in Table 2-3.

Table 2-3: Samples textural properties as derived by XRD patterns and N_2 sorption isotherms at -196 °C

Sample	Time of autoclave (day)	Temp of autoclave (°C)	d_{100} (nm) (±0.01)	a (nm)	BET SSA ($m^2 g^{-1}$)	Microporous volume (cm^3g^{-1})[b]	Total Pore Volume ($cm^3 g^{-1}$)
MeMO-1	4 days	T=105-110°C	2.6	2.97	334	0.09	0.23
MeMO-2	4 days	T=98-105°C	2.5	2.95	617	0.11	0.32
MeMO-3	4 days	T=95-100°C	2.6	2.67	580	0.11	0.28

2.3.4 MAS NMR characterization

NMR spectroscopy is an important analysis method, which provides considerable information about the structure of aluminosilicates [148-150] including clay minerals [76, 151]. The position of the silicon resonance is mainly influenced by its degree of polymerization, and by the nature of cations in the nearest neighboring. The aluminum resonance is mainly affected primarily by the number of atoms in its immediate coordination environment, *i.e.* to whether the aluminum is four- or six fold coordinated by oxygen. Therefore, MeIMO was characterized by ^{13}C, ^{27}Al and ^{29}Si MAS NMR measurements, for studying the structure and investigating the structural units of this material.

The ^{13}C NMR shows a chemical shift at *ca.* -1.35 ppm, a value reasonably close to that of ^{13}C in the reference TEMS (Triethoxymethylsilane), around 0 ppm (Figure 2-8).

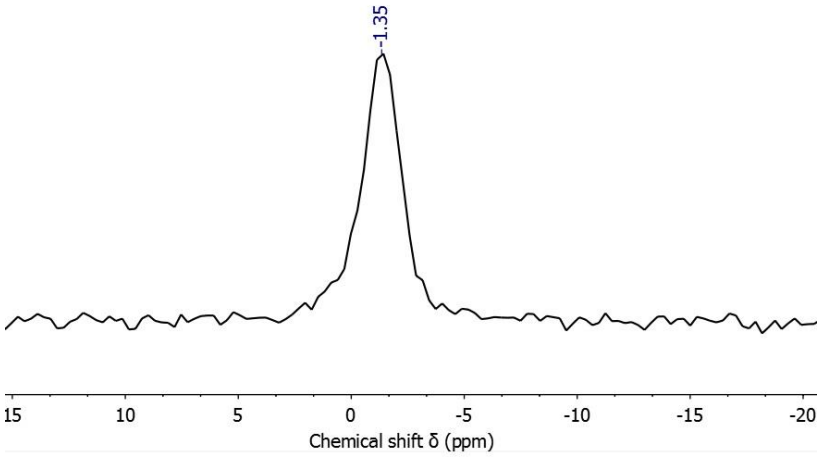

Figure 2-8: Solid-state ^{13}C-MAS NMR of MeIMO

^{29}Si MAS NMR spectrum (Figure 2-9) presents a sharp peak with a chemical shift value δ = -42.5 ppm, which is typical for tetrahedral Si atoms bonded to one carbon and three Al atoms through oxygen bridges at the inner surface of NTs [9, 13]

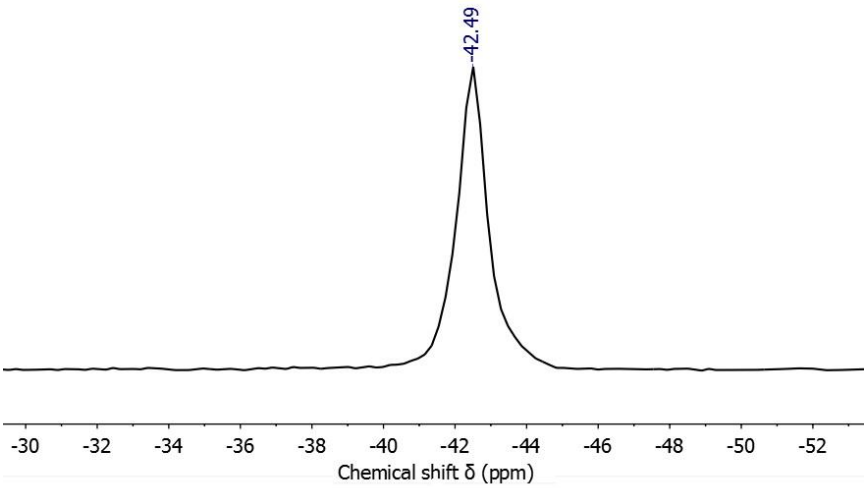

Figure 2-9: Solid-state ^{29}Si-MAS NMR of MeIMO

The ^{27}Al MAS NMR spectrum in Figure 2-10 shows a major single shift, approximately at 7.52 ppm. The shift is the same as gibbsite (δ = 7.52 ppm), indicating the prevalent presence of octahedral Al atoms [152]. The NMR spectrum also exhibits a minor peak at δ = 61.77 ppm (*inset*), along with a small contribution from the second spinning-sideband of the major peak (asterisks). According to previous studies, the 61.77 ppm peak is likely due to a minor amount of four-coordinated Al atoms, probably due to formation of an amorphous phase rather than NTs, in agreement with the literature [143].

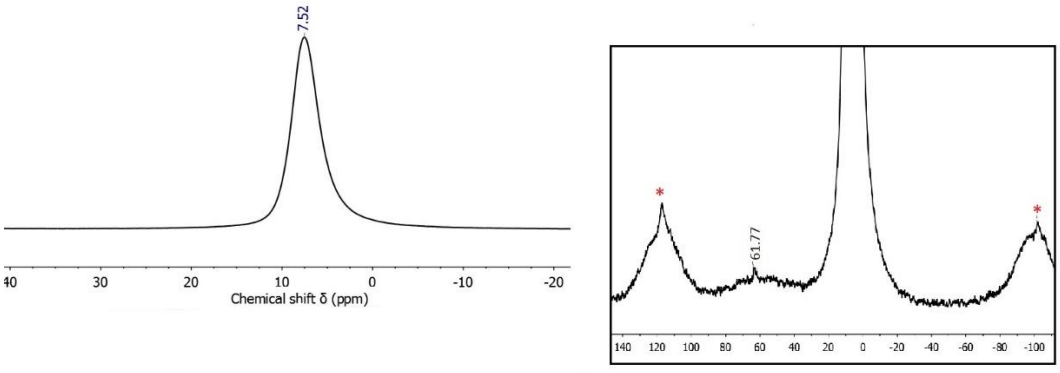

Figure 2-10: ^{27}Al-MAS NMR of MeIMO

2.3.5 Thermogravimetric analysis (TGA)

Figure 2-11 reports both thermogravimetric (TG; black line) and derivative thermogravimetric (DTG; blue line) analysis of MeIMO. The analysis was performed on 10 mg sample powder, heating from room temperature up to 500 °C, under Ar flow (55 ml min^{-1}), with the temperature increasing rate of 10 °C min^{-1}, by SDT 2960 DTA/TGA-MS instrument.

According to the curves, two broad endothermic peaks corresponding to two weight losses were observed. The first peak at 75 °C is assigned to the dehydration of the hydrophilic outer surface of MeIMO NTs. Comparing the results with those obtained by Zanzottera *et al.* [25], MeIMO starts loosing adsorbed molecular water at lower temperature with respect to imogolite. This behavior ascribed to larger B pores in MeIMO structure, which favor mass transfer through the porosities (Scheme 2-4). The second peak at 360 °C is due to an actual structural transition through dehydroxylation and collapsing the NTs structure at temperatures higher than 300 °C [25], which will be explained in chapter 4. According to Zanzottera *et al.* [25] in MeIMO, the reaction between inner CH_3 groups and outer hydroxyl groups at around 300 °C, resulted in Si-O-Al bonding and formation of methane, which was detected in their experiments (reaction 2-2):

$$Si - CH_3 + OH - Al \rightarrow Si - O - Al + CH_4 \quad (2-2)$$

An additional minor endothermic mass loss observed in TG analysis is at 440 °C, assigned to the release of oxygen molecules, caused by thermal decomposition of remaining perchlorate species (ClO_4^-) present in the synthesis bath. The same peak has been observed in previous studies on imogolite [25] and alumino-germanate imogolite NTs at 477 °C and 415 °C [113, 153], respectively.

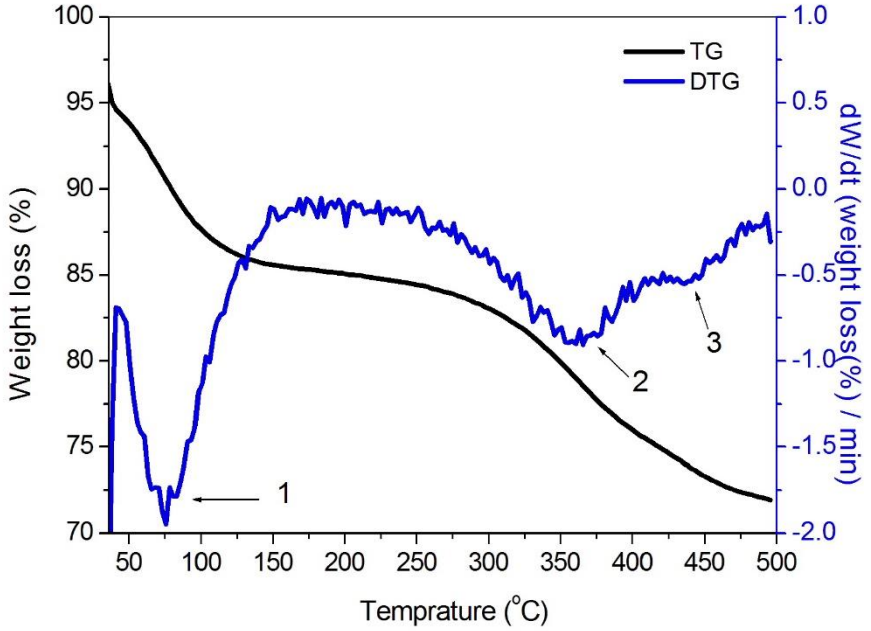

Figure 2-11: Thermogravimetric (TG; black line) and derivative thermogravimetric (DTG; blue line) analysis of MeIMO

2.3.6 FTIR characterization of MeIMO NTs

Figure 2-12 reports the IR spectra of a MeIMO pellet, outgassed at r.t. and 150 °C. With increasing the temperature (T > 75 °C) the band at 1644 cm^{-1}, due to the bending mode of water molecules mainly located at the outer surface of NTs, disappears almost completely, in agreement with the data obtained from TGA analysis. Indeed, in more hydrophilic imogolite NTs, this band is still observed after outgassing up to 150 °C [8, 9]. The sharp band at 1275 cm^{-1} is due to the bending mode of the Si–CH_3 (δ CH_3) groups; as well as the bands at 2978 and 2919 cm^{-1}, which are respectively assigned to the asymmetric (ν_a CH_3) and symmetric (ν CH_3) stretching modes of the Si–CH_3 groups. The broad and intense absorption in the OH stretch region (3800–3000 cm^{-1}) is assigned to the presence of outer Al(OH)Al groups [8].

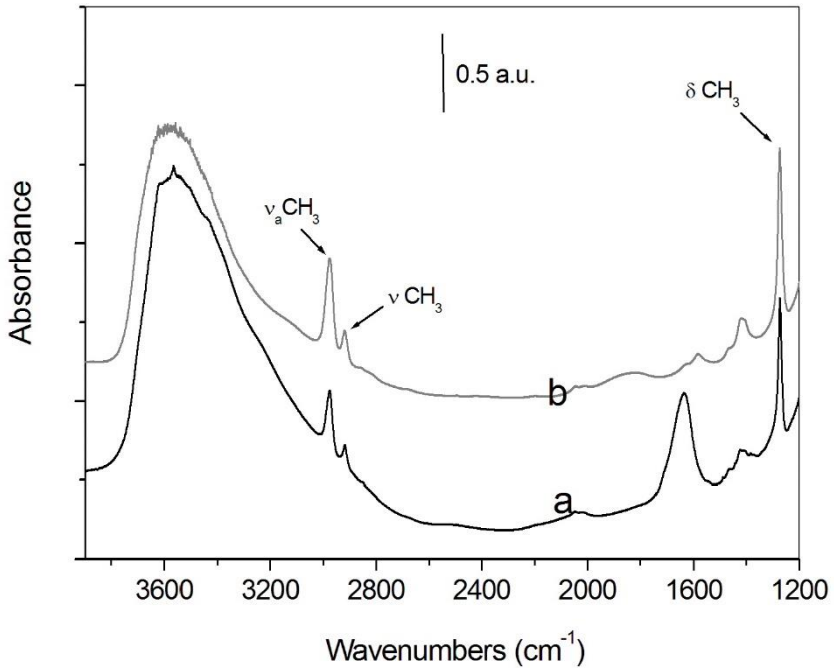

Figure 2-12: IR spectra of MeIMO outgassed at: r.t (a) and 150 °C (b). The methyl groups functionalities pointed out by arrow

2.4 Conclusion

Methyl-imogolite (MeIMO) is a hybrid organic/inorganic NT obtained by non-expensive, environmental friendly and mild-conditions synthesis. This material has high surface area, and its tubular structure is stable up to 300 °C.

The inner pores of NTs are accessible to small molecules like N_2 after outgassing at 150 °C and removing the entire adsorbed water. The presence of an inner hydrophobic surface along with an outer hydrophilic one makes this material suitable for potential applications, *e.g.* in the fields of gas chromatography and gas separation. Nonetheless, obtaining the NTs of controlled dimension with the whole inner surface covered by functionality other than methyl groups, and increasing the NTs polarization with ferroelectric photocatalysts in order to enhance e-h separation within the structure, may introduce a novel hybrid organic–inorganic NT for polarization-enhanced photocatalytic applications and opens the way to other $(OH)_3Al_2O_3Si$–X analogues.

Chapter 3

Synthesis and Characterization of Fe-Doped Methyl-Imogolite Nanotubes

3.1 Introduction

Modification of the outer surface of NTs involves either electrostatic interaction or covalent bonding [11, 14, 154]. Recently, several researchers have studied Fe-doped imogolite NTs [21, 24, 85]. Although Al/Fe isomorphic substitution is a common process in all natural aluminosilicates, little is known about Fe-doped imogolite. The presence of Fe^{3+} in the structure imparts new chemical and solid-state properties [20]. Ookawa and co-workers for the first time synthesized Fe-containing imogolite NTs [21, 22].Their studies demonstrate that there is an upper limit to the amount of iron that can be hosted in the structure, in that NTs are preserved up to an overall 1.4 wt % Fe content.

The recent studies on Fe-doped aluminum-germanate NTs, analogous to imogolite NTs, showed that NTs formation is preserved up to an overall 1.4 wt % iron content, whereas the upper limit to the amount of isomorphically substituted (IS) iron is 1 wt% and the formation of Fe oxo-hydroxides unavoidably occurs at higher Fe content [155]. Theoretical calculations showed that iron could either isomorphically substitute for aluminum or create “defective sites”, and reduces the band gap energy of the original material. According to Shafia *et al.* [24] doping

with iron reduces the band gap of imogolite from 4.9 to 2.4-2.8 eV. Alvarez-Ramírez *et al.* [20] have also studied the incorporation of iron in Ge-Imogolite NT, demonstrating that the optimized NT models have iron content in the interval $0.05 \leq X \leq 0.1$ and the band gap of Ge-imogolite goes from 4.6 to 2.6 - 1 eV.

According to those authors, Fe ions can locate in three different places in the imogolite structure: inner, outer surface of imogolite and by isomorphic substitution in the Al gibbsite layer (Scheme 3-1). In all of the configurations iron affects the electronic states of the bandgap region, generating the reduction of the gap values with respect to original NTs.

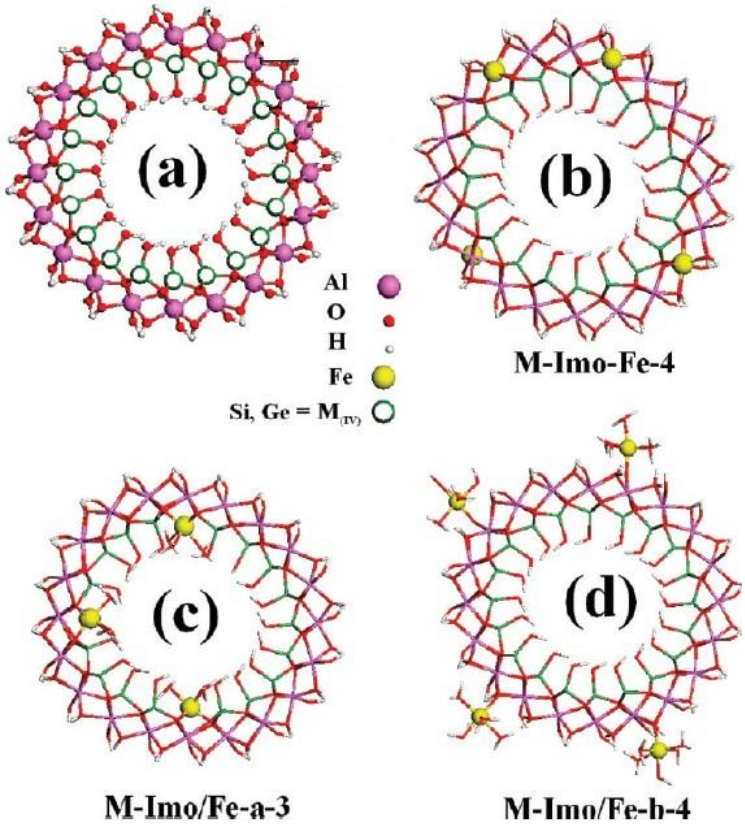

Scheme 3-1: Diagonal cross section of the imogolite structure, which indicates the atomic layers in the structure. (b) Schematic representation of octahedral isomorphic substitution of Al^{+3} for Fe^{+3}. (c-d) Adsorption of octahedral Fe^{+3} ions on the inner and outer defects of imogolite surface. In all the cases, the M symbol denotes both Si and Ge containing structures [20]

So far, no work has addressed the effect of Fe-doping on MeIMO: in this chapter we will report the results of the successful synthesis of novel Fe-MeIMO NTs (Scheme 3-2), in which iron doping is achieved by either direct synthesis (Fe-x-IMO-DS) or post-synthesis ionic exchange (Fe-x-IMO-IE, where x = 0.7 or 1.4 wt % Fe).

The physico-chemical properties of the synthesized samples were characterized by means of several techniques (XRD, TEM, Elemental analysis, UV-Vis spectroscopy, EPR, adsorption/desorption of N_2 at -196 °C, FTIR and solid state NMR and compared to the original MeIMO.

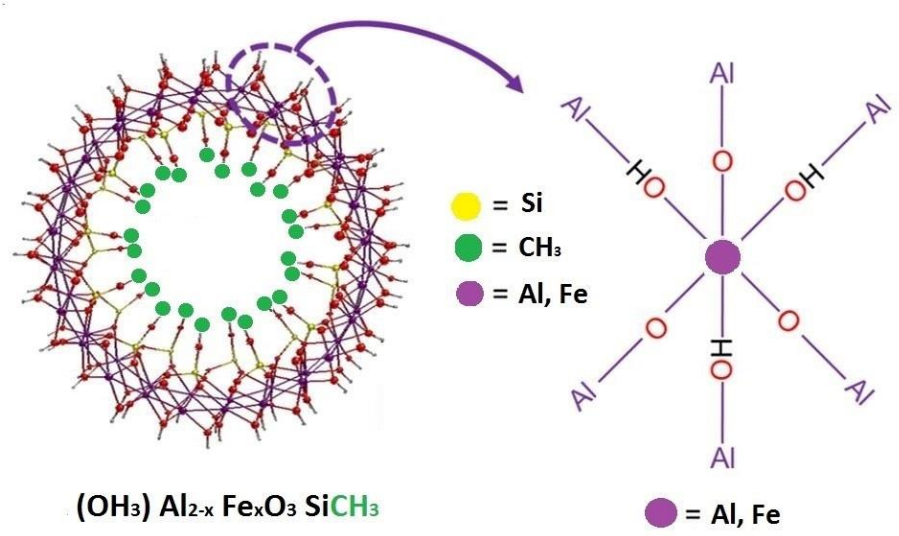

Scheme 3-2: On the left side: frontal view of a MeIMO single-walled NT (left side) exposing Si-CH_3 at the inner surface and Al(OH)Al, Al-O-Al groups at the outer surface. On the right side: environment ideally surrounding each octahedral cation (Al^{3+}, Fe^{3+}) at the external surface of NTs

3.2 Synthesis of iron doped MeIMO

Fe-containing methyl Imogolite (Fe-MeIMO) samples were synthesized by two different methods:

3.2.1 Direct synthesis of iron doped MeIMO (Fe-x-MeIMO-DS, where x = 0.7 or 1.4 wt % Fe)

In a dry box, a proper amount of iron (III) chloride hexahydrate ($FeCl_3$*$6H_2O$ (97%)), as a source of iron, was added to 80 mM solution of perchloric acid in double-distilled water. Aluminum-tri-sec-butoxide (97%) as a source of Al and Triethoxymethylsilane (99%) as sources of Si, were mixed and stirred for some minutes (molar ratio: ATSB:TEOS 2:1.1). The pH of the equilibrium of solution was 4. The mixture was stirred for 18 h at room temperature. After 18 h stirring, a clear reddish brown solution was obtained. Bi-distilled water was added in order to dilute solution to 20 mM Al and the resulting solution was stirred for 20 min. For preparing 2 g of Fe-1.4-MeIMO-DS (1.4 wt.% Fe), use 0.2 g $FeCl_3 \cdot 6H_2O$ in 127 mL of an 80 mM solution of perchloride acid and add the mixture of ATSB (5.4 mL) and TEMS (2.2 mL) dropwise to the solution, dilute the solution after 18 h of stirring with 885 mL double-distilled water. After dilution, the mixture was poured into a thick wall Teflon bottle, and autoclaved for 4 days at 96° C. After 4 days, jelly liked clusters were observable in the solution. The solution was filtered (0.02 micron filter) and washed with bi-distilled water. The final product was dried in the oven at 120 ° C for 1 day.

3.2.2 Post-Synthesis Loading of MeIMO NTs with Fe (Fe-x-MeIMO-IE, where x = 0.7 or 1.4 wt % Fe)

The proper amount of fine powder of MeIMO was added to double-distilled water in a small beaker. Depending on the iron content (0.7-1.4 wt% of final sample), the proper amount of $FeCl_3$*$6H_2O$ (97%) was added to mixture and stirred for 18 h at room temperature. (For 0.25 g MeIMO NTs, add 0.025 g iron (III) chloride hexahydrate in 15 ml of double-distilled water). The uniform stirring of the mixture insures a higher homogeneity in the final structure.

The resulting mixture was then filtered with 0.02 μ filter, washed with bi-distilled water, and dried at 120 °C for 48 hours.

3.3 Characterization and textural properties of Fe-MeIMO

3.3.1 TEM characterization

Figure 3-1(a-b) reports the HR-TEM images of MeIMO NTs with two different magnifications. The network of bundles of NTs is observable at lower magnification (Figure 3-1a), whereas, at higher magnification, bundles of parallel NTs with considerable long lengths are detectable.

Figure 3-1(d-e) reports TEM and dark field-TEM images of Fe-1.4-MeIMO-IE NTs. Figure 3-1d shows the series of bundles of parallel NTs aligned in different directions and with more disorder as compared to MeIMO NTs, mainly due to post iron loading, which induces disorder in the NTs arrangement in bundles. The *inset* to Figure 3-1d displays a detail of a terminal region of bundles, showing the hexagonal arrays of NTs. The red arrows in Figure 3-1e point out the occurrence of some Fe-containing clusters at the outer surface of NTs in Fe-1.4-MeIMO-IE sample. For a better observation of such clusters in the structure of NTs, the dark field HR TEM was also performed on the mentioned sample. In dark field –TEM, diffracted beams strongly interact with the specimen; therefore, it provides useful information for observation of planar defects, stacking faults and/or particle size. According to dark field-TEM image (*inset* of Fig. 1e), Fe-containing clusters with an approximate size of 4-5 nm are detectable (red arrows).

Figure 3-1 (g-h) reports TEM and dark field-TEM images of Fe-1.4-MeIMO-DS NTs. The Fe-1.4-MeIMO-DS NTs, show the same morphological features of MeIMO NTs (Figure 3-1g), however, some clusters are detected (Figure 3-1h, red arrows). Furthermore, the presence of an amorphous phase is also observable (Figure 3-1h, white arrow). The *inset* of Figure 3-1h shows a dark field-TEM picture of the related sample, with the slightly smaller Fe-containing clusters (~ 4 nm) with respect to Fe-1.4-MeIMO-IE sample.

Figure 3-1 (c,f and i) correspond to selected area diffraction pattern (SAED) of MeIMO, Fe-1.4-MeIMO-IE and Fe-1.4-MeIMO-DS, respectively. As discussed in a previous chapter, SAED pattern is related to structure crystallinity. The first reflection ring corresponds to the scattering of individual NTs, which has a comparably sharp reflection for MeIMO (Figure 3-1c) and Fe-1.4-MeIMO-IE (Figure 3-1f); however for Fe-1.4-MeIMO-DS (Figure 3-1i) is broader. The second ring corresponds to parallel NTs within a bundle, which is identical in all three samples. The last reflection corresponds to center-to-center NTs separation and

could be taken as characteristic signature that differentiate the NTs from any amorphous phases [68, 103]. This ring is more blurred in the direct synthesis sample, probably due to the formation of some amorphous phase, due to high amount of iron.

Figure 3-2 (a-c) correspond to EDX (Energy-dispersive X-ray) analysis of MeIMO, Fe-1.4-MeIMO-IE and Fe-1.4-MeIMO-DS, respectively. According to the EDX analysis, the samples show the same Al:Si atomic ratio of 2:1, which is in agreement with the NTs structure.

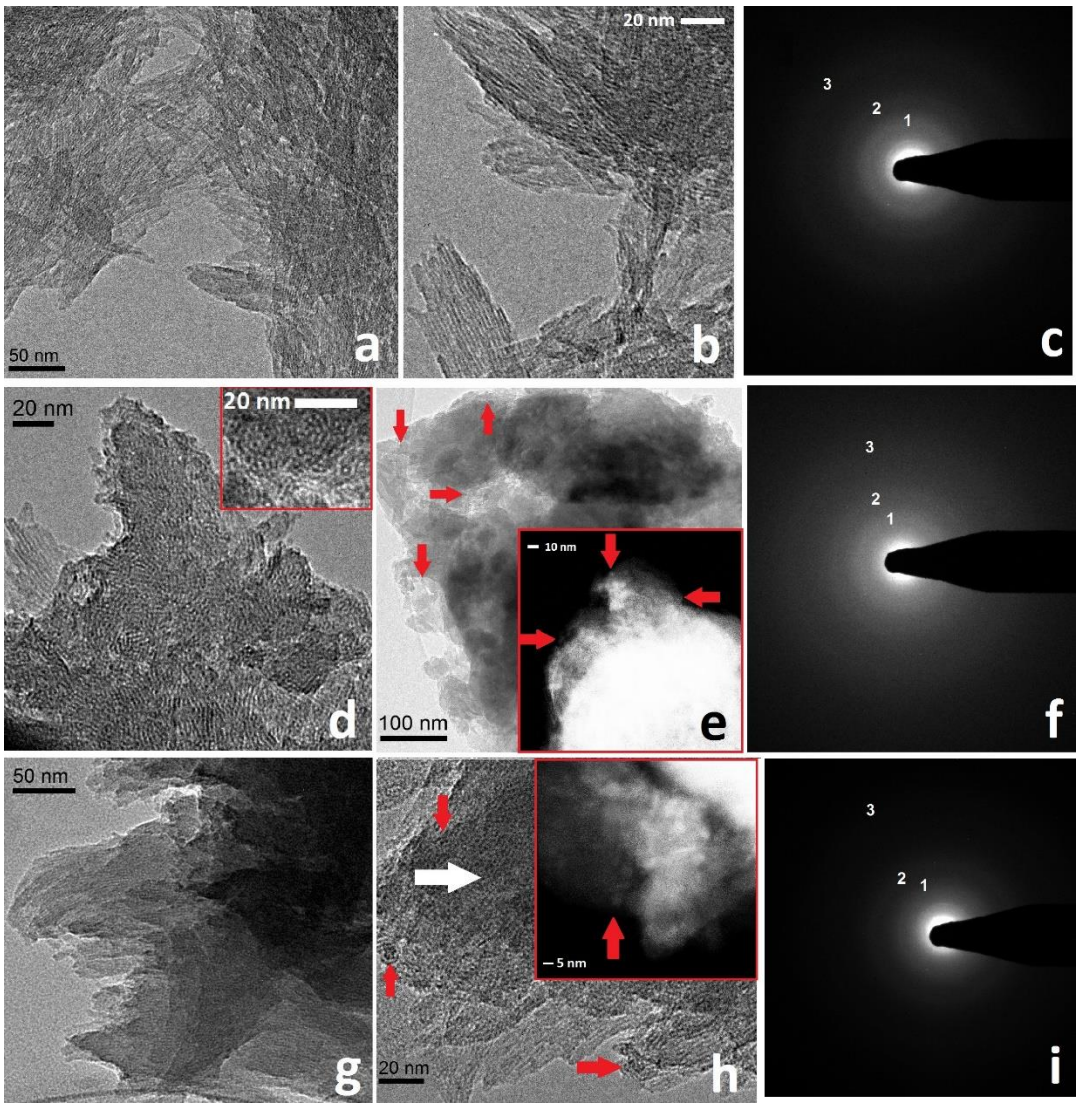

Figure 3-1: HRTEM images of MeIMO bundles (a), formed by parallel NTs (b) and corresponding SAED pattern (c). HRTEM images taken from Fe-1.4-MeIMO-IE (sections d and e), forming the hexagonal arrays (*inset* to section d), black filed-TEM of iron-containing clusters (*inset* to section e) and corresponding SAED pattern (f). The HRTEM images taken from Fe-1.4-MeIMO-DS (sections g and h), black filed-TEM and particle size of iron-containing nanoclusters (*inset* to section h) and corresponding SAED pattern (i)

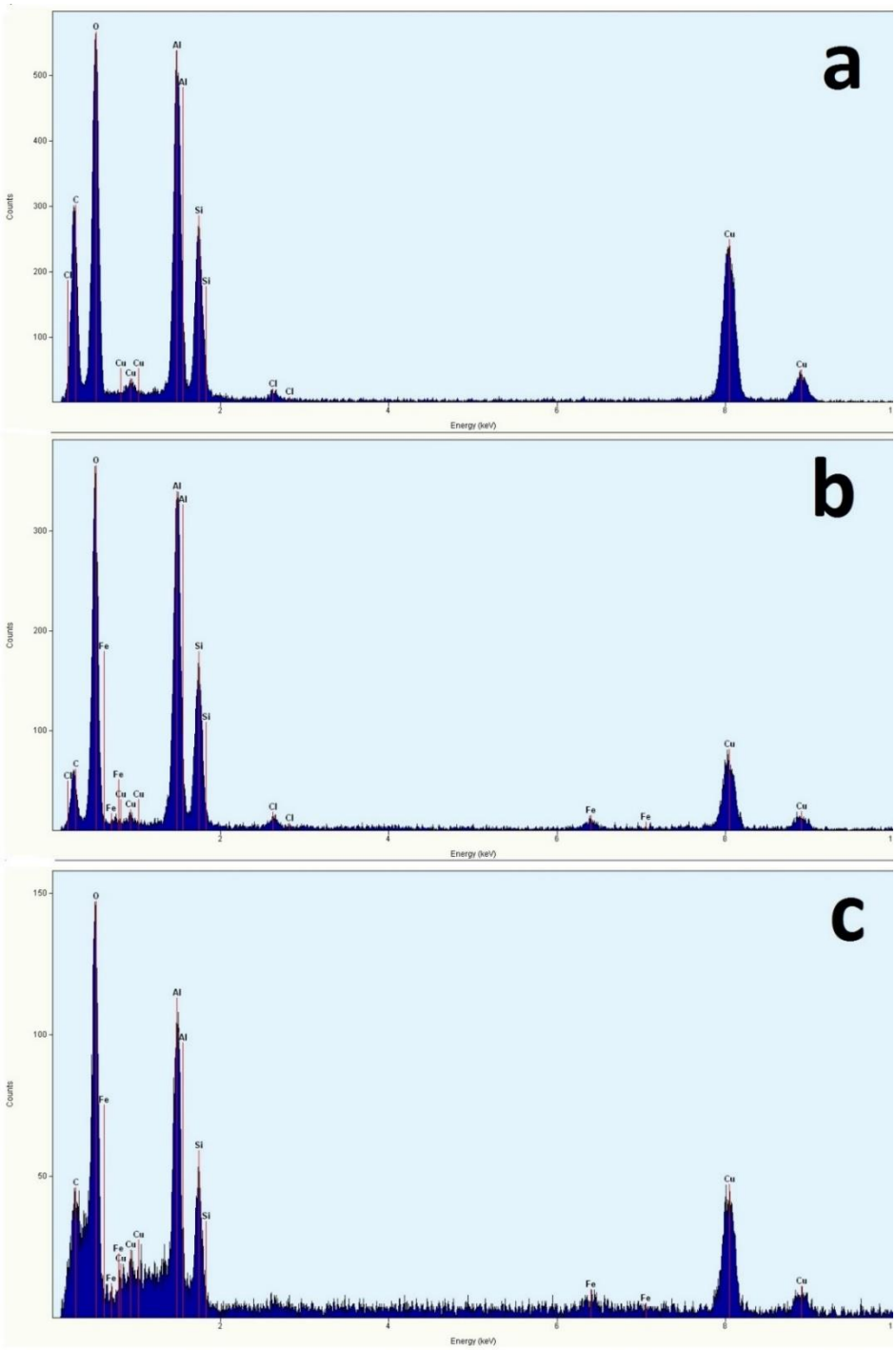

Figure 3-2: EDXS (Energy-dispersive X-ray-spectroscopy) analysis of MeIMO (a), Fe-1.4-MeIMO-IE (b) and Fe-1.4-MeIMO-DS (c)

3.3.2 Powder X-ray diffraction (XRD)

Figure 3-3 reports powder XRD patterns of the studied samples, corresponding to a hexagonal packing of NTs. The most intense peak is due to the d_{100} reflection, from which the cell parameter a, corresponding to the center-to-center distance between two aligned NTs, is calculated (Table 3-1).

Broad peaks at higher angles are assigned to d_{001} and d_{211} reflections due to the repetition of MeIMO structural units along the tubes [2, 25, 48, 119, 141]. Samples obtained by IE show a shift in the d_{100} peak position to lower angles with respect to MeIMO (2θ= 3.42°, 3.38° and 3.10° in MeIMO, Fe-0.7-MeIMO-IE and Fe-1.4-MeIMO-IE, respectively), with a corresponding increase of the cell parameter *a* (Table 3-1). Upon Fe^{3+}/Al^{3+} IS, NTs inner diameter is indeed expected to increase, due to the larger Shannon radius of octahedral (Oh) Fe^{3+}(r= 0.645 Å) with respect to Al^{3+} (r= 0.535 Å) (Curves 3 and 5) [24, 140]. Such effect was instead not observed in samples obtained by DS (curves 2 and 4). The same effect (i.e. a cell parameter decrease in samples obtained by direct synthesis) was observed in Fe-doped imogolite NTs, due to the presence of chloride ions replacing (larger) perchlorates ions that remained trapped between NTs in the dry powders (18). The washing procedure after ionic exchange likely allows the removal of such ions, leading to a larger cell parameter. However, it should be noted that XRD patterns vary slightly from sample to sample depending on sample alignment and adsorbed water content in ambient condition [82, 104]. Furthermore, incorporation of Fe atoms in tube structure without alteration of MeIMO structure is limited. According to studies done by Shafia *et al.* on Fe doped imogolite NTs [24, 156] obtained by direct synthesis, increasing the amount of Fe ≥1.4 wt%, resulted in a decrease of the characteristic d_{001} peak of imogolite in XRD pattern, showing that increasing the iron content will hinder the formation of NTs in fair agreement with the observations by Ookawa about iron doped imogolite NTs [21, 22]. The same consideration can be done for samples obtained by direct synthesis method with higher amount of iron (curve 4) (1.4 wt%; Fe-1.4-MeIMO-DS), in which the intensity of first peak is slightly lower than the original MeIMO and Fe-0.7-MeIMO-DS samples, as well as, less repetition of structural units along the NTs (the intensity of d_{001} and d_{211} reflections). These results can be attributed to the high amount of amorphous phase, coming from unreacted precursor in agreement with SAED pattern and ^{29}Si MAS NMR analysis, which confirm indeed the presence of the trace of silanols condensation in the Fe-1.4-MeIMO-DS. XRD patterns of ion exchanged samples (curves 2 and 3), indeed, show that the hexagonal packing is maintained, since the characteristic peaks of imogolite NTs are observed.

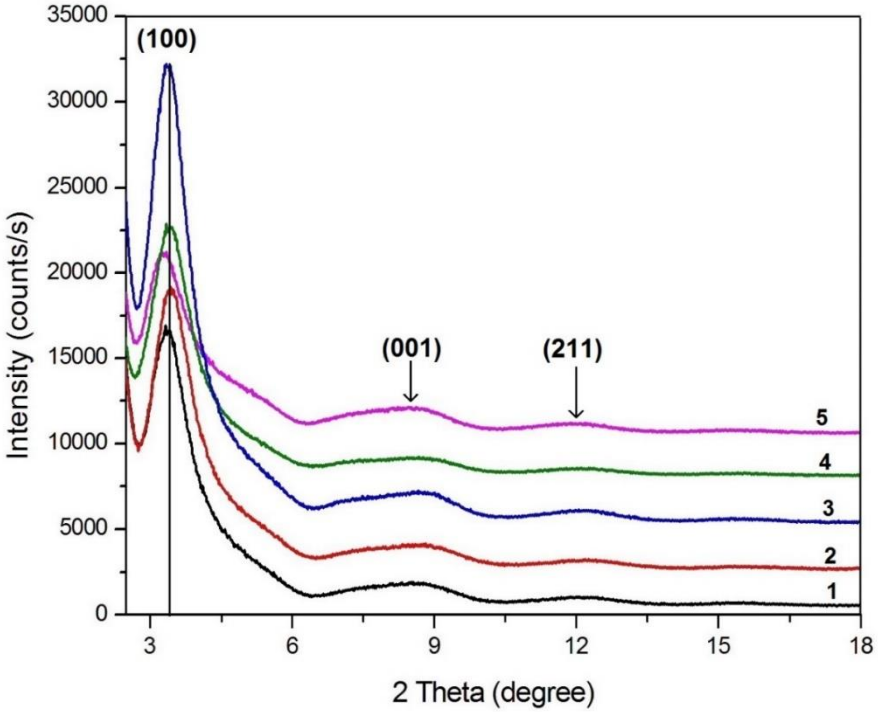

Figure 3-3: Low-angle XRD patterns of MeIMO (1), Fe-0.7-MeIMO-DS (2), Fe-0.07-MeIMO-IE (3), Fe-1.4-MeIMO-DS (4) and Fe-1.4-MeIMO-IE (5)

3.3.3 Porosity characterization by N_2 adsorption/desorption isotherms

To determine the BET SSA (Brunauer- Emmett-Teller Specific Surface Area) and porous volume reported in Table 3-1, N_2 isotherms were measured at -196 °C on samples previously out-gassed at 250 °C, a temperature allowing the removal of water and other atmospheric contaminants still preserving NTs structure [8, 143]. NL-DFT (Non Local Density Functional Theory Method) was used to determine the Pores Size Distributions (PSDs), by adopting a N_2-silica kernel for cylindrical pores.

N_2 sorption at -196 °C (Figure 3-4a) gives rise with all the studied samples to type IV isotherms with limited hysteresis loops, as typical of microporous systems with some mesoporosity. All iron doped samples (0.7wt% and 1.4 wt% with IE and DS) have larger mesopores volume and SSA values with respect to MeIMO

(Table 3-1), likely due to the fact that Fe-doping mainly affects the outer surface of NTs and especially C mesopores [24]. This is confirmed by PSDs curves, showing an increase of volume due to mesopores larger than 3.0 nm (Figure 3-4b).

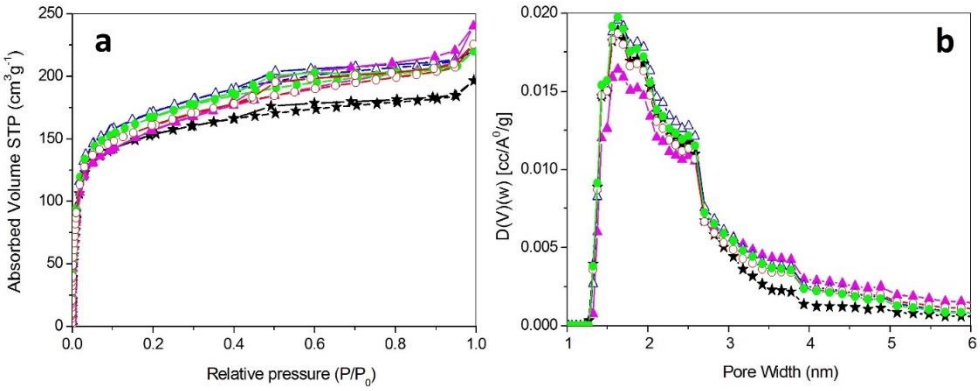

Figure 3-4: N_2 isotherms at -196 °C (a) and corresponding PSDs (b), as obtained by applying the NL-DFT method, of samples: MeIMO (stars), Fe-0.7-MeIMO-IE (hollow triangles), Fe-1.4-MeIMO-IE (triangles), Fe-0.7-MeIMO-DS (hollow circles) and Fe-1.4-MeIMO-DS (circles) samples

Table 3-1: Samples textural properties as derived by XRD patterns and N_2 sorption isotherms at -196 °C.

Samples	Fe wt%	d_{100} nm (±0.01)	a (nm) [a]	BET SSA, ($m^2 g^{-1}$)	Total Pore Vol, ($cm^3 g^{-1}$)	Micropore Vol [b] ($cm^3 g^{-1}$) [b]
MeIMO	---	2.58	2.98	557	0.30	0.14
Fe-0.7-MeIMO-IE	1.4	2.61	3.00	617	0.33	0.14
Fe-1.4-MeIMO-IE	0.7	2.68	3.10	565	0.33	0.10
Fe-0.7-MeIMO-DS	0.7	2.57	2.97	576	0.32	0.11
Fe-1.4-MeIMO-DS	1.4	2.59	2.99	605	0.32	0.13

(a) Hexagonal cell parameter as obtained by applying the equation $a = {2d_{100}}/{\sqrt{3}}$

(b) As calculated by applying the *t*-plot method

3.3.4 Nature of iron species as studied by UV-Vis spectroscopy

DR UV-Vis spectra of dehydrated samples are reported in Figure 3-5a MeIMO has, as expected, a negligible absorption in the UV-Vis region (curve 1).

All Fe containing samples (0.7wt% and 1.4 wt% with IE and DS) have strong absorption bands both below and above 300 nm. According to the literature, bands around 240 and 290 nm are due to charge-transfer (CT) transition between O^{2-} and isolated Fe^{3+} ions in different coordination (tetrahedral or higher). The 240 nm band likely implies that besides Al^{3+}/Fe^{3+} IS, another type of ionic exchange occurred: previous theoretical work [129] has indeed postulated the occurrence of some defects/vacancies at both sides of MeIMO NTs wall, which could lead to the formation of some *Td* Fe^{3+} sites upon ionic exchange. Absorption bands in the 300-400 nm range and above 400 nm are assigned to d-d transitions of Fe^{3+} ions in oligomeric clusters (Fe_xO_y) and Fe_2O_3 particles, respectively [157-160].

UV–Vis spectra point out the preferential formation of clusters and Fe_2O_3 particles by IE method especially at higher iron content, in agreement with what was observed by Shafia *et al.* [24] with Fe-doped imogolite. Furthermore, broadening of UV-vis spectrum over 290 nm contributed to the small Fe_xO_y oligomeric clusters and Fe_2O_3 particles that their absorption bands partially overlap in the high-wavelength [158, 159]. In DS samples, however, a higher proportion of isolated Fe^{3+} sites is observed with respect to clusters (curves 2 and 4). If the same iron content is considered, more intense bands, related to isolated Fe^{3+}, are observed by DS, as well as more intense band related to the formation of small Fe_xO_y oligomeric clusters and Fe_2O_3 particles are observed in IE method. The occurrence of some Fe_2O_3 clusters in both IE and DS samples indicates that the actual isomorphic substitution of Fe for Al in the MeIMO structure is lower than that corresponding to 1.4 % by weight, in agreement with the literature [24].

The presence of isolated Fe^{3+} sites in Fe-x-MeIMO-IE samples indicates that Al bridges at the outer surface of NTs are reactive in water, and consequently the following reaction takes place [24]:

$$[Al(OH)Al]_s + Fe(H_2O)_6^{3+} \rightarrow [Fe(OH)Al]_s + Al(H_2O)_6^{3+} \quad (3\text{-}1)$$

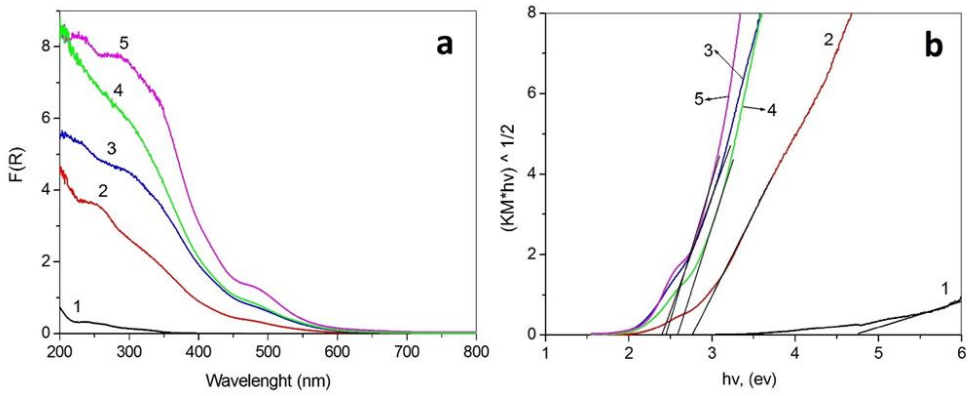

Figure 3-5:DR UV-Vis spectra (a) and corresponding Tauc plots (b) of MeIMO (1), Fe-0.7-MeIMO-DS (2), Fe-0.7-MeIMO-IE (3), Fe-1.4-MeIMO-DS (4) and Fe-1.4-MeIMO-IE (5)

Reaction (3-1) was already observed in iron-doped imogolite, since such NTs structure is able to exchange Al^{3+} and Fe^{3+} ions dynamically in water solution, rendering ionic exchange an alternative method with respect to more complicated direct synthesis procedures.

Figure 3-5b reports the corresponding Tauc's plot, from which the band-gap of the materials can be extrapolated: MeIMO is an insulator with an energy band gap E_g =4.7 eV (curve 1). With Fe-containing samples, band gap values are as follows: E_g = 2.4 eV for Fe-0.7-MeIMO-IE and Fe-1.4-MeIMO-IE, and E_g = 2.7 and 2.6 eV for Fe-0.7-MeIMO-DS and Fe-1.4-MeIMO-DS, respectively. Isomorphic substitution of iron reduces the band gap of MeIMO, especially by IE, though a precise determination of the band gap is hampered by the presence of Fe_2O_3 clusters along with substitutional iron.

3.3.5 Nature of iron species investigated with EPR spectroscopy

EPR spectroscopy has been extensively used to identify the state of iron species in molecular structures and in the solid state, since it is an efficient technique for identification of isolated Fe^{3+} species of different coordination geometry [161-165], as well as Fe_xO_y clusters of different degrees of aggregation by analysis of the mutual magnetic interactions of the Fe sites [161]. Furthermore, EPR is considered as a technique of choice for characterization of geometrical and electronic peculiarities of different isolated Fe^{+3} ions at very low iron concentrations (which is often not possible to analyze by other techniques *e.g.* Mössbauer spectroscopy).

In order to get deeper insight in the state of iron in MeIMO structure, the two samples with lower amount of iron loadings (0.7 wt% of Fe) were studied, as they were expected to have lower amount of iron oxo/hydroxide clusters.

For better observation of the paramagnetic behavior of iron species, EPR signals were recorded both a room temperature (r.t.) and low temperature (l.t. at -153 °C) with the corresponding sample powder in 1 mm quartz tubes.

EPR analysis of both samples at l.t. show typical signals at effective g_{eff} values of 2, 4.3, and 6 (Figure 3-6c). These signals were frequently detected in Fe-ZSM-5 and with Fe^{3+} ions in other solid matrices [166-170].

The number and position of EPR transitions for isolated Fe^{3+} ions highly depends on the local ligand-field symmetry of the sites (reflected by the magnitude of the zero-field splitting (zfs) parameters, E and D), as well as the possible magnetic interactions between them [171]. Therefore, from the signal position alone it is not possible to obtain the exact coordination of the respective Fe ions (octahedral or tetrahedral), since the signal position is driven by the magnitude of both D and E, *i.e.* the extent of distortion of the Fe coordination. Such distortion can arise from both tetrahedral and octahedral coordination. E/D parameter has a limited range (0-1/3), and shows the distortion degree of rhombic structure in the electronic environment [161].

The signals at g ≈ 4.5 and at g ≈ 6 arise from the $|-\frac{1}{2}> \leftrightarrow <\frac{1}{2}|$ transition of isolated Fe^{3+} sites in strong rhombic (D > hν, E/D = $\frac{1}{3}$, g ≈4.3) or axial distortion (D > hν, E/D = 0, g≈ 6), respectively [161]. This implies that a Fe^{3+} species giving rise to a line at g ≈ 4.3 is more strongly distorted with respect to a Fe^{3+} site represented by a signal at g ≈ 6, due to the difference in the magnitude of the parameter E, which characterizes the additional asymmetry [166, 172]. In zeolites, g ≈ 4.3 is assigned to Fe^{3+} sites incorporated in tetrahedral framework positions, whereas a line at g ≈ 6 is attributed to isolated Fe^{3+} species in higher coordination [161, 166-169, 173]. The signal at g ≈ 2 is assigned to either isolated Fe^{3+} in high symmetry (D, E ≈ 0) or Fe_xO_y clusters [161].

In aluminum silicates, Fe^{+3} ions are in high-spin electronic configuration, (S = 5/2), since the possible ligands are oxygen, OH or water molecules (which are weak field ligands). According to previous studies, the prominent peak at g_{eff} = 4.3 in EPR spectra (Figure 3-6) is assigned to the presence of isolated Fe^{3+} ions in high-spin state, likely corresponding to species absorbing at 290 nm in the DR-UV–Vis spectra [166].

As expected for pure paramagnetic behavior according to the Curie-Weiss law, the intensity of two peaks at 4.3 and 6 increases with decreasing temperature. The intensity loss of these two peaks at (r.t.) is strongly suggesting a shorter relaxation time for the corresponding Fe^{3+} species (Figure 3-6a and 3-6b).

In contrast, the intensity of the line at $g \approx 2$ does not markedly increase upon cooling (Figure 3-6a and 3-6b). This suggests that the Fe^{3+} sites responsible for this signal are coupled by antiferromagnetic interactions within Fe_xO_y clusters, which reduce the number of unpaired spins contributing to the EPR signal. The presence of Fe_xO_y clusters in these two samples has been confirmed by previous UV-Vis spectra (Figure 3-5a).

Therefore, the temperature dependence of the EPR signal intensity gives significant information on the presence of magnetically coupled phases [174-177]. While well-ordered crystalline α-Fe_2O_3 is antiferromagnetic below T_N =960 K (TN: Neel temperature) and, therefore, not EPR-active, it has been shown that nanoparticles of α-Fe_2O_3 ($d \approx 3$ nm) do give rise to an EPR signal below T_N due to incomplete compensation of the spin moments [161, 174].

According to Figure 3-6c, by comparing the relative intensity of the g_{eff} = 4.3 for both iron doped samples at low temperature (-153 °C), the intensity of this signal is higher in Fe-0.7-MeIMO-DS, with respect to Fe-0.7-MeIMO-IE. Previous studies Fe-iron doped imogolite NTs imply that Fe_xO_y clusters /particles in the structure (with the $g_{eff} \approx 2.0$ -2.3) strongly interact with Fe^{3+} isolated iron sites, hampering the evaluation of the relative spin concentration of clustered and /or isolated Fe^{3+} sites [166, 178, 179]. Therefore, in this case, there is a high anisotropy in the transition probabilities of Fe^{3+} high-spin states. Comparison of UV-Vis spectra (Figure 3-5a) and EPR signals (Figure 3-6c) show that by ionic exchange more Fe formed oligomeric clusters and/or Fe_2O_3 particles than isolated sites, which may negatively affect the intensity of corresponding peak at g_{eff} = 4.3 in the EPR analysis. Summarizing, these results show that isolated Fe^{3+} species are much more abundant in Fe-0.7-MeIMO-DS.

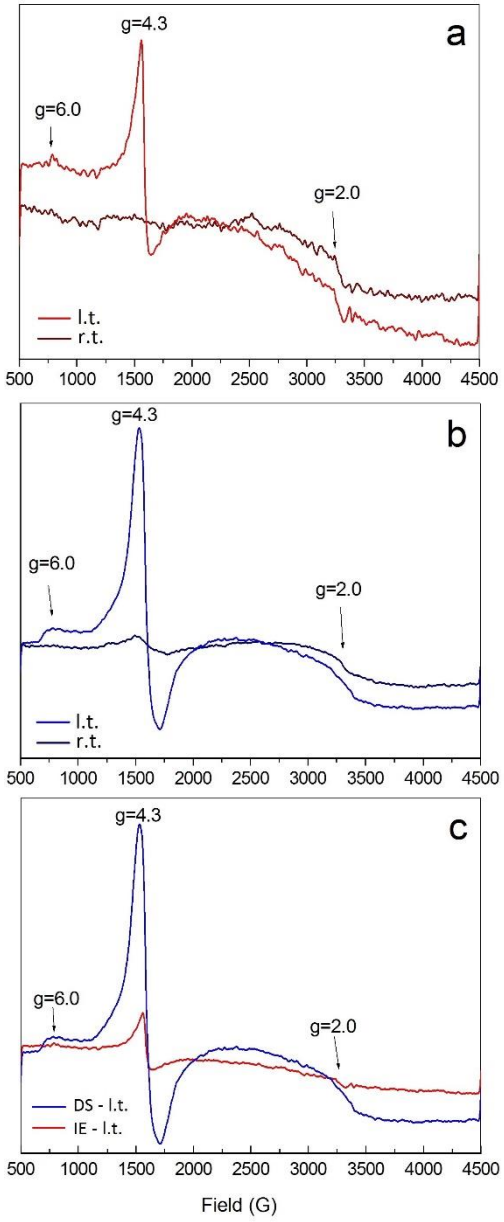

Figure 3-6: EPR spectra of (a) Fe-0.7-MeIMO-IE in r.t. and l.t. (-153 °C), (b) Fe-0.7-MeIMO-DS in r.t. and l.t. (-153 °C) and (c) Fe-0.7-MeIMO-DS (blue curve) and Fe-0.7-MeIMO-IE (red curve) at -153 °C

3.3.6 Elemental analysis

The Fe-0.7-MeIMO-DS sample was characterized by elemental analysis (Table 3-2). The results show an exact amount of 0.7 wt% loading in the NT structure, although a slight excess of iron (1 wt%) was loaded in the syntheses bath.. Furthermore, the Al/Si molar ratio is 0.496, which is in fair agreement with the Al/Si ratio for both natural and synthetic imogolite NTs [180].

Table 3-2: Elemental analysis of Fe-0.7-MeIMO-DS sample

Element	Unit	amount
Al	mass-%	27.8
Si	mass-%	13.8
Fe	mass-%	0.69

3.3.7 MAS ^{13}C, ^{27}Al and ^{29}Si NMR on iron doped samples

Solid-state ^{13}C, ^{27}Al and ^{29}Si MAS NMR measurements were carried out in order to investigate the coordination of both silicon and aluminum atoms in methyl-imogolite samples.

As mentioned in chapter 2, ^{13}C NMR shows a chemical shift at *ca.* -1.35 ppm, which has the value reasonably close to ^{13}C NMR of the reference compound, TEMS (Triethoxymethylsilane), around 0 ppm (Figure 3-7). In the Fe-1.4-MeIMO-DS, however, an additional small peak with a chemical shift of *ca.* 50.0 ppm is detectable, assigned to ethoxy groups (δ= 48.8 ppm) stemming from the silicon precursor. The same peak has been observed in ^{13}C NMR of modified imogolite type NT obtained by using methyltrimethoxysilane precursor and has been assign to C^4 in the methoxy group coming from the precursor [10].

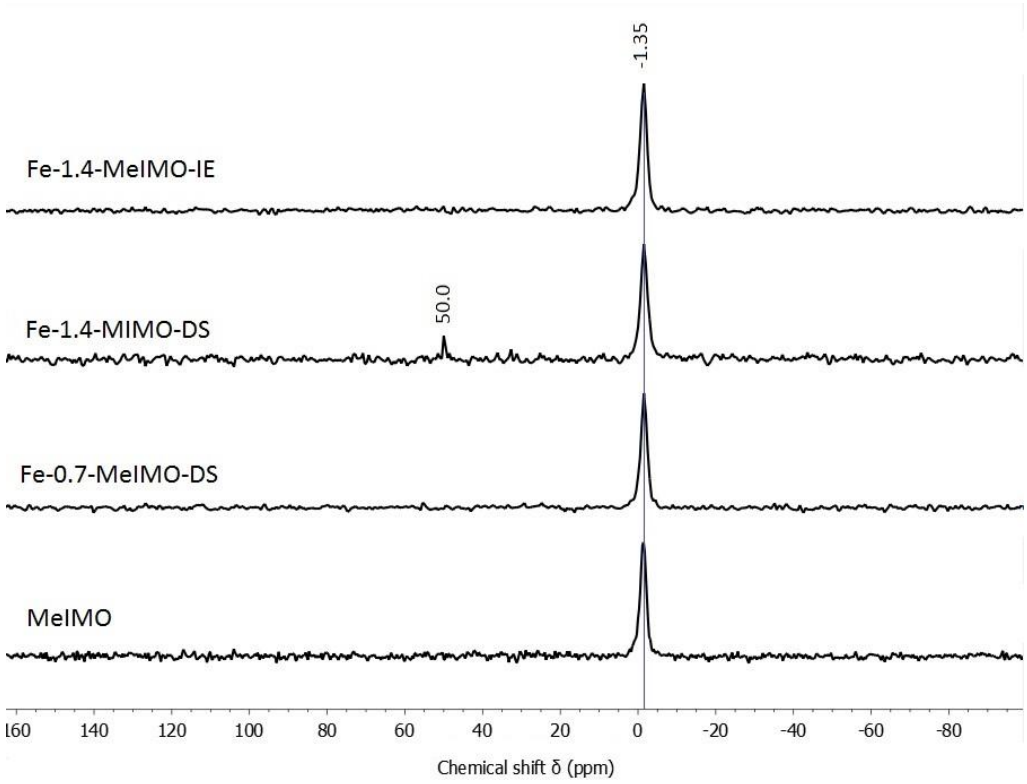

Figure 3-7: Solid-state ^{13}C-MAS NMR of MeIMO and iron doped MeIMO NTs

^{29}Si MAS NMR spectra show a sharp peak centered at chemical shift value of at δ (-43 ppm) for all samples (Figure 3-8), which is typical for tetrahedral silicon atoms bonded to one carbon and three aluminum atoms through oxygen bridges at the inner surface of NTs [9, 13].

The spectra also show a minor shoulder at δ (-78 ppm) for all samples, which is not commonly found in other aluminosilicate frameworks. This chemical shift is assigned to the unique Q^3(6Al) silicon framework, probably due to the limited occurrence of an amorphous phase in the structure [50, 76]. Furthermore, Fe-1.4-MeIMO-DS a extra minor shoulder at δ (-100 ppm), assigned to Q^4(6Al) and considered the contribution from the small number of condensed silanols groups [50, 76]. The *ins*et of Figure 3-8, shows a magnification of the main peak at -43 ppm. MeIMO and Fe-0.7-MeIMO-DS show the same spectra, whereas by increasing the amount of iron in Fe-1.4-MeIMO-IE, disorder induced by ion exchange in the structure slightly affects the shape of the peak. The widest peak belongs to Fe-1.4-MeIMO-DS, which indicates the different environment around Si atoms, due to heterogeneity in the sample structure.

The results of ^{13}C and ^{29}Si MAS NMR, along with the TEM and corresponding SAED pattern of Fe-1.4-MeIMO-DS, confirm that a higher amount of iron in the synthesis bath affects the structural stability in formation of the MeIMO NTs, by imposing strain energy into the structure, hence, hinders the formation of NTs. These results are in agreement with previous findings on iron doped imogolite NTs, where Fe may isomorphically substitute for Al up to 1 wt. %, whereas by ionic exchange method and higher Fe loadings (>1 wt. % Fe), Fe oxo-hydroxide clusters formation occurs along isomorphic substitution (Figure 3-5a) [21, 23, 24, 85].

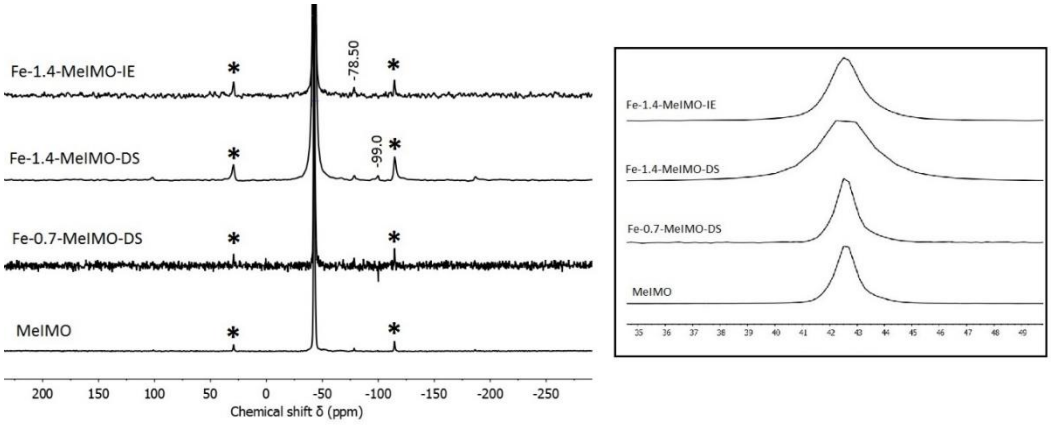

Figure 3-8: Solid-state ^{29}Si-MAS NMR of MeIMO and iron doped MeIMO NTs

The ^{27}Al MAS NMR spectra (Figure 3-9) show a major single shift, approximately at 7.5 ppm for all samples (MeIMO, Fe-0.7MeIMO-DS, Fe-1.4-MeIMO-DS and Fe-1.4-MeIMO-IE), indicating the presence of octahedral aluminum close to that found for gibbsite (δ = 7.8 ppm) [152]. The small shoulder around 61.7 ppm presented in *inset* of Figure 3-9, along with a small contribution from the second spinning- sideband of the major peak, is attributed to small proportion of four-coordinated aluminum atoms, probably coming from an amorphous phase within the structure of NT [143].

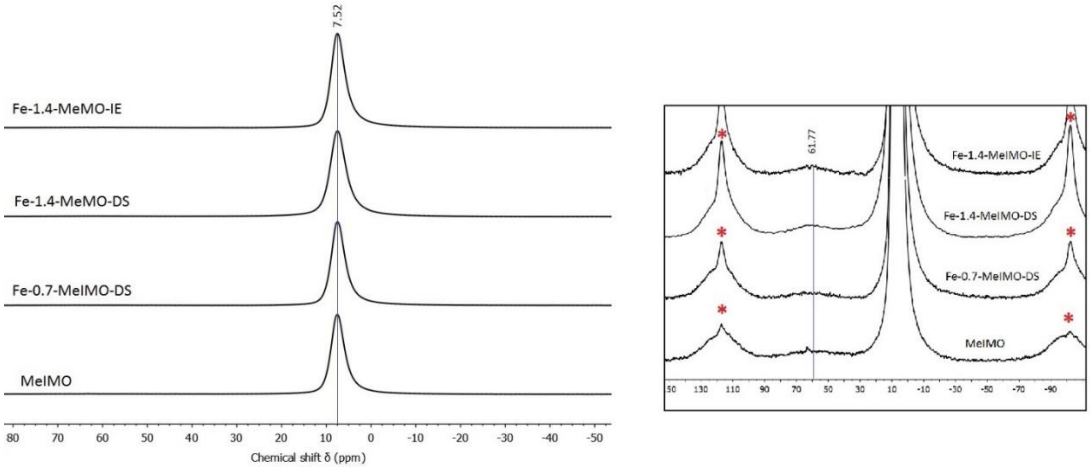

Figure 3-9: Solid-state ^{27}Al-MAS NMR of MeIMO and iron doped MeIMO NTs

3.4 Conclusion

This is the first report on Fe-doping of hybrid organic-inorganic NTs of the imogolite-type (methyl-imogolite; MeIMO) with two weight percent Fe (0.7 and 1.4 wt %). It is shown that doping with iron may occur both by direct synthesis, *i.e.* by addition of Fe^{3+} species in the synthesis mixture, or by ionic exchange of preformed NTs in aqueous phase.

The resulting materials, however, show some different properties, mainly concerning the state of Fe-species. Direct synthesis (with 0.7 wt% of Fe loading) seems to favor actual isomorphic substitution of Fe^{3+} for Al^{3+}. Comparison between Fe-0.7-MeIMO-DS and Fe-0.7-MeIMO-IE show that isolated Fe^{3+} species are more abundant in Fe-0.7-MeIMO-DS, whereas by ionic exchange iron tends to form oligomeric iron oxo/hydroxide clusters or Fe_2O_3 particles rather than isolated sites.

By increasing the amount of iron up to 1.4 wt%, in direct synthesis method (Fe-1.4-MeIMO-DS), some Fe_xO_y oligomeric clusters and Fe_2O_3 particles were detected in black field-TEM. Some traces of an amorphous phase deriving from unreacted precursors and/or unsuccessful synthesis process, due to perturbing the synthesis condition, were detected by XRD, SAED pattern and ^{13}C and ^{29}Si MAS NMR.

On the other hand, in ion exchange method, the original NTs structure is preserved. However, post loading of iron mainly affects the outer surface of NTs (C surface). Consequently, it induces some disorders in the NTs bundles, which is detectable in HR-TEM spectra, as well as the formation of larger mesopores and higher SSA values. Furthermore, formation of small Fe_xO_y oligomeric clusters and

Fe_2O_3 particles are more likely by this method, as observed in dark-filed TEM and also proofed by UV-Vis analysis.

Although a simpler experimental procedure, post-synthesis ionic exchange leads to a higher formation of Fe_xO_y clusters and Fe_2O_3 particles. Nonetheless, isomorphic substitution also occurs by ionic exchange. The better dispersion of Fe^{3+} ions in the synthesis mixture during direct synthesis is probably the main factor affecting the preferential formation of isolated (octahedral) Fe^{3+} sites in the NT structure.

Independently of the synthesis method, the presence of Fe has a significant effect on decreasing the band gap of MeIMO (an insulator), and finally a new hybrid materials with semiconducting properties (E_g=2.4 - 2.7 eV) is obtained.

Finally, novel Fe-doped MeIMO NTs have higher porosity and higher surface area, and can be considered as support of catalytic species, and could be considered a novel material in the fields of adsorption and catalysis.

Chapter 4

Dehydration and Dehydroxylation of Bare and Fe-Doped Methyl-Imogolite Nanotubes

4.1 Introduction

The dehydroxylation phenomenon has been observed in aluminosilicate and aluminogermate NTs, within a broad temperature range by TG analysis [25, 113, 153]. By thermal heating, the following successive processes are taking place on the structure of as-synthesized NTs: (i) dehydration, (70-150 °C) (ii) dehydroxylation with subsequent structural collapse above 300 °C, (iii) formation of mullite crystalline phase, due to structure transformation at temperature above 1000 °C.

MacKenzie *et al.* [143] postulated two possible mechanisms for the structural transformation of imogolite NTs by increasing the temperature. According to their studies, the cleavage of the NTs is probably prompted by the loss of some external Al-OH groups [25, 143]. In the first mechanism (mechanism A), the single-tube cleavage occurs with the tube breaking along its axis and formation of Si-O-Si bridges with Al-O-Si-O-Si-O-Al repeating sequence (Scheme 4-1a). The second mechanism (mechanism B), instead, is the vertical cleavage of two adjacent NTs and deals with two tubes cleavage, resulting in dehydroxylation of silanol and aluminol groups of two adjacent NTs. Consequently, Si-O-Al bridges form due to

condensation and formation of Al-O-Si-O-Al-O-Si repeating sequences (Scheme 4-1b).

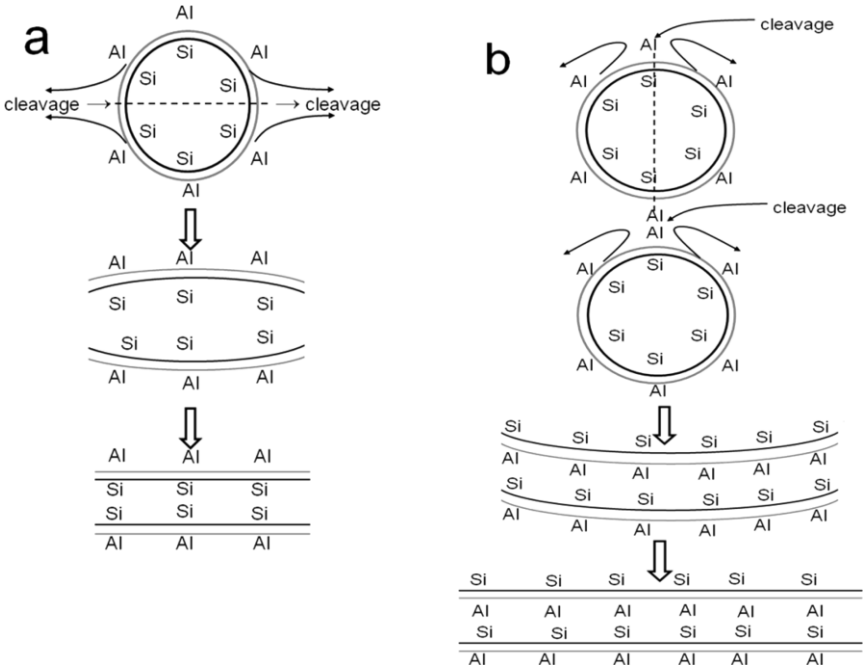

Scheme 4-1:Two possible collapsing mechanisms occur within NTs structure upon heating, [143]: (a) single-tube cleavage (b) two tube cleavage and condensation [25]

Later, Zanzottera el al. (2012) [25] reported an irreversible structural transition and formation of lamellar phase from the collapse of aluminosilicate imogolite NTs starting at around 400 °C. Additionally, they proposed that the structure contains some residual microporous regions derived from unaffected pristine NTs within the layers (Scheme 4-3) [143]. Base on their research on thermal stability of imogolite and MeIMO and Me-Imo-NH_2, with imogolite, the proposed mechanism was the cleavage of NTs across their diameter (Scheme 4-3a), causing the formation of the repeating sequence Al-O-Si-O-Si-O-Al. Nonetheless, with two other hybrid imogolite-like samples the mechanism is much more complex and both mechanisms seem to act sequentially [25].

Comprehensive studies on dehydration, dehydroxylation and rehydroxylation of imogolite NTs have been carried out by Kang *et al.* (2010) [50]. According to their studies, NTs were completely dehydrated under vacuum and at 250 °C, as a prerequisite to partial dehydroxylation process that was previously investigated up

to 450 °C. However, at this temperature also a small proportion of hydroxyl groups was still present and the tubular structure was preserved [50].

Numerical calculations done by da Silva *et al.* (2015) [26] indicated that dehydroxylation of silanols groups at the inner surface of NTs induces deformation of NTs before the recovery of cylindrical structure with the subsequent rehydroxylation of the outer surface. They concluded that dehydroxylation of the silanol groups led to Si–O–Si bonding in the inner surface and cleavage of NTs due to the thermal treatment, and subsequently affected the geometry, band gap and Young's modulus of the material, as shown in Scheme 4-2 [26]. Therefore, controlling the degree of dehydroxylation in the heat treatment process may open the possibility to adjust and control the electronic and mechanical properties of imogolite NTs. According to their SCC-DFTB calculations on the dehydroxylation imogolite NTs [26], the dehydroxylated imogolite is considered a semiconductor with a lower band gap energy with respect to parent imogolite.

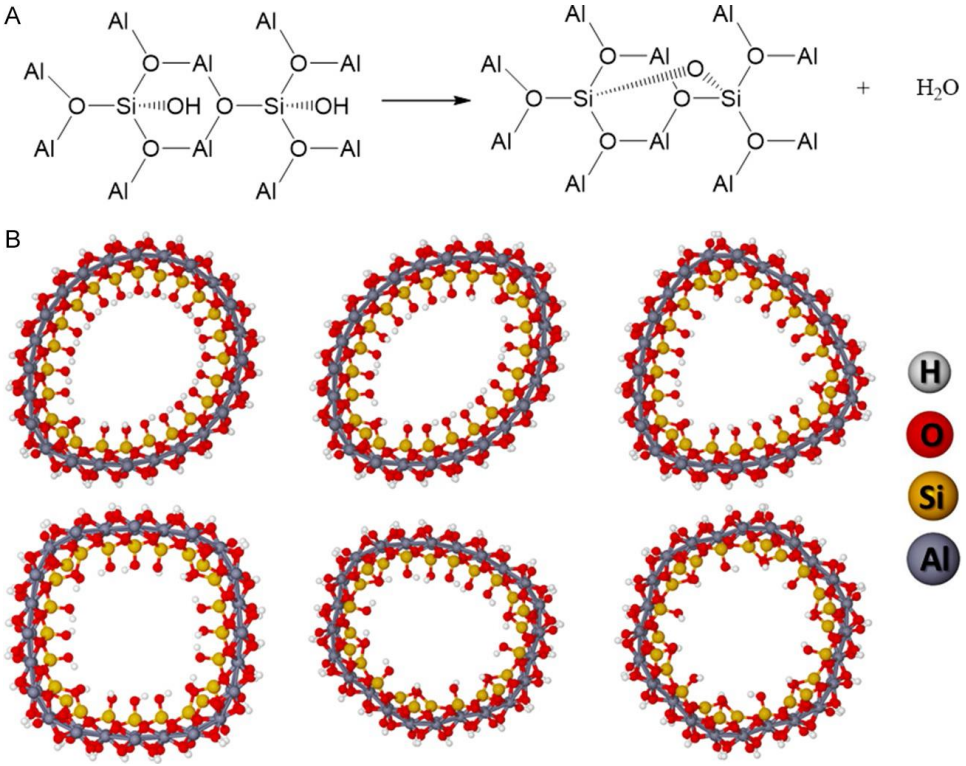

Scheme 4-2: (A) Dehydroxylation reaction occurs in the inner surface of NTs. (B) Optimized structures of the dehydroxylated zigzag (12,0) imogolite NT [26, 180]

Nevertheless, no information is available for the irreversible collapsing mechanism of MeIMO and iron doped MeIMO in different calcination medium. Based on experimental results concerning solid state nuclear magnetic resonance (NMR), powders X-ray diffraction (XRD), thermogravimetric−mass spectrometry (TG-MS), and Fourier transform infrared spectroscopy (FT-IR), in this chapter evidence is reported that these materials do show an irreversible collapse phenomenon, just as imogolite [25], which was previously studied. However, the thermal treatment of NTs in either air atmosphere or under high vacuum may affect the collapsing mechanism, as well as the presence of iron.

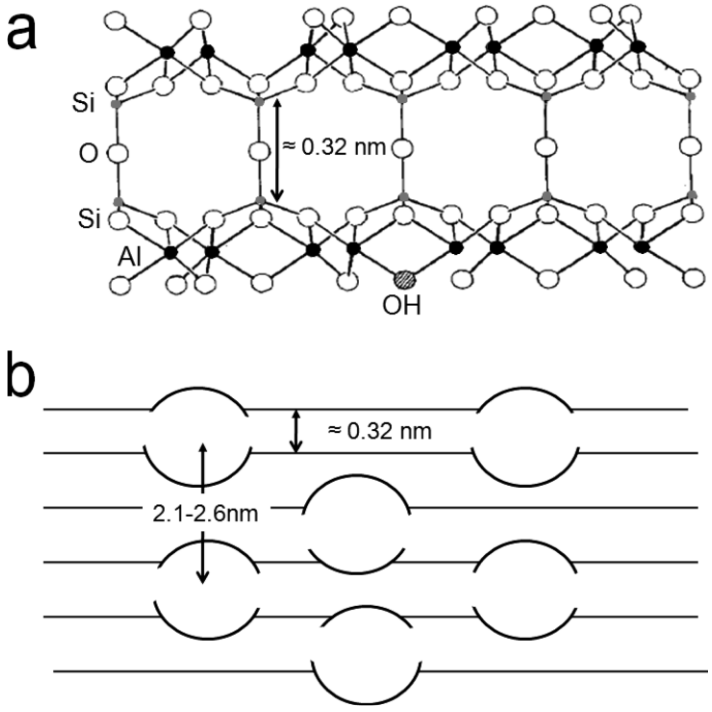

Scheme 4-3: Patches of the layers occur by imogolite NTs cleavage and condensation [143] (a) and proposed buckled structure based on calculated values of d_{100} from XRD peak position and the residual porosity after thermal collapse (b) [25]

4.2 Characterization and textural properties of collapsed NTs

4.2.1 TGA-DTG analysis

Figure 4-1a and 4-1b report the differential thermal analysis (DTA) and thermogravimetric analysis (TGA) of MeIMO, Fe-0.7-MeIMO-IE and Fe-0.7-MeIMO-DS samples. 40 mg of each sample were used for TG analysis from 40 to 500 °C, with 10 °C min^{-1} heating rate and under Ar flow.

According to the curves on Figure 4-1a and 4-1b, two broad endothermic peaks accompanied by a weight loss were observed with all the samples. The first and second endothermic peaks are attributed to the loss of adsorbed water and the dehydroxylation of outer surface by removing of Al-OH-Al groups [25, 50], respectively. MeIMO sample start releasing water above 40 °C, most of water being desorbed at 75 °C, whereas, molecular water desorption from pristine imogolite NTs desorbs at higher temperature (130-150 °C), due to higher hydrophilicity of both inner and outer surface and smaller pores. However, dehydroxylation of the outer surface appears at about the same temperature with MeIMO, in agreement with the similar composition [8, 25].

With MeIMO, a third mass loss is observed at 440 °C, whereas, in iron doped samples the mentioned peak has not been observed. As mentioned in chapter two, this peak has been assigned to the release of oxygen molecules, caused by thermal decomposition of remaining perchlorate species (ClO_4^-) present in the synthesis bath and has been previously observed in DTG and MS analysis of both of imogolite and alumino-germanate imogolite NTs [25, 50, 113].

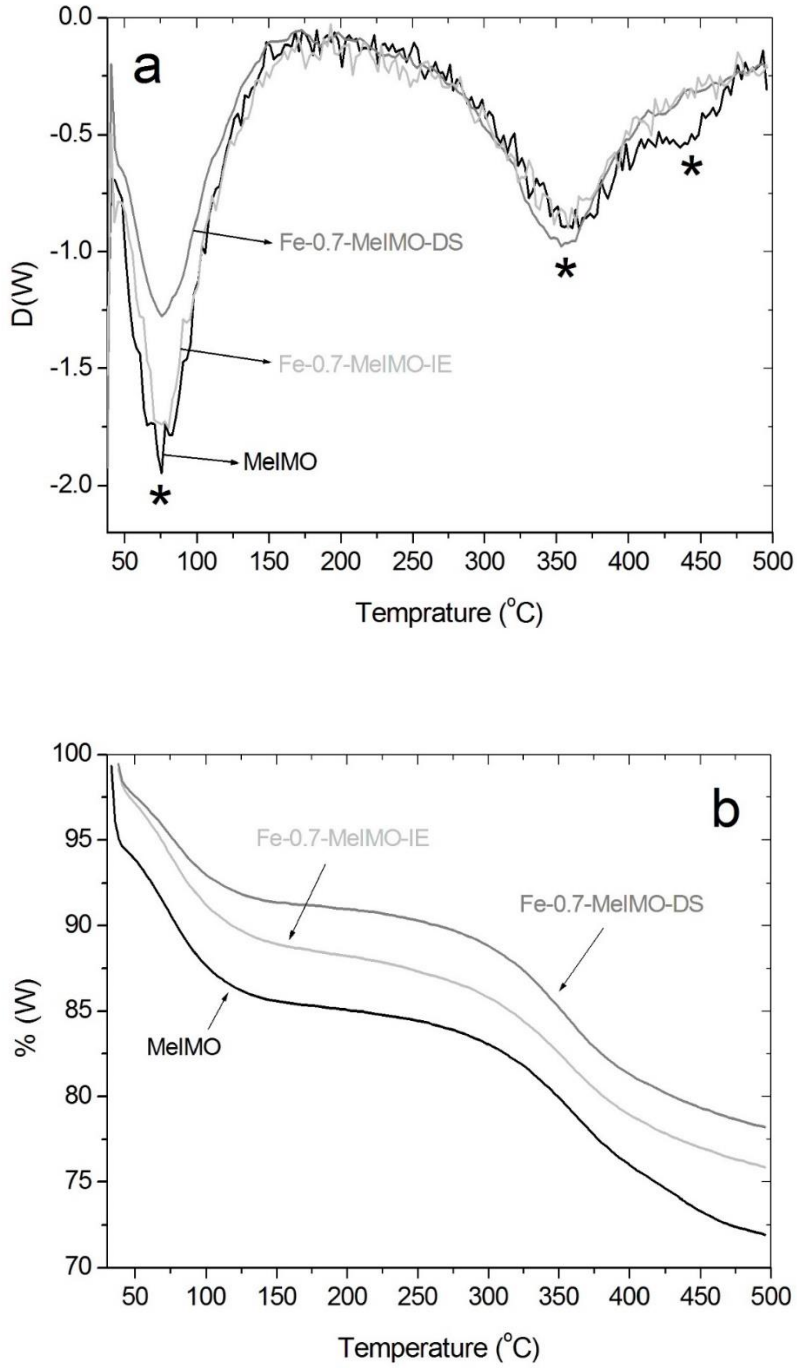

Figure 4-1: Derivative thermogravimetric (DTG; a) Thermogravimetric (TG; b) analysis of MeIMO, Fe-0.7-MeIMO-IE and Fe-0.7-MeIMO-DS

4.2.2 TEM characterization

Figure 4-2 reports the HR-TEM images of MeIMO-c and Fe-1.4-MeIMO-c samples (thermally treated at 500 °C in argon for 4 h; heating rate of 5 °C min^{-1}).

The HR-TEM image of MeIMO-c is reported in Figure 4-2a, and the residual voids derived from the thermal collapse of the structure are detectable. In the *inset* of Figure 4-2a, the proposed structure of collapsed NTs made from patches of layers (yellow arrows) are sealed together. Also, some residual voids coming from unaffected NTs in the thermal treatment process (white arrows) are visible [25, 143]. The distance between layers in the collapsed structure is roughly about 1.0-1.2 nm.

Figure 4-2b reports TEM pictures of Fe-1.4-MeIMO-IE-c sample. The parallel layers and residual voids derived from thermal collapse of NTs are detectable. The *inset* of Figure 4-2b shows the parallel layers with the average distance of *ca.*1.0 nm.

The presence of some clusters are detectable in both samples (Figure 4-2, red arrows). In a case of MeIMO, these clusters may be assigned to carbon residues in structure. The EDXS analysis of sample from different zones, also confirms the presence of carbon in the structure after collapsing (Figure 4-3a). On the other hand, for Fe-1.4-MIMO-IE-c, the same signal may be assigned to either carbon residues and/or Fe-containing clusters (Figure 4-3b).

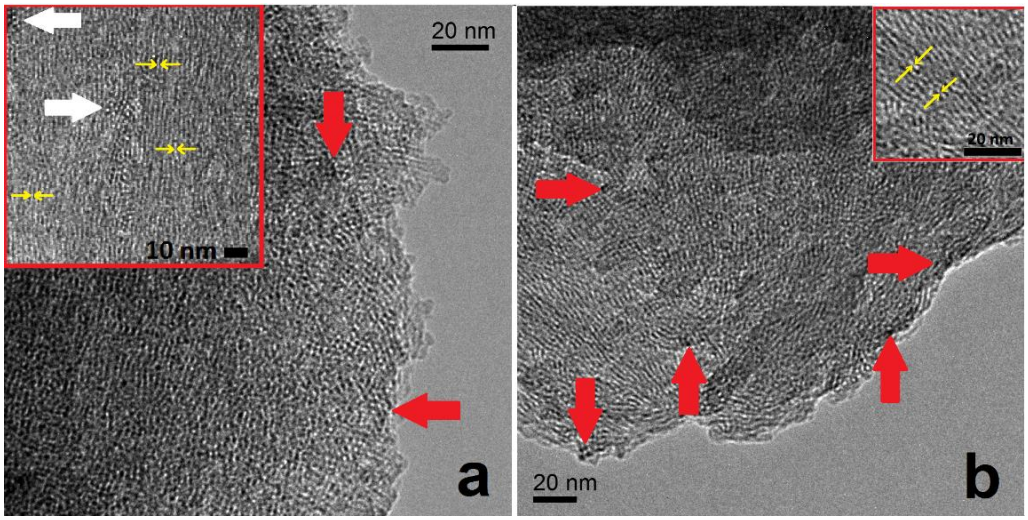

Figure 4-2: HRTEM images of collapsed (MeIMO-c) with carbon residual content indicated with red arrows (a), forming a lamellar phase along with patches of layers and pores coming from pristine NTs indicated with white arrows (*inset* to section a). HRTEM image of Fe-1.4-MeIMO-IE-c with iron-containing clusters indicated with red arrows (b), forming a layered structure with some residual voids *(inset to section b)*

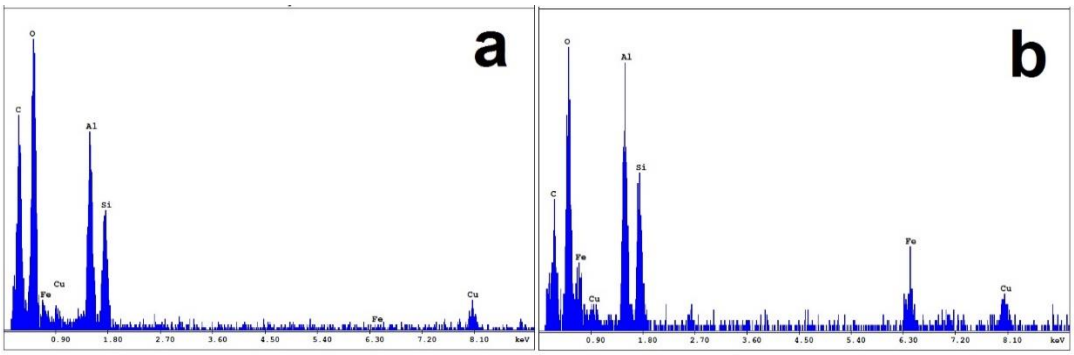

Figure 4-3: EDXS analysis of MeIMO-c (a) and Fe-1.4-MeIMO-c (b). EDXS analysis energy resolution 139.2 eV at Mn Kα

4.2.3 Solid state NMR analysis on the collapsed samples

In order to study the collapse mechanism of MeIMO and Fe-doped MeIMO NTs at the earlier stage of collapsing by considering the effect of thermal treatment environment on the collapse mechanism, all samples were thermally treated at 400 °C with heating rate of 5 °C.min^{-1} for 2h either in air or in vacuum. The solid state ^{13}C, ^{27}Al and ^{29}Si MAS-NMR studies have been performed on all samples.

Clearly, increasing temperature or heating time may result in more structural collapse. For proofing this fact, a longer heating time was considered for one of the samples (Fe-0.7-MeIMO-DS; thermal treatment in air for 2 and 4 hour) and corresponding NMR spectra (^{13}C, ^{27}Al and ^{29}Si) were reported for comparison.

4.2.3.1 ^{13}C MAS-NMR

Figure 4-4 shows the ^{13}C Solid NMR of all the studied samples. All samples, with the exception of MeIMO-air-2h, display a main peak at -1.6 ppm that is very close to the ^{13}C chemical shift of Me_4Si compound (δ= 0 ppm). However, comparing to ^{13}C NMR in tubular structure, the peak is broader and slightly shifted to more negative chemical shift, representing ^{13}C species in slightly different environments, mainly in form of Si-CH_3 and Si-CH_2 groups (Figure 4-5). With MeIMO-air-2h, the mentioned peak is not detectable likely due to burning of methyl groups to CO_2 in the presence of air. However, the small peak at around 30 ppm is assigned to aliphatic carbon species in the structure (Figure 4-5) [181]. Apparently, the thermal treatment in vacuum or the presence of iron in the structure affect the collapsing mechanism in a way that high amount of carbon bonded to Si atoms are still present in the final phase.

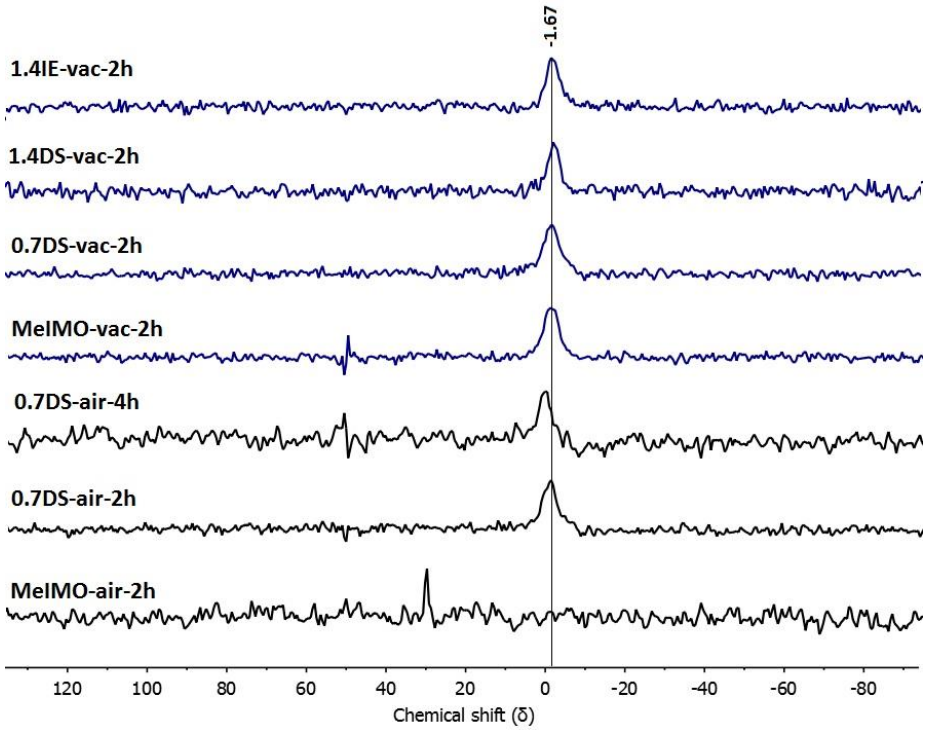

Figure 4-4: Solid-state ^{13}C-MAS NMR of MeIMO and iron doped MeIMO, heated at 400 °C, for 2 h or 4 h with heating rate of 5 °C.min^{-1}, either in air or in vacuum (xDS/IE, represent the Fe-x-MeIMO-DS/IE; x=0.7 and 1.4 wt% of Fe)

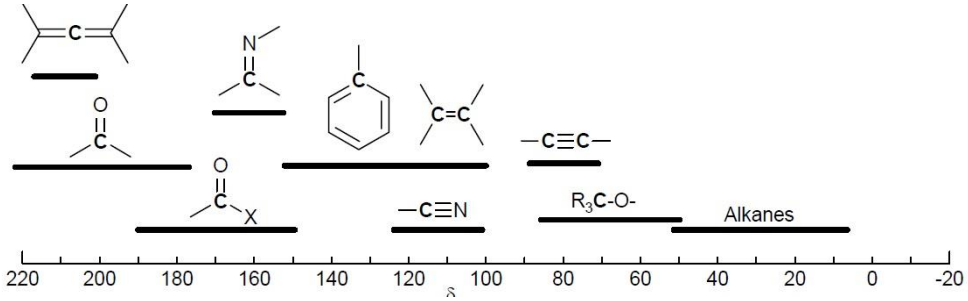

Figure 4-5: The ^{13}C chemical shift scale in solid state NMR

4.2.3.2 ^{27}Al MAS-NMR

Figure 4-6 reports ^{27}Al NMR spectra: with all the samples, three peaks at 4, 33, and 62 ppm are seen. As previously discussed, the peak at 4 ppm is assigned to octahedrally coordinated Al, also present in as-synthesized NTs [95]. A broad peak at 33.6 ppm (absent in the as-synthesized samples) is observed in all the thermally treated samples. There are several possible assignments for such peak. Previous studies stated that peaks in the 20-50 ppm range can be assigned to distorted tetrahedral Al [182, 183], distorted octahedral Al [184] or penta-coordinated Al [184-187]. Based on previous research on structural collapse of imogolite type NTs and in the analogy to the structural transformation of gibbsite under calcination, this peak is assigned to the penta-coordinated Al species [50, 62, 188-191], as observed with some transition alumina, mostly γ-alumina with a chemical shift at approximately 26 ppm [192] and also observed in amorphous aluminosilicates at 33 ppm [191, 192].

The peak at 60 ppm is attributed to tetrahedral aluminum Al(IV) [25, 50, 191] and it has been observed, although with lower intensity, in NTs structure and assigned to some structural defects within the NT wall [49].

The ^{27}Al MAS NMR spectra of both imogolite and MeIMO in collapsed form are very similar. This is in agreement with the fact that the outer surface of both type of NTs may collapse in the same way.

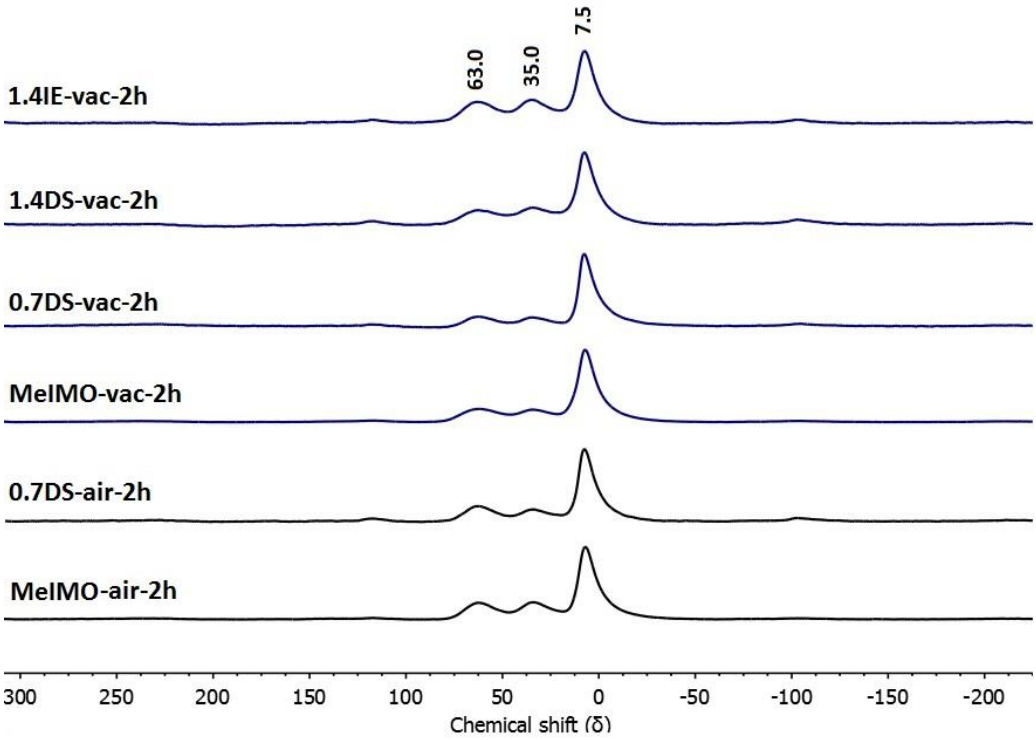

Figure 4-6: Solid-state ^{27}Al -MAS NMR of MeIMO and iron doped MeIMO, heated at 400 °C, for 2 h or 4 h with heating rate of 5 °C.min^{-1}, either in air or in vacuum. (xDS/IE, represent the Fe-x-MeIMO-DS/IE; x=0.7 and 1.4 wt% of Fe)

4.2.3.3 ^{29}Si MAS-NMR

^{29}Si NMR provides a molecular-level understanding of the structural change in the interior wall of the SWNT during heat treatment, (Figure 4-7). The NMR spectra indicate the presence of various environments around Si atom (Scheme 4-4). Accordingly, three different peaks are observed with almost all samples, namely a sharp peak at - 43 ppm, a broad one centered at −90 ppm and a reduced intensity "tail" at −78 ppm. However, the peaks intensities and the chemical shift positions vary from sample to sample, and significantly depend on different heat treatment and on iron loading.

The peak at -43 ppm is assigned to Si atoms bonded to three oxygen atoms and one carbon atom, *i.e.* $O_3{\equiv}Si\text{-}CH_3$ moieties present also in collapsed samples [25]. The broad peak at −90 ppm indicates that most Si atoms are present as Q^4 sites. This peak has been observed at -100 ppm and -90 in imogolite and MeIMO NTs, respectively, and has been assigned to the transformation of the Si coordination environment, due to the thermal collapse of the NTs [25, 50]. Further experiments

on amorphous aluminosilicates showed that ^{29}Si in Q^4 sites display more positive chemical shifts, with increasing the substitution of Al loading as a second neighbor [149, 191, 193-197].

Copéret *et al.* (2015) [191], conducted a comprehensive DFT study on the interface between Silica and Alumina in aluminosilicates. According to their results, the presence of various environments around similar ^{29}Si species, such as different Si−O−Al and Si−O−Si angles and bond lengths, different coordination numbers of Al atoms, presence of non-covalently bonded Al atoms in the neighborhood of Si−O bonds resulted in the chemical shifts distribution within a range of -80 to -97 ppm. The analysis of crystalline and amorphous aluminosilicates with corresponding empirical assignments [149, 191, 194, 196, 197] shows that both H and Al as a second neighbors are the source of increasing in the chemical shift of ^{29}Si MAS-NMR. Consequently, the small tail at −78 ppm chemical shift could correspond to a higher number of Al neighbors (n = 4) together with a proton [149, 191, 194, 197]. The negative shift toward the peaks centered at -83 ppm are due to the bonding of silicate directly to the Al surface, with increasing in Si content in less Al neighbors [191].

On the other hand, in the presence of high Si content in the surrounding environment, ^{29}Si is found at more negative values, especially around −93 ppm (and to a lower extent, −100 ppm), consistent with the existence of more numerous Si as second neighbors and formation of a SiO_2 multilayer and a pure silica network [191].

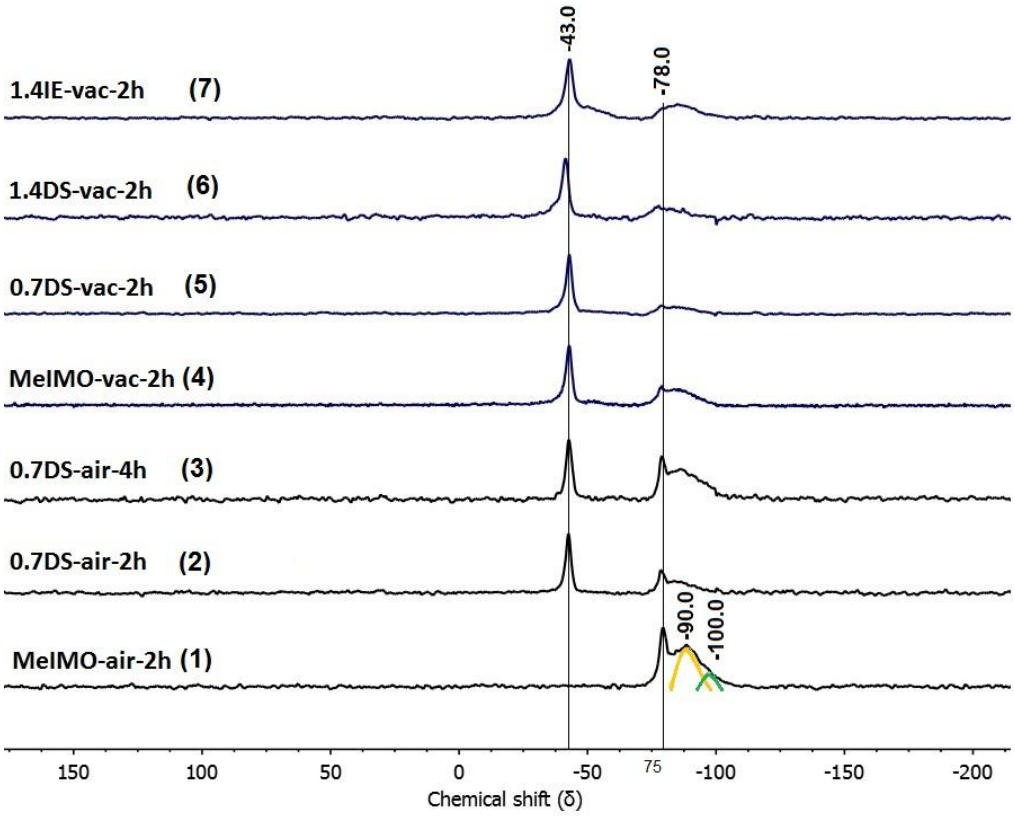

Figure 4-7: Solid-state ^{29}Si -MAS NMR of MeIMO and iron doped MeIMO, heated at 400 °C, for 2 h or 4 h with heating rate of 5 °C.min^{-1}, either in air or in vacuum. (xDS/IE, represent the Fe-x-MeIMO-DS/IE; x=0.7 and 1.4 wt% of Fe)

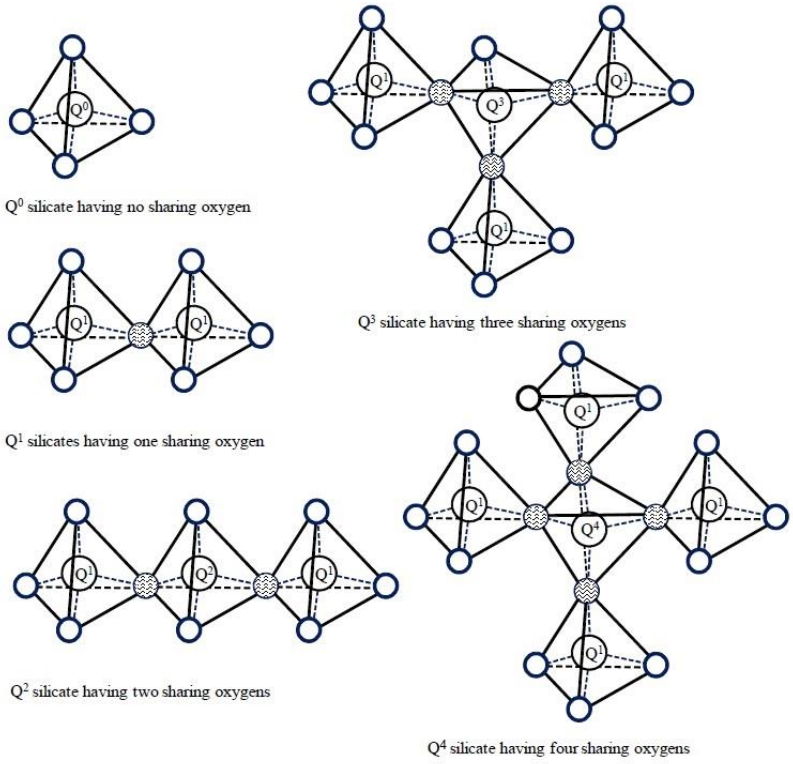

Scheme 4-4: Silicate connections detected from the analysis of ^{29}Si magic angle spinning nuclear magnetic resonance (MAS NMR) spectra [198]

4.2.3.4 The effect of thermal treatment environment and the presence of iron in collapse of nanotube

Comparison between MeIMO treated in air or vacuum (curves 1 and 4) shows that thermal treatment in air results in the disappearance of the ^{29}Si -43 ppm peak and preferential formation of the peak at -90 ppm with a tail at -78 ppm both with high intensity. The broad peak centered at -90 ppm can be ascribed to the formation of a Si-reach phase (Si-O-Si) in air. Furthermore, the tail at -78 ppm is likely due to substitution of a higher number of aluminum neighbors (n=4) into tetrahedral sites around tetrahedral Si atoms, hence, formation of Si−O−Al(IV) groups.

On the other hand, for both bare and Fe-doped samples (curves 4, 5 and 6) by thermal treatment in vacuum a high amount of Si-CH_3 moieties is still present (peak at -43 ppm) and a positive displacement of ^{29}Si chemical shift to the peak centered at -83 ppm, with a small shoulder at -78 ppm.

Following the two mechanisms proposed by MacKenzie for collapsing of imogolite NTs [143], it seems that thermal treatment in air provides occurrence of both mechanisms (mechanism A and B; Scheme 4-1). Accordingly, the cleavage occurs along the NTs by dehydroxylaton between silanol and aluminol groups of two adjacent NTs. Therefore, formation of repeating sequence of O−[Si−O−Al]−O (mechanism B, Scheme 4-1b) occurs, as well as condensation of silanols across the NTs diameter, and formation of the repeating sequence: Al−O− [Si−O−Si]−O−Al (mechanism A, Scheme 4-1a). In fact the presence of air acts as a driving force for faster cleavage of NTs, due to effect of air in total (no sign of peak at -43 ppm for MeMO) or partial (less partial intensity of peak at -43 ppm for Fe-doped samples) burning of the inner methyl groups.

On the other hand, the presence of Fe in structure favors the mechanism B (comparing the spectrum 1 and 2), in agreement with the ^{29}Si chemical shift toward more positive values ($-78 < \delta$ (ppm) < -83) and formation of peak centered at -90 ppm with lower intensity with respect to collapsed MeIMO in air.

According to Zanzottera *et al.* [25], there could be two possible routes (Scheme 4-5) for the reaction between an aluminol group and a $SiCH_3$ group according to mechanism B: (i) direct elimination of methane by transferring the H atom from the aluminol species to $SiCH_3$ (equation 4-1); (ii) and transferring the H atom of methyl group to the aluminol species, followed by releasing of molecular hydrogen (equations 4-2). The Si-CH_2-O-Al species form in the second route are unstable and may release CH_2 groups which are reactive and can either dimerize or decompose to coke-like carbon and molecular hydrogen (H_2) (equations 4-3, 4-4 and 4-5) [25]. In fact, the presence of coke-like carbon is much more evident even by visual inspection of samples thermally treated in high vacuum (10^{-4} mbar), as shown by the dark grey color of the sample (Figure 4-8).

To summarize, thermal treatment in air, results in the occurrence of both mechanisms, in which mechanism B takes place mostly according to equation 4-1. On the other hand, the presence of Fe in the structure and the thermal treatment in vacuum favor mechanism B, mostly through the second route (equations 4-2 to 4-5).

$$\mathrm{Si-CH_3 + OH-Al \rightarrow Si-O-Al + CH_4} \quad (4-1)$$

$$Si - CH_3 + OH - Al \rightarrow Si - CH_2 - O - Al + H_2 \quad (4-2)$$

$$\mathrm{Si} - CH_2 - O - Al \rightarrow \mathrm{Si} - O - Al + "CH_2" \quad (4-3)$$

$$"CH_2" \rightarrow H_2 + C \text{ (coke)} \quad (4-4)$$

$$"CH_2" \rightarrow H_2 + C_xH_y \quad (4-5)$$

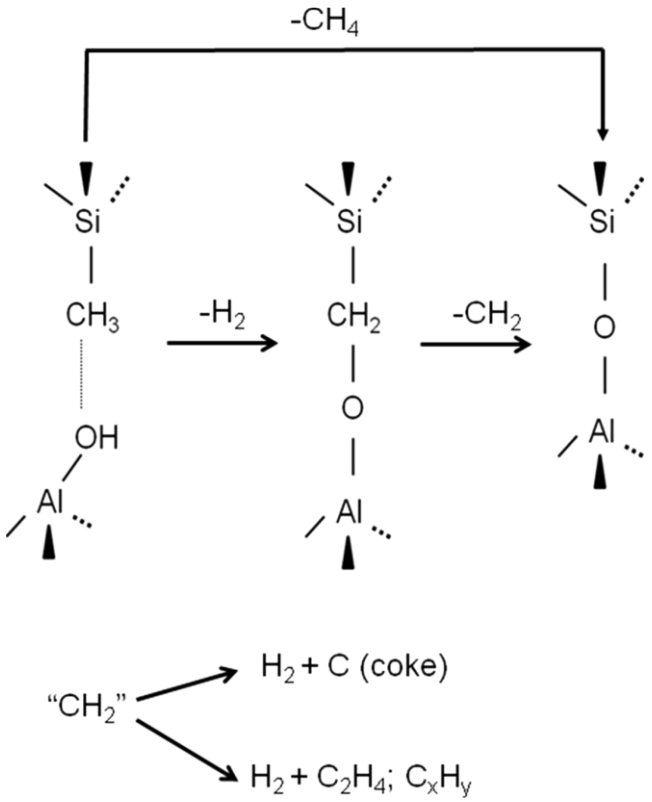

Scheme 4-5: Different proposed route for hybrid imogolite type NTs cleavage [25]

Figure 4-8: The Fe-0.7-MeIMO-DS powder sample, treated in air and vacuum at 500 °C, for 4 h with the heating rate of 5 °C.min^{-1}

4.2.4 Powder X-ray diffraction (XRD)

XRD analysis were done on three selected samples (MeIMO, Fe-0.7-MeMO-IE and Fe-0.7-MeIMO-DS) in the as-synthesized and collapsed form, thermally treated at 500 °C, for 4 h and with the heating rate of 5 °C min^{-1} (Figure 4-9).

With as-synthesized samples (Figure 4-9, left part), the peaks corresponding to an ideal hexagonal packing of NTs are observed as discussed in the previous chapters. After the thermal treatment either in air or in vacuum, the XRD patterns essentially show a single reflection, ascribed to the (100) plane of a lamellar phase. A faint peak due to the (200) diffraction is also barely visible in almost all samples (Figure 4-9, right part).

As shown in Table 4-1 the d_{100} inter-reticular distance in both air and vacuum environments is smaller than the distance between hexagonally packed NTs, causing a shift of d_{100} peak to higher 2θ angles with respect to the parent sample.

According to previous studies, the obtained lamellar structure cannot be viewed as a simple close packing of proper layers [25, 68]. Indeed, based on the mechanism proposed by MacKenzie *et al.* [143] the lamellar phase should result in a thickness of ~0.32 nm (Scheme 4-3b), which is definitely smaller than the inter-reticular distance in the collapsed sample [25]. More likely, the structure of all the collapsed materials is made of patches of layers sealed together, with some micropores entrapped within the layers, deriving by the presence of residual NTs, unaffected by thermal treatment and acting as spacers between the layers (Scheme 4-3b) [25].

Comparing the XRD patterns of samples thermally treated in either air or under vacuum (Figure 4-9, right part), the d_{100} inter-reticular distance is slightly smaller under vacuum, resulting in a shift of d_{100} peak to higher 2θ angles with respect to heat treatment in air (MeIMO: 2θ = 3.98° and 4.20°, Fe-0.7-MeIMO-IE: 3.93° and 4.06° and Fe-0.7-MeIMO-DS: 3.99° and 4.30°, with the values corresponding to the air and vacuum, respectively).

Some molecular dynamic calculations performed on either hydrated or dried imogolite showed that NTs are highly deformable [199, 200] and dried NTs can deform into an oval shape [199] (Scheme 4-6). Besides, defects such as vacancies within the imogolite structure may favor NTs deformation [49].

Moreover, calculations on the frequency values of radial breathing modes of NTs which have been performed by both Guimarães [62] and Konduri [112], suggest that imogolite NTs are rather “soft” and the correspondingly calculated Young’s modulus for both aluminosilicate and aluminogermanate NTs is in the

range of 200–400 GPa [62, 112, 114, 180], which is smaller than Young's modulus for carbon or boron nitride NTs [49].

The XRD results also give an idea about the possible mechanism for collapsing of tubular structure, which agrees with the previous results. Under vacuum, NTs firstly deform around their contact points due to intertube interactions (Scheme 4-6) [199]. This primary deformation may triggers the cleavage of NT more toward the mechanism B and formation of more compact layers with respect to air environment.

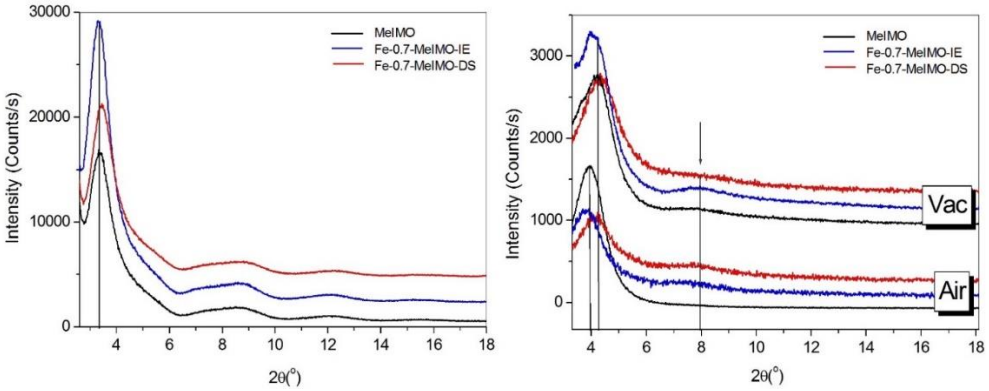

Figure 4-9: (right): Low-angle XRD patterns of as-synthesized MeIMO, Fe-0.7-MeIMO-IE and Fe-0.07-MeIMO-DS. (left): Low-angle XRD patterns of MeIMO, Fe-0.7-MeIMO-IE and Fe-0.07-MeIMO-DS, thermal treated at 500 °C for 4h with heating rate of 5 °C.min^{-1} either in air or in vacuum

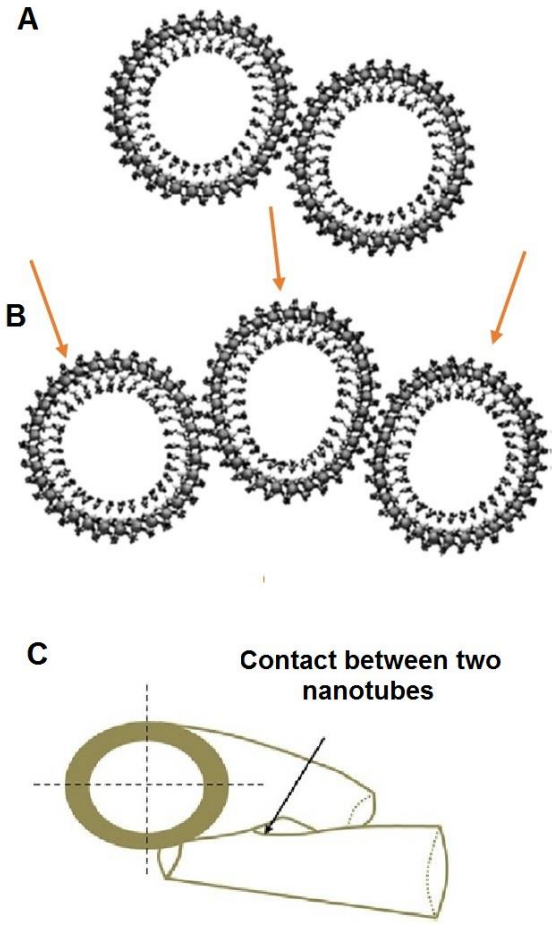

Scheme 4-6: Calculated imogolite structure by molecular dynamics simulations, viewed along the direction of the tube axis: (A) for two interacting NTs and (B) for three interacting NTs [180, 199]. (C) Contact point of two NTs, resulting in their local deformation [199]

Table 4-1: Samples textural properties as derived by XRD patterns

Sample	2θ (°)	d_{100} (nm)	a (nm) [a]
MeMO	3.42	2.58	2.98
MeIMO-500 °C-Air	3.98	2.21	2.55
MeIMO-500 °C -Vac	4.20	2.10	2.42
Fe-0.7-IE	3.40	2.61	3.00
Fe-0.7-IE-500 °C-Air	3.93	2.26	2.61
Fe-0.7-IE-500 °C-Vac	4.06	2.17	2.50
Fe-0.7-DS	3.43	2.57	2.97
Fe-0.7-DS-500 °C-Air	3.99	2.13	2.45
Fe-0.7-DS-500 °C-Vac	4.30	2.06	2.38

(a) Hexagonal cell parameter as obtained by applying the equation $a = {2d_{100}}/{\sqrt{3}}$

4.2.5 Porosity characterization by N_2 adsorption/desorption isotherms

N_2 sorption isotherms at -196 °C were measured on three selected samples (MeIMO, Fe-0.7-MeMO-IE and Fe-0.7-MeIMO-DS) in both the as-synthesized and collapsed forms, thermally treated at 500 °C, for 4 h and with heating rate of 5 °C.min^{-1} (Figure 4-10 (a-c)). The corresponding values of SSA and pores volume are reported in Table 4-2.

All as-synthesized samples (Figure 4-10 (a-c), full symbols) show type IV isotherms with H4 hysteresis loop, typical of microporous systems with some mesoporosity [144]. The ratio between the values of microporous SSA and total SSA (as determined by NL-DFT) shows that doping with iron induces an overall decrease of the microporous area and a corresponding increase in the mesoporous one, in agreement with Shafia *et al.* [23, 24, 85, 156], who showed that Fe-doping mainly affects the outer surface of MeIMO NTs (C mesopores).

All the collapsed samples also show type IV isotherm (Figure 4-10 (a-c): half hollow and hollow symbols, corresponds to heat treatment in air and vacuum respectively). Corresponding values, reported in Table 4-2, show that collapsed

samples have lower BET SSA with respect to parent samples, due to partial pore blocking caused by the structural cleavage accompanied by dehydroxylation [25, 50]. Although the wall structure of collapsed samples is partially damaged or disordered, the microporous volume and corresponding ratio between microporous and total SSA, are indeed higher in both thermal treatment in air and vacuum with respect to parent samples (Table 4-2). In fact, the achievement of a fully layered structure is unlikely at the adopted temperature.

The PSD curves of as-synthesized and collapsed samples are reported in Figure 4-10(d-f): the as-synthesized samples (Figure 4-10 (d-f):full symbols) show similar porosity, in agreement with values reported in Table 4-2, with a slight increase in the volume of large mesopores in the presence of Fe [23, 24, 156]. On the other hand, the PSD curves of collapsed samples (Figure 4-10 (d-f)) show at least two families of micropores (~1.0 nm and 1.0-2.0 nm), and a dramatic decrease of mesopores volume with respect to parent samples. The total pore volume for the samples treated in vacuum is lower than samples treated in air and even lower than that of parent samples. Conversely, the ratio between micropore and total SSA are considerably high. These data can indicate that in the presence of vacuum the layers are more compact, in agreement with the results obtained by XRD analysis. Furthermore, the decomposition of methyl groups in the presence of vacuum results in formation of coke-like phase [25], as mentioned previously (Figure 4-8). The presence of residual C-containing fragments in the structure may partially block the pores and results in lower micropores volumes with respect to the air treated samples.

Table 4-2: Samples textural properties as derived by N_2 sorption isotherms at -196 °C

Sample	BET SSA (m^2g^{-1})	NL-DFT (SSA) (m^2g^{-1})	Micropore SSA/Total SSA (%) [a]	Micropore volume (cm^3g^{-1}) [b]	Total pore volume (cm^3g^{-1})
MeIMO	557	476	55%	0.12	0.29
MeIMO-500 °C -Air-4h	617	514	71%	0.12	0.27
MeIMO-500 °C -Vac-4h	200	228	64%	0.04	0.17
Fe-0.7-IE	617	525	53%	0.11	0.33
Fe-0.7-IE-500 °C-Air-4h	486	562	76%	0.13	0.29
Fe-0.7-IE-500 °C-Vac-4h	542	570	78%	0.15	0.27
Fe-0.7-DS	576	497	54%	0.11	0.32
Fe-0.7-DS-500 °C -Air-4h	467	548	56%	0.075	0.35
Fe-0.7-DS-500 °C -Vac-4h	300	352	81%	0.09	0.19

(a) Percentage ratio [(Microporous SSA)/(Total SSA)] as calculated from NL-DFT cumulative surface area curves
(b) As calculated by applying the *t*-plot method

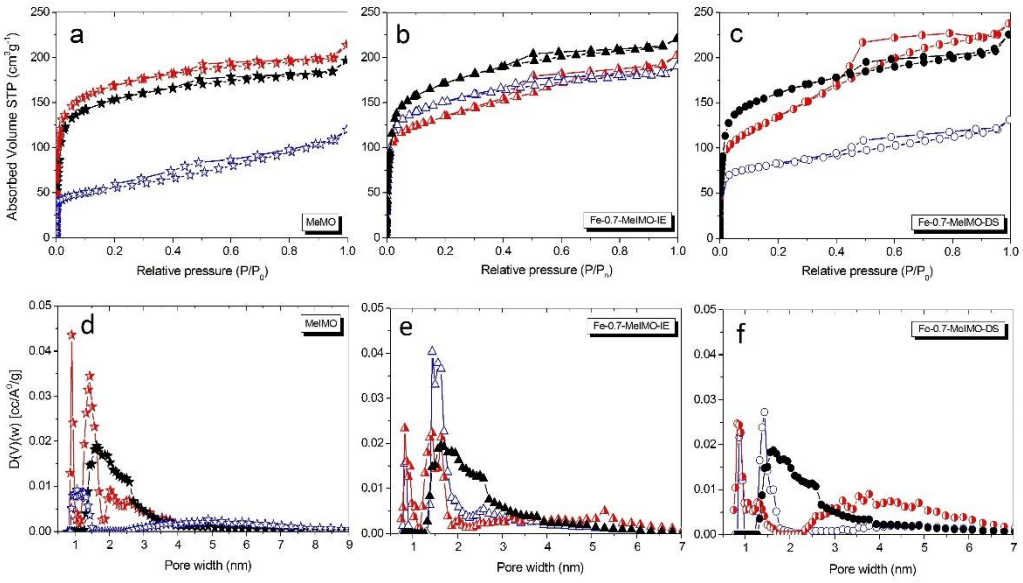

Figure 4-10: (a-c) N_2 isotherms of samples at -196 °C for as-synthesized samples (full symbols) and thermal treated samples at 500 °C for 4h with heating rate of 5 °C.min^{-1}, either in air (half hollow symbols) or in vacuum (hollow symbols). (d-f) corresponding PSDs, as obtained by applying the NL-DFT method, of as-synthesized samples (full symbols) and thermal treated samples at 500 °C for 4h with heating rate of 5 °C.min^{-1}, either in air (half hollow symbols) or in vacuum (hollow symbols)

4.2.6 Nature of iron species as studied by UV-Vis spectroscopy

DR UV-Vis spectra of collapsed samples (heated in air at 500 °C for 4 h with the heating rate of 5 °C.min^{-1}) are reported in Figure 4-11a. The spectrum of all collapsed samples is mainly dominated with two characteristic oxygen-to-metal charge-transfer (CT) bands below 300 nm, assigned to CT transitions from O^{2-} to Fe^{3+} ions in tetrahedral (Td, 240 nm) and octahedral (Oh, 290 nm) coordination [157].

In the case of Fe-1.4-MeIMO-IE-c, a broadening of UV-vis spectrum is observed in the range of 300-600 nm with a maximum around 500 nm. The broadening of UV spectrum in the 300-400 nm range is assigned to CT transitions of oligomeric Fe oxo-hydroxide clusters, whereas bands above 400 nm to larger Fe oxo-hydroxide particles and *d-d* transitions [157, 159, 201].

After collapsing (Figure 4-11b), UV bands ascribed to Fe oxo-hydroxide clusters in the range of 300-400 nm almost disappear, whereas the bands below 300 nm (211 and 270 nm) increase in intensity. The position of 270 nm band is typical of CT transitions, indicating a change in the environment of Fe^{3+} ions, by changing

in the environment of Si and Al atoms. During thermal treatment at 500 °C, Fe oxo-hydroxide clusters likely reacted with the aluminum-silicate network, as observed for Fe in LFO perovskite [202]. Such phenomenon is expected to impact on the catalytic activity of collapsed samples, which will discuss in chapter 6.

In addition in the Fe-1.4-MeIMO-IE-c sample, CT at 370 nm shifted slightly to higher wavelengths, which may indicate the migration of part of the Fe^{3+} ions from framework to extra framework positions and aggregation into Fe oxo-hydroxide clusters present Fe-1.4-MeIMO-IE sample [203].

Band gap energy (E_g) values of all collapsed samples were calculated according to Tauc's formula and the corresponding curves are reported in Figure 4-11c. In Fe-doped samples, the calculated band gap is different with respect to as-synthesized samples, indicating a change in the environment of Fe in agreement with previous observations (Table 4-3).

However, in the case of MeIMO, the band gap of collapsed sample is lower than the as-synthesized sample. This agrees with the theoretical calculation based on Self-Consistent Charge Density Functional Tight Binding (SCC-DFTB) calculations, on the effect of dehydroxylation on the band gap energy of imogolite NTs which has been performed recently by da Silvia *et al.* [26]. According to their studies, upon dehydroxylation up to 50 %, NTs tend to deform and changing in the environment of silanols and formation of Si-O-Si bonds result in the decreasing of band gap energy. Therefore, the dehydroxylated imogolite is considered as a semiconductor.

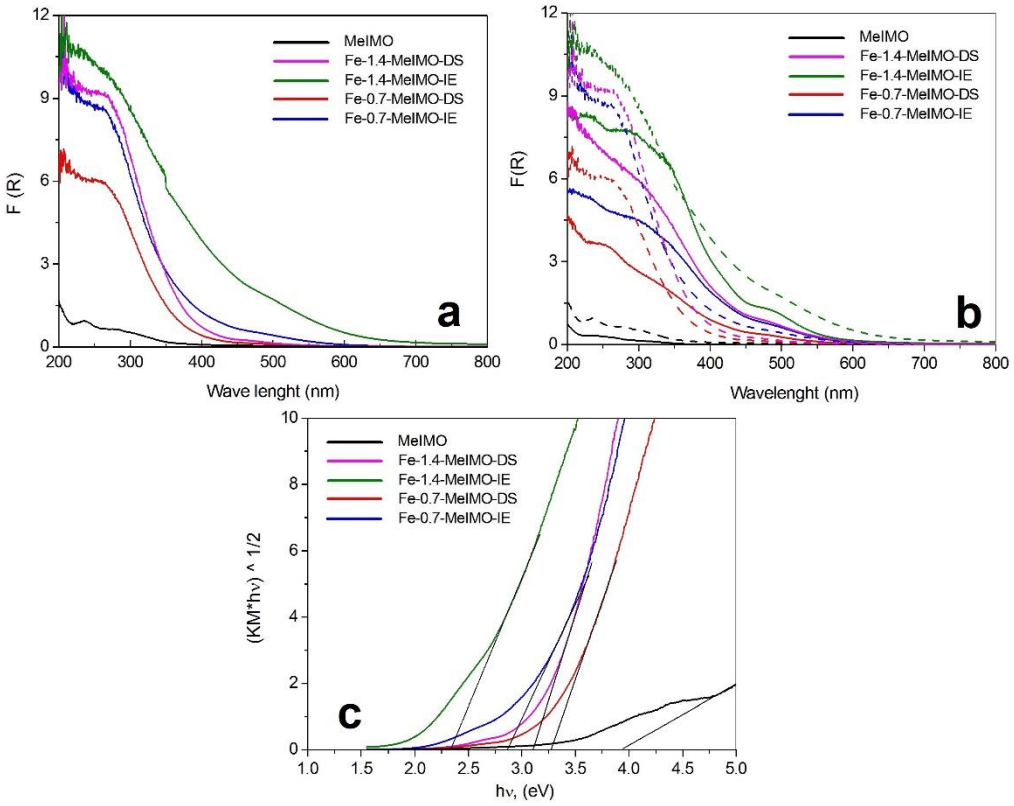

Figure 4-11: DR UV-Vis spectra of collapsed samples obtained at 500 °C for 4h with heating rate of 5 °C.min^{-1} in the air atmosphere (a) and comparison between DR UV-Vis spectra of as-synthesis samples (solid line) and corresponding collapsed samples (dashed line) (b). Corresponding Tauc plots of collapsed samples (c)

Table 4-3: Calculated band gap energy according to Tauc's formula for both NTs and collapsed samples

Sample	Band Gap in NT form (eV)	Band Gap in collapsed form (eV)
MeIMO	4.7	3.9
Fe-0.7-MeIMO-IE	2.4	2.8
Fe-0.7-MeIMO-DS	2.7	3.2
Fe-1.4-MeIMO-IE	2.4	2.3
Fe-1.4-MeIMO-DS	2.6	3.1

4.3 Conclusion

Thermal treatment of imogolite type NTs reveals the progressive dehydroxylation in the NT structure resulting in the formation of new phase where a lamellar structure coexist with some residual voids derived from pristine NTs. Moreover, thermal treatment in air or vacuum may affect the collapse mechanism and the structure of the final phase. Accordingly, the thermal treatment in air leads to faster cleavage of NTs by the elimination of methyl group from structure and collapse of NTs through both mechanisms (mechanisms A and B) postulated by MacKenzie *et al.* [143]. On the other hand, under vacuum, the burning of methyl groups is hindered. The presence of Fe in the structures, same as vacuum treatment triggers the mechanism B, probably due to joining tendency of Fe^{3+} ions in the NTs framework to the extra framework Fe-containing clusters.

The collapsed samples also exhibit a different light adsorption capacity and different band gap values with respect to the as-synthesized ones, probably due to the changing in the environment of atoms in the collapsed phase. However, more complete studies on collapsed samples are needed to investigate their formation mechanisms and their modifications. Control of thermal stability of imogolite type NT and the different structural phases arrived from thermal treatment is a prerequisite for the elaboration of future materials and their applications.

Chapter 5

Surface Acidity and Reactivity of Bare and Fe-Modified Methyl-Imogolite Nanotubes with azo-dye

5.1 Introduction

The composition of the inner and outer surfaces of imogolite type NTs with the unique porous structure occurring in the dehydrated NTs (Scheme 5-1) introduces this material as an interesting choice for different chemical engineering applications. The major applications of this material relate to its surface where the presence of cavities with various pore dimensions with different chemical properties and large specific surface areas (SSA) are required. For example one might utilize this material for catalysis application, gas adsorption and storage [9, 10, 116], removal of ions from aqueous solution [23, 85], etc. The outer and inner surface of imogolite NTs, with the presence of silanol and aluminol amphoteric groups, have different acid/base properties and ion exchange capacity [8]. Further advances in this field are significant for improvement of materials with different functionality based on imogolite and imogolite-like constituents. In this chapter the surface acidity and catalytic reactivity of MeIMO NTs and Fe-doped MeIMO NTs have been studied for the first time, in order to gain a deeper insight for further applications.

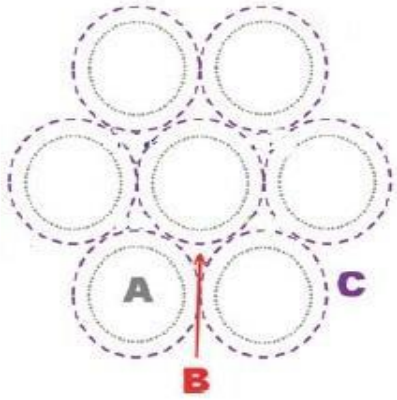

Scheme 5-1: representation of different kind of surfaces present in the bundles of dehydrated imogolite type NTs [8]

5.2 Determination of acid–base properties by adsorption of pyridine followed by IR spectroscopy

In order to study the adsorption properties of imogolite type NTs, the proper heat treatment is needed at elevated temperatures under vacuum in order to remove the water molecules [8, 107, 115]. However, the outgassing temperature must remain below 300 °C to avoid the structural collapse as mentioned in chapter 4. Therefore, the optimal pretreatment temperature for maximum pore accessibility still maintaining the nanotubular structure, is in the range of 270°C–300°C [25, 115].

To investigate further the catalytic potential of imogolite type NTs, the adsorption of different reactive molecules can be studied for probing the acidic and basic sites in the structure of material, particularly the type and abundance of acidic Lewis and Brønsted species. Bonelli *et al.* [8, 9, 107, 115], carried out several studies on the surface acidity of imogolite-type NTs, using IR spectroscopy of various probes including NH_3, CO and CO_2. The results imply the interaction of NH_3 molecules as well as, CO molecules with silanol groups and confirms the significant acidic sites associated with these groups in the inner surface of imogolite NTs. However, in a case of MeIMO NTs non-polarity and hydrophobicity of Si-CH_3 groups may hinder the interaction of probe molecules with the inner surface [8, 9, 115, 138]. On the other hand, the outer surface of both imogolite and MeIMO NTs, show weak Lewis acidity, as shown by the coordination of NH_3 molecules on external Al^{3+} Lewis sites.

One of the most common probe molecules for identification of acidic sites, especially in aluminosilicates and silica-alumina is pyridine [204]. Unlike ammonia which interacts with both weak and strong acidic cites, differently-bonded pyridine gives different absorption bands in the IR range which are quite evident and give information about different Lewis (LPy) acidic sites, Brønsted (BPy) acid sites and the hydrogen-bonded pyridine (HPy) molecules on the surface of materials [205-208].

5.2.1 Sample preparation for IR analysis and pyridine adsorption method

The samples for pyridine adsorption analysis are preheated at 200 °C or 500 °C for 4 h in high vacuum line and maintained in glovebox for further experiments. The pellets for IR measurements are obtained in the form of thin, KBr-supporting wafers (10% of the sample concentration in KBr; all procedure is performed in glovebox). The extra pure dry pyridine is attached on IR cell including the sample pellet, which was pre-evacuated in the line. The IR spectra of outgassed samples are studied both before and after pyridine adsorption at r.t., followed by consecutive evacuation at r.t., 80 °C, 150 °C (and for some samples even up to 250 °C). All spectra are subtracted from spectrum of sample before pyridine adsorption. All Spectra are recorded using a Bruker FT-IR Alpha spectrometer, equipped with OPUS software. Spectra are recorded at resolution <2 cm^{-1}, A typical experiment consisted of the measurement of transmission in 32 scans in the region from 4000 to 1000 cm^{-1}.

5.2.1.1 Identification of both Brønsted and Lewis Acid Sites as obtained by IR spectra of adsorbed pyridine

Inspection of IR spectra show that several bands in the 1650-1430-cm^{-1} region appear due to pyridine adsorption. This indeed corresponds to ν(C-C) stretching vibrations of the ring (Table 1) [209, 210]. The relative intensity ratio of the IR band at 1545 cm^{-1} (characteristic of the pyridium ions PyH^{+}) to the band at 1455 cm^{-1} (characteristic of the LPy species), are considered as an index of relative concentration of the Brønsted to Lewis acid site [204, 212].

Lewis sites (LPy): Tri-coordinated aluminum atoms are strong Lewis acid centers [212]. The LPy species produced the characteristic bands in the range of 1630–1600 cm^{-1} [210]. However, the most typical Lewis acid sites are the bands

near 1455, 1490 cm^{-1}, and the 1455 cm^{-1} band is typical sign of these sites [212]. Lewis acid sites have high stability to outgassing at high temperatures [210].

Brønsted sites (BPy): The protonation of pyridine molecules to pyridinium ion (PyH^+) is the main reason of the formation of BPy sites. BPy shows adsorption bands at 1640–1630 cm^{-1} and 1550–1530 cm^{-1} regions and bands near 2450 and 1580 cm^{-1} [210]. However, the most common bands are at about 1490, 1540, and 1635 cm^{-1}. The band at 1540 cm^{-1} is also considered a typical band of this site [211, 212]. BPy species are relatively less thermally stable than LPy species [210].

Hydrogen-bonded pyridine (HPy): these sites are formed due to H-bond donor sites (surface-OH groups) [210] and also the strong electrostatic interaction between the cation and the pyridine molecule [212, 213]. They are characterized by strong IR bands in the range of 1596–1590 and 1455–1445 cm^{-1} [210]. Furthermore, another characterization of HPy is the low frequency shifts of νOH vibrations of the associated surface-OH groups [210]. According to studies, HPy sites on the clay solid, has vibration bands near 1440 and 1590 cm^{-1} [211, 212]. These species are likely unstable to outgassing at even low temperatures with most of metal oxides (100 °C) [210].

Physisorbed-bonded pyridine (PPy): it is due to loosely adsorbed closed packed layers (liquid-like) of Py molecules give bands in the range of 1450 –1430 cm^{-1}[210]. These bands are normally removed after evacuation at temperature near 150 °C or even room temperature [214].

The summary of different configurations with corresponding IR characteristic bands of adsorbed pyridine on the surface of metal oxides at r.t., is reported in Table 5-1 [210]. Scheme 5-2, also addresses an overview of different IR characterization bands of pyridine adsorbed on the surface of acid solid [211, 212].

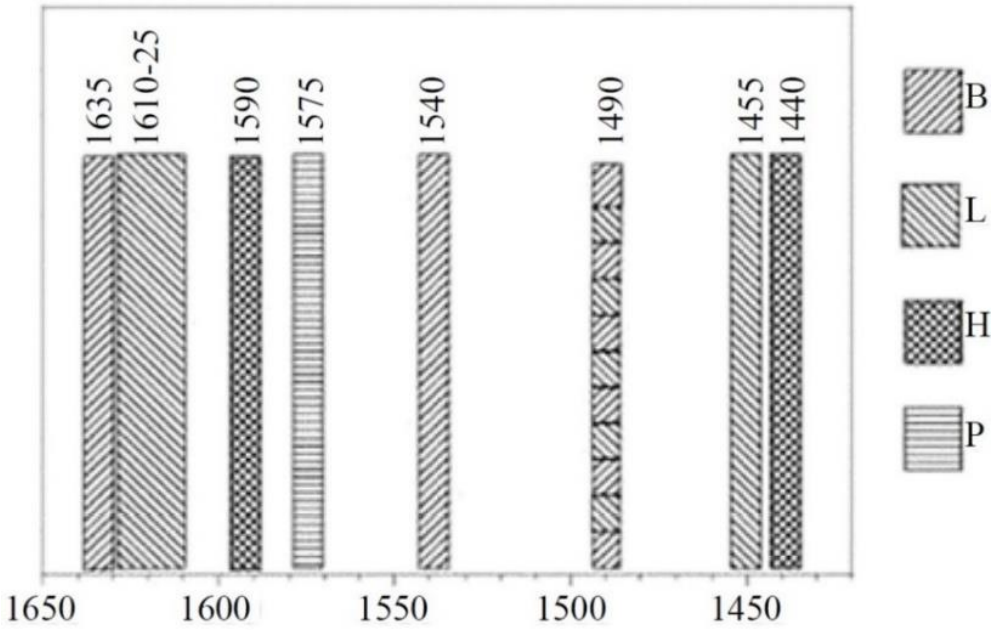

Scheme 5-2: IR characterization bands of pyridine adsorbed on the surface of acid solid Pyridine adsorbed on B, Brønsted sites; L, Lewis sites; H, hydrogen- bonded, and P, physisorbed pyridine [211, 212]

Table 5-1: Shape and IR characteristics bands of adsorbed pyridine on the surface of metal oxides at $\geq 27^{\circ} C$ [210]

Py Species	T /K	Configuration	νCCN/cm^{-1} ν_{8a}	ν_{19b}
PPy	300	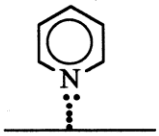	1585	1445 & 1435
HPy	300	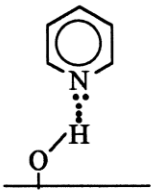	1600-1580	1447-1440
BPy	300	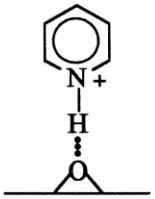	1640-1630	1540-1500
LPy	300	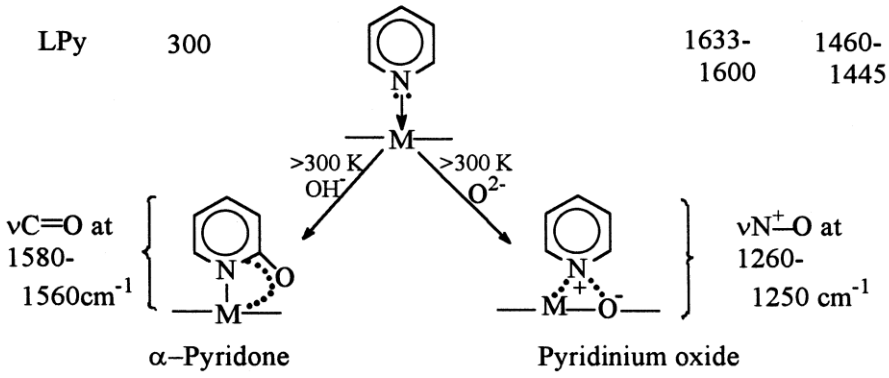	1633-1600	1460-1445

5.2.1.1.1 IR spectra of pyridine adsorbed on the surface of MeIMO and Fe-doped MeIMO

The IR spectra of bare and Fe-doped MeIMO samples after dehydration at 200 °C and 500 °C, are reported in Figure 5-1a and 5-1b respectively. For samples dehydrated at 200 °C, the broad adsorption range (3800-3000 cm^{-1}) is observed due to hydroxyl groups on the outer surface of NTs [8]. For all Fe-doped samples, no

significant difference has been observed, due to low iron content, which results in the similarity in the IR spectra. Lamellar structure is formed for all samples after pre-heating at 500 °C [25] (Figure 5-1b), as discussed in forth chapter and based on results obtained by XRD, MAS NMR, TEM and BET surface area analysis. According to the spectra, the bands related to the C-H stretching and bending are still observable with remarkable high relative intensity and seems unperturbed due to their unchanged position with respect to pristine NTs [25] (2970 and 2916 cm^{-1}, assigned to asymmetric and symmetric stretching of inner CH_3 groups, respectively). These observations are in agreement with the results found in chapter four and strongly suggest that for MeIMO NTs collapsing mainly affects the outer surface, and inner surface mostly remained unchanged [25]. In the OH stretching region, the intensity of OH vibration is decreased mainly due to the dehydroxylation of the outer surface.

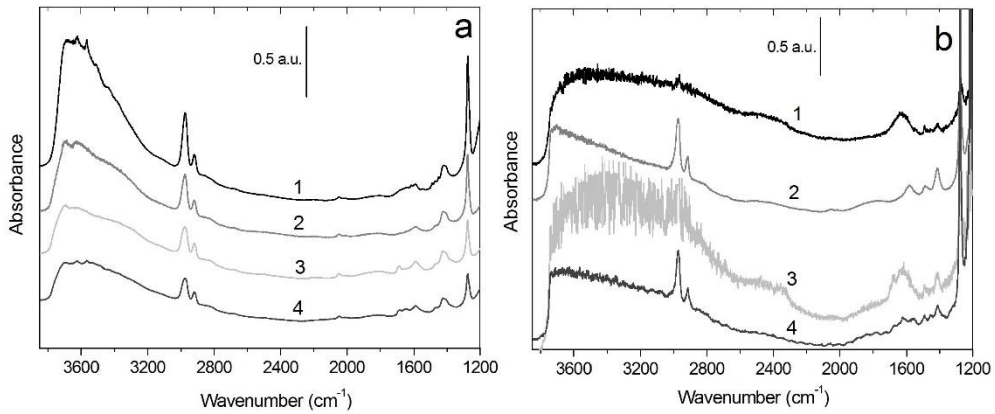

Figure 5-1: Comparison of FT-IR spectra of a MeIMO (curve 1), Fe-0.7-MeIMO-IE (curve 2), Fe-0.7-MeIMO-DS (curve 3) and Fe-1.4-MeIMO-DS (curve 4) KBr wafer samples, outgassed at 200 °C (section a) and 500 °C (section b).

5.2.1.1.2. IR spectra of pyridine adsorption in the 1700-1400 cm^{-1} range

Figure 5-2 (a-d) reports different IR spectra of pre-heated samples at 200 °C in the adsorption region of 1700-1400 cm^{-1} after pyridine adsorption at r.t.,(only displays for Fe-0.7-MeIMO-IE and Fe-1.4-MIMO-DS for comparison) followed by evacuation in r.t., 80 °C and 150 °C for all samples and even at 250 °C (for MeIMO).

According to the spectra, the samples display adsorption bands at 1440, 1450, 1488, 1545, 1590 and 1610-1622 and 1635 cm^{-1}. The bands at 1450 and 1610-1622

cm^{-1}, correspond to Lewis acid sites, with notably high intensity in MeIMO with respect to other Fe-doped samples. The intensity of these band is decreases after evacuation at high temperature. The relative intensity of Lewis bands at 150 °C for all Fe-doped samples are low; however, for MeIMO, these bands are even detectable in evacuating at 250 °C, which confirms the stronger acidity of the outer surface of MeIMO due to coordination of pyridine molecules on the Al^{3+} Lewis sites, with respect to Fe-doped samples [23, 107, 115].

Both Lewis and Brønsted acidic sites are characterized by IR band at 1490 cm^{-1}, which is evident in MeIMO sample at higher relative intensity with respect to Fe-doped samples. Brønsted acidic sites are characterized by absorption bands at 1545 and 1636 cm^{-1}, which are the typical bands for pyridinium cations, formed by protonation of pyridine by Brønsted acidic surface OH groups [205, 207]. These bands are detectable in MeIMO samples, even after evacuation at 150 °C. For Fe-doped samples (Figure 5-2 b-d), these bands are not observable, or observable with low intensity (*e.g.* in Fe-1.4-MeIMO-DS) due to less acidic properties of Fe-(OH)-Al groups [23].

Pyridine molecules adsorbed by hydrogen bonding, are characterized by bands at 1442 and 1590 cm^{-1}. These bands are not detectable in IR spectra of MeIMO samples; however, they are present in all Fe-doped samples (Figure 5-2 b-d), mainly due to electrostatic interactions between pyridine molecules and weakly acidic OH groups, likely related to Fe_2O_3 clusters [23].

Physisorbed pyridine molecules show bands in the 1430-1440 cm^{-1} and 1580-1595 cm^{-1} range. In almost all samples they disappeared after evacuation at r.t.

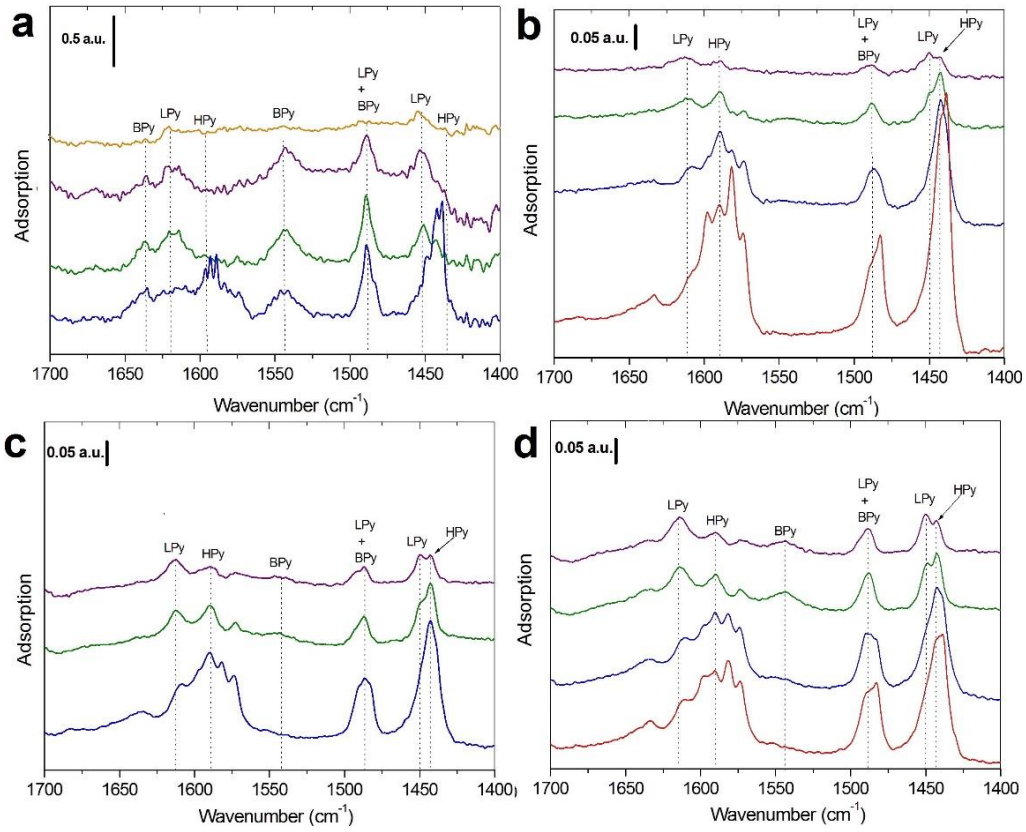

Figure 5-2: Difference IR spectra obtained on samples preheated at 200 °C, after adsorption of pyridine at r.t. (red spectrum), desorption at r.t. (blue spectrum), 80 °C (green spectrum), 150 °C (purple spectrum) and 250 °C (orange spectrum), on MeIMO (a), Fe-0.7-MeIMO-IE (b), Fe-0.7-MeIMO-DS (c) and Fe-1.4-MeIMO-DS (d)

Figure 5-3 (a-d) reports different IR spectra of pre-heated samples at 500 °C and corresponding desorption at r.t., 80 °C and 150 °C and 250 °C. The spectra show that all samples have both Lewis and Brønsted acidic sites, which are stable even after evacuation at 250 °C.

According to the observations in fourth chapter and based on previous studies on the structural collapse of imogolite and MeIMO [25, 183], the presence of penta-coordinated, tetra-coordinated and hexa-coordinated aluminum sites and also residual hydroxyl group, are the main reason for acidic properties of collapsed samples and also bands observed in OH region [215], in fair agreement with what was observed with Bonelli *et al.* [8, 115] on surface acidity of collapsed phase. Furthermore, the increase in the intensity of Brønsted sites with respect to the parent samples may indicate that the collapsed phase has interesting acidic properties.

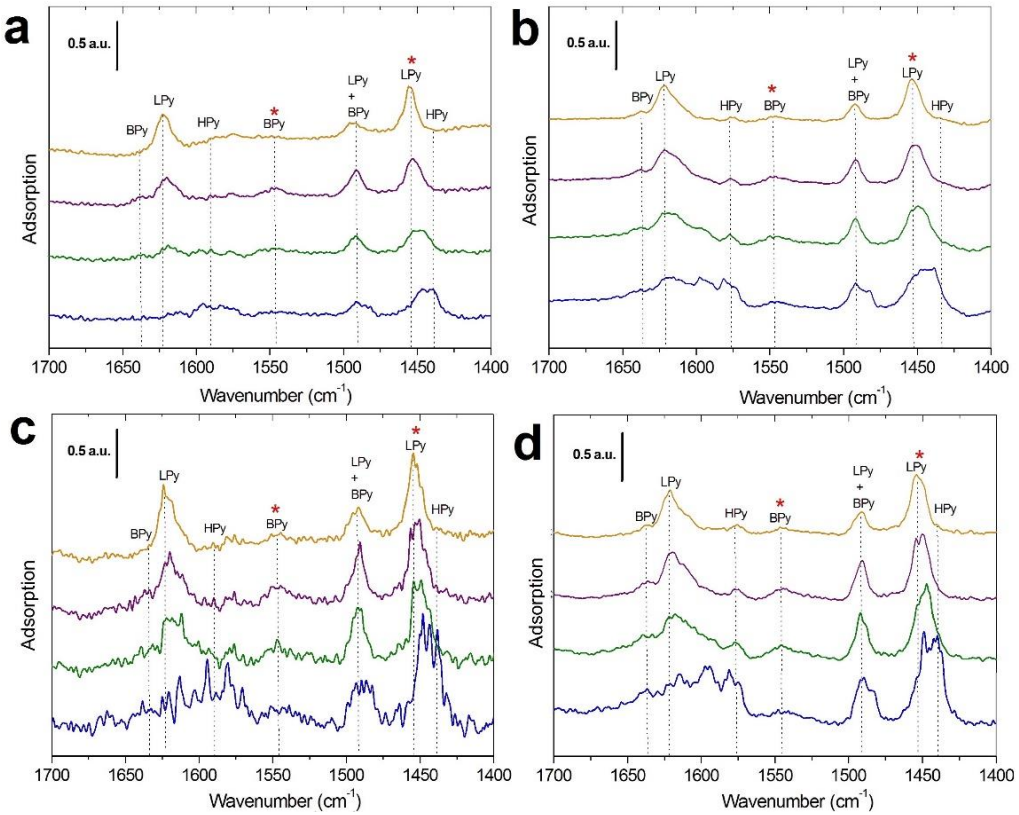

Figure 5-3: Difference IR spectra obtained on samples preheated at 500 °C, after desorption of pyridine at r.t. (blue spectrum), 80 °C (green spectrum), 150 °C (purple spectrum) and 250 °C (orange spectrum), on MeIMO (a), Fe-0.7-MeIMO-IE (b), Fe-0.7-MeIMO-DS (c) and Fe-1.4-MeIMO-DS (d)

5.2.1.1.3. Studying the IR spectra of pyridine adsorption in the OH stretching region

The adsorption spectra of pyridine on Fe-0.7-MeIMO-IE and Fe-0.7-MeIMO-DS (pre heat at 200 C) were selected to study the adsorption in OH stretching regions (3800-300 cm-1) (Figure 5-4 a-b). Negative adsorption bands in the region of 3800-3000 cm^{-1} are assigned to the disappearing of hydroxyls, due to interaction with pyridine [8, 115].

The IR spectra of Fe-0.7-MeIMO-IE, show 3 different bands at 3700, 3623 and 3429 cm^{-1}, while for Fe-0.7-MeIMO -DS only one adsorption band presents at 3770 cm^{-1}.

The adsorption band at 3700 cm^{-1} is assigned to hydroxyl species of Fe_2O_3 clusters: such OH groups should be less acidic, and indeed in Fe-0.7-MeIMO-DS

with less expected amount of Fe_2O_3 clusters, this band is not detectable. The band at 3623 cm^{-1}, corresponds to the inner hydroxyl groups, located in the B surface between 3 NTs (Scheme 5-1). In clay minerals (kaolinite), this band is ascribed to octahedral and tetrahedral sheets of inner hydroxyl groups [212]. Probably in IE method, the presence of more iron-containing clusters within NTs results in higher accessibility of B pores with respect to DS method. The adsorption bands in the 3440-3360 cm^{-1} region, are signed to inter-layer OH species, forming H-bonds to O atoms of another layer [115]

Due to similarity between the IR spectra of pyridine adsorption on samples prepared at 500 °C, the Fe-0.7-MeIMO-IE was selected for studying the adsorption behavior of pyridine molecules. The IR spectra present the adsorption bands at 3742 cm^{-1}. The negative sharp bands in the 3770-3630 cm^{-1} region, are mainly due to the H-bonding interaction between hydroxyl groups of silanols in collapse structure with high acidity, in agreement with the previous studies on surface acidity of collapsed imogolite-type materials with NH_3 interaction [8].

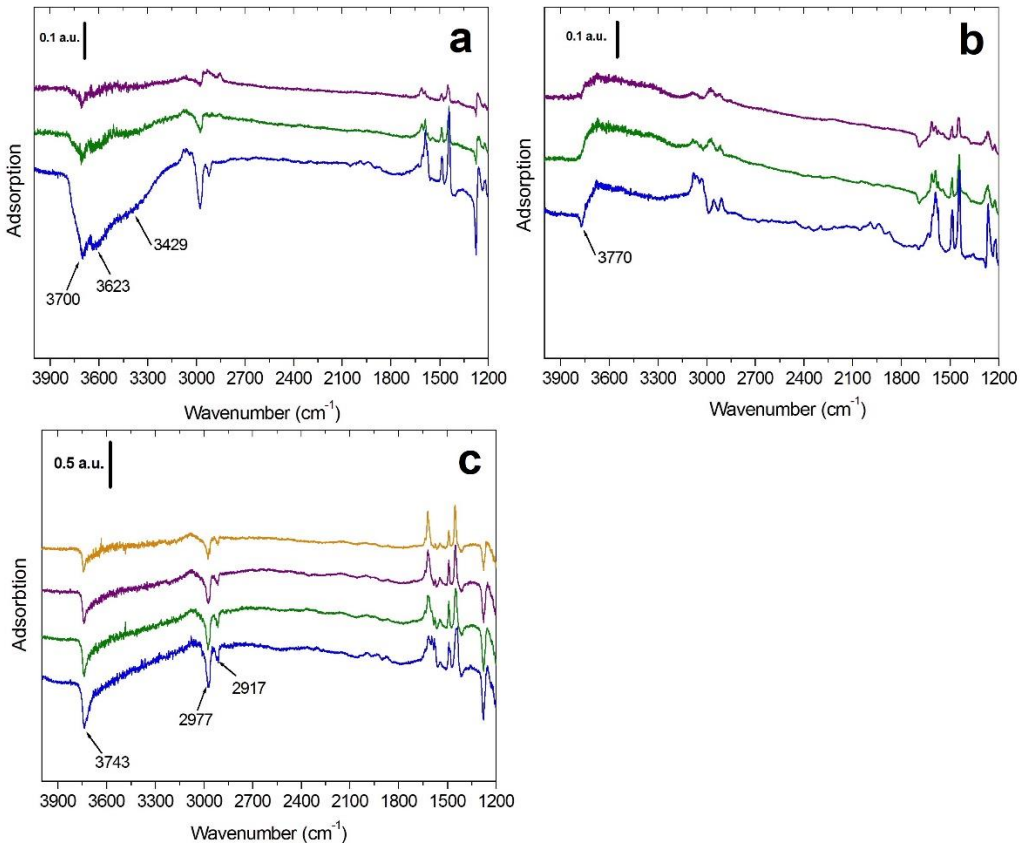

Figure 5-4:IR spectra obtained after desorption of pyridine at r.t., 80 °C, 150 °C and 250 °C on (a) Fe-0.7-MeIMO-IE preheated at 200 °C, (b) Fe-0.7-MeIMO-DS preheated at 200 °C, (c) Fe-0.7-MeIMO-IE preheated at 500 °C

5.3 Interaction with acid orange 7 (NaAO7) dye in the aqueous solution

Dye pollutants are considered a source of environmental contaminants, which damage both aquatic and human life, due to their toxic, carcinogenic and mutagenic effects [216, 217]. Azo dyes are characterized by the presence of one or more azo groups (-N=N-) bounded to aromatic rings. They are considered as the most important class of synthetic organic dyes, which are applied widely in different industries. Due to high chemical stability and versatility of azo dyes, it has been estimated that more than half of all commonly used dyes are from this category.

Synthetic azo dyes are widely used by textile, cosmetic, photographic, pharmaceutical and food industries, representing environmental concerns. The increasing amount of azo dyes increases the water toxicity due to inhibition of

sunlight penetration, which negatively affects the photosynthetic reaction of aquatic flora [218-222]. Therefore, the removal of these pollutants and aromatic compounds from water is considered as one of the most important challenges that scientists and researchers must address [223-225]. However, the synthetic azo-dyes have a high stability and resistance to light and oxidation agents in the aqueous media [226], due to their complex aromatic structure that makes them stable to biodegradation [227]. One of the most common used azo dye is, Acid Orange 7 (NaAO7, chemical formula: $C_{16}H_{11}N_2NaO_4S$), which is soluble in water and is a textile dye mainly used for silk and wool dyeing [228].

In this section the adsorption of NaAO7 dye with the synthesized MeIMO and Fe-doped MeIMO NTs, has been investigated. The same studies have been performed by Shafia *et al.* [23, 85] on the adsorption of NaAO7 dye with imgolite and Fe-doped imogolite NTs. According to their research results, the NaAO7 as a sodium salt, in the presence of water was dissociated and the anion part ($C_{16}H_{11}N_2O_4S^-$) could interact electrostatically with outer $Al(OH_2)^+Al$ or $Fe(OH_2)^+Al$ groups and enhanced the adsorption process. Moreover, the inner ≡SiOH groups also showed minor interaction with $AO7^-$, due to difficulty in diffusion of dye within the pores (Sheme 1).

5.3.1 Adsorption and catalytic test

5.3.1.1 Adsorption of NaAO7

The adsorption behavior of NaAO7 dye (Fluka) is studied by contacting the powder (1g L^{-1}) with a 0.67 mM aqueous solution of NaAO7 dye at the starting pH of 6.8. The powders used for investigating the adsorption towards NaAO7, are: MeIMO, and Fe-x-MeIMO (x= 0.7 and 1.4 wt% of Fe) produced by ion exchange (IE) methods. Due to poor adsorption behavior Fe-doped powder with respect to MeIMO, the adsorption behavior of Fe-doped MeIMO obtained by direct synthesis method (DS) was not considered.

Aliquots of the suspension are collected at regular time intervals, during the adsorption tests. The suspended catalyst powder is separated from the solution by centrifuging (ALC centrifuge PK110, at the speed of 4000 rpm and for 4 min). The residual solution is measured by UV-vis spectroscopy in the 200-800 nm range (Cary 5000 UV-Vis-NIR spectrometer, Varian instrument), by using 1 mm path length quartz cell. The residual concentration of $AO7^-$ n the solution is measured

by the intensity of the main peak in adsorption of $AO7^-$ at 482 nm (*vide infra*) after calibration.

5.3.1.2 NaAO7 degradation

The degradation of NaAO7 in the presence of H_2O_2 is studied by contacting the powder (1g L^{-1}) with 0.67 mM aqueous solution of NaAO7 dye and 0.030 M H_2O_2. The powders used for investigating of the degradation of NaAO7 toward catalytic pathway, are MeIMO, Fe-x-MeMO (x= 0.7 and 1.4 wt% of Fe) produced with both IE and DS methods.

Aliquots of the suspension are collected at regular time intervals, during the catalysis tests. The suspended catalyst powder is separated from the solution by centrifuging (4000 rpm and for 4 min) and the residual solution is measured by UV-vis spectroscopy in the 200-800 nm range. The concentration of residual $AO7^-$ in the solution is measured by the intensity of the main peak in adsorption of $AO7^-$ at 482 nm.

In the presence of H_2O_2 the catalytic reaction takes place leading to the degradation of NaAO7 dye according to the below reaction:

$$C_{16}H_{11}N_2SO_4Na + 42H_2O_2 \rightarrow 16\,CO_2 + 46H_2O + 2HNO_3 + NaHSO_4 \quad (5-1)$$

According to reaction (5-1) the stoichiometric concentration of H_2O_2 necessary for complete degradation of NaAO7 dye is 0.03 M, which has been chosen during this analysis.

5.3.2 Results of adsorption and catalytic activity of MeIMO and Fe-doped MeIMO

The molecular structure and UV-Vs spectrum of NaAO7 dye in the water are reported in Scheme 5-3.

The hydrazone form of AO7 in the presence of water is stable in the solid phase. Therefore, the azo-hydrazone tautomerization takes place in water by intra-molecular proton transfer. Consequently, both hydrazone and azo-form are simultaneously present in water [85, 156]. The bands at 230 and 310 nm and the shoulder at 256 nm are assigned to electron transmissions of the aromatic rings.

The band at 482 is the maximum visible adsorption wavelength of the NaAO7 dye and is due to the n-π* transition involving the lone pair on N atoms and the connected system, which extend over the two aromatic moieties and include the N-N group of the hydrazone form [85, 156, 229-231] The small shoulder at 403 nm has a similar nature, including the *N–N* group of the azo-form [230, 232, 233].

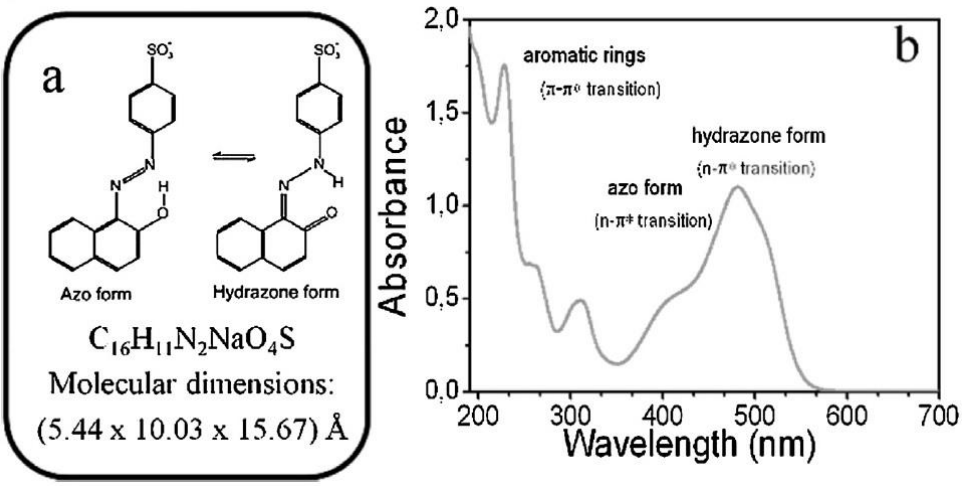

Scheme 5-3:(a) Structure formula and molecular dimension of AO7- dye, (b) UV-Vis spectroscopy of 0.67 mM aqueous solution of AO7 dye, with the corresponding adsorption bands due to azo- and hydrazone forms

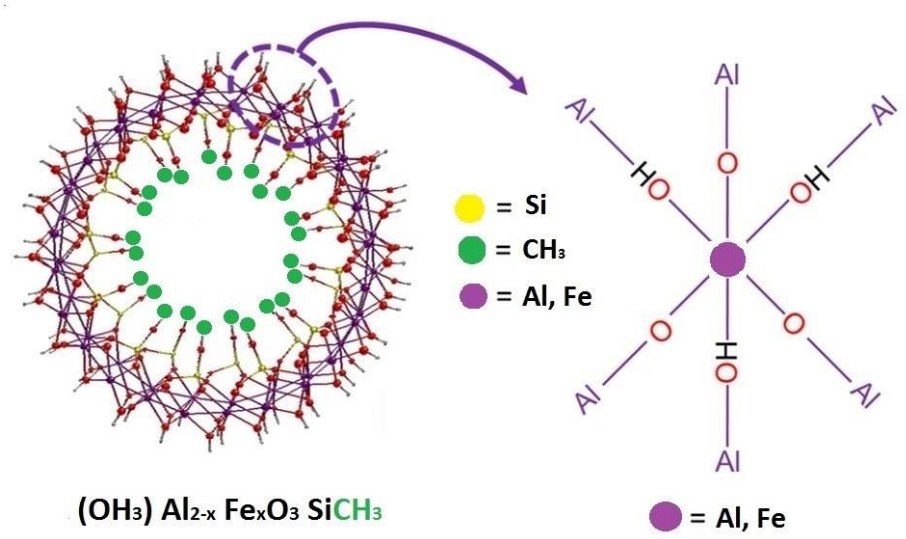

Scheme 5-4: MeIMO NTs and species present on the outer surface of this material before and after isomorphic substitution of Fe^{3+}/Al^{3+}

Figure 5-5 reports the UV-Vis spectra of supernatant solution after contact with the MeIMO and Fe-x-MeIMO-IE (x= 0.7 and 1 wt% of Fe) samples. Based on the spectra, no extra bands have been observed with respect to the initial NaAO7 solution, which indicate the minor adsorption process. Due to the hydrophobicity of inner surface of MeIMO type NTs, the interaction of dye with the inner pores is hindered. On the other hand, the fast process takes place on the C surface of NTs (Scheme 5-1) with the interaction of dye either with Al(OH)Al groups in the MeIMO NTs or with Fe(OH)Al groups in Fe-doped samples.

In the case of MeIMO, the minor adsorption of $AO7^-$ molecules at the first 120 min of process (46 %), indicate the electrostatically reaction of $AO7^-$ with the outer surface of NTs (Figure 5-6). However, in the case of the Fe-doped samples, the minor adsorption of $AO7^-$ molecules, for both samples with different amount of iron doping (32 %) indicate that only few Fe(OH)Al groups are protonated (Figure 5-6).

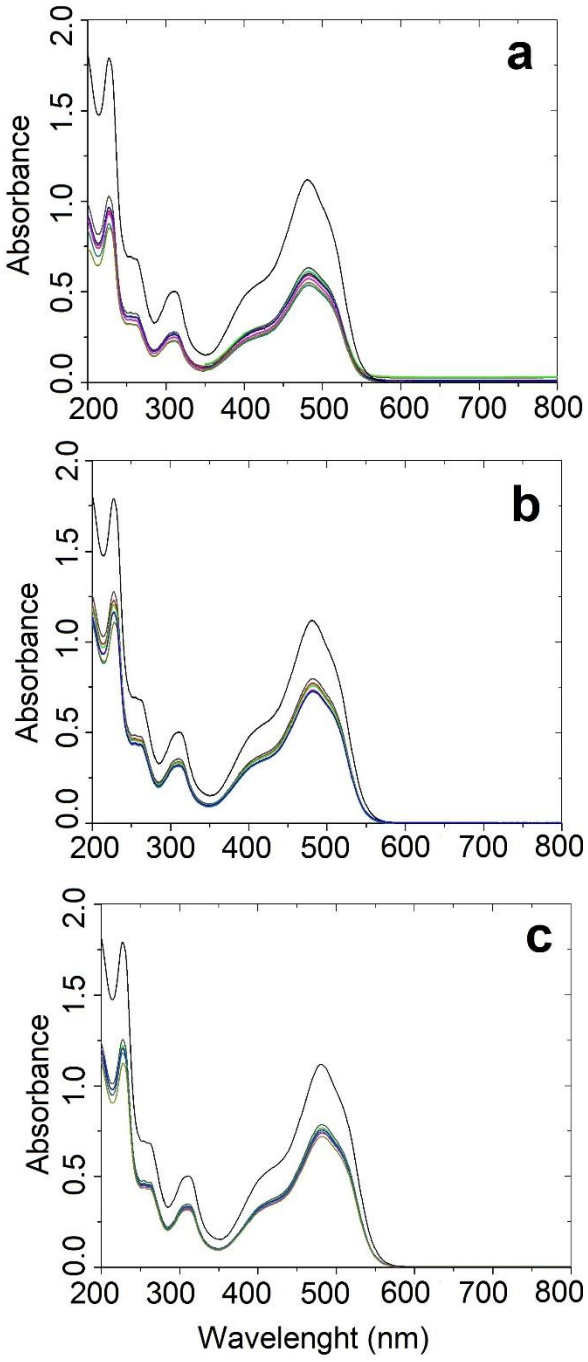

Figure 5-5: UV-Vis spectra of the starting AO7 solution (0.67 mM in water; bold black curve) and supernatant solutions obtained after different time intervals in contact with MeIMO (a) and Fe-0.7-MeIMO-IE (b) and Fe1.4-MeIMO-IE (c). The colors of spectra are assign to 10 min (gray), 1 h (red), 2 h (green), 5h (blue), 24 h (purple), 72 h (dark cyan) 96 h (dark yellow)

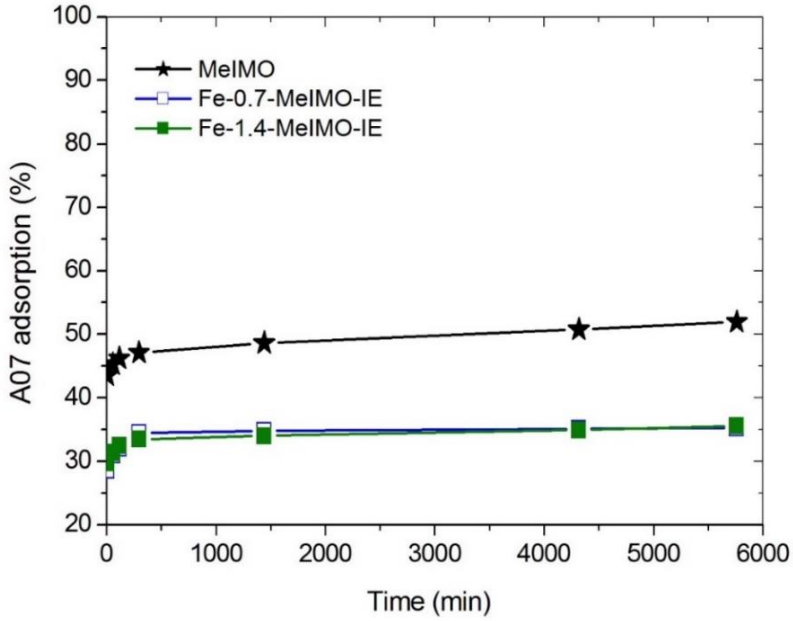

Figure 5-6: Percentage of AO7 adsorption by MeIMO (stars), Fe-0.7-MeIMO-IE (hollow squares) and Fe-1.4-MeIMO-IE (squares)

The results of NaAO7 degradation and catalytic reaction in the presence of 0.030 M H_2O_2 and 1g L^{-1} catalyst loading in dark condition is reported in Figure 5-7. Sections "a-e" of Figure 5-7 report the UV-Vis spectra of supernatant solution in contact with MeIMO and Fe-doped MeIMO samples, obtained by either direct synthesis or post synthesis in different time intervals, and section "f" compares the UV-Vis spectra of supernatant solution in contact with catalyst after 72 h from starting of the process. Figure 5-8 reports the total conversion (% of $AO7^-$ degradation) of the dye in contact with the corresponding catalysts.

According to spectra (Figure 5-7), for all samples the intensity of AO7 bands is decreased. However, for the whole experiment time, Fe-1.4-MeIMO-IE (93%) and MeIMO (73%) show higher $AO7^-$ removal respectively with respect to all other samples. Furthermore, in all Fe-doped samples either with direct synthesis or with ion exchange methods, those with higher iron loading (1.4 wt %) show the higher ability for $AO7^-$ removal, compared to the lower Fe-doped samples (0.7 wt %) (Figure 5-7f and Figure 5-8). Therefore, the total AO7- removal in the whole process time is decreased following this order: Fe-1.4-MeIMO-IE (93%) > MeIMO (73%) > Fe-1.4-MeIMO-DS (57%) > Fe-0.7-MeIMO-IE (45%) > Fe-0.7-MeIMO-DS (35%).

The high reactivity of the bare MeIMO is likely attributed to the presence of reactive aluminum sites on the outer surface of NTs, which is in agreement with the results reported by Shafia *et al.* [85] on the catalytic reactivity of imogolite NTs for degradation of NaAO7 dye. According to their study, the aluminum sites on the surface of imogolite NTs have higher reactivity in comparison with the similar ones at the surface of transition aluminas, which have been shown to be active in epoxidation reaction [85, 234-236]. The higher reactivity of aluminium sites at the surface of imogolite and MeIMO NTs, with respect to transition aluminas in the degradation $AO7^-$ can be attributed to the structure and the curvature on the surface of NTs Table 5-2 [85].

Regarding the lower reactivity of three Fe-doped samples (Fe-1.4-MeIMO-DS, Fe-0.7-MeIMO-DS and Fe-0.7-MeIMO-IE, Figure 5-7f, spectra 6, 3 and 4 respectively): doping iron in the NTs structure, results replacement of one Al^{3+} with one Fe^{3+} group and formation of three Fe(OH)Al and three FeOAl groups (Scheme 5-4). Based on this modification, the amount of Fe-related sites are high enough to affect the hydroxyl population at the outer surface, and change the surface properties of MeIMO NTs. Furthermore, the Fe^{3+} in the structure of NTs are highly coordinated, which may negatively affect their reactivity toward H_2O_2 molecules. Simultaneously, the presence of H_2O_2 interferes the interaction of Fe^{3+} and $AO7^-$ species which is in agreement with the previous observations obtained by Shafia *et al.* [85] on the reactivity of imogolite NTs.

In the case of Fe-1.4-MeIMO-IE NTs, the higher catalytic reactivity of this sample with respect to other Fe-doped samples, is likely due to the presence of some Fe^{3+} ions in the solution. The origin of Fe^{3+} ions is probably the clusters within the NTs structure. The presence of these Fe^{3+} ions motivates the occurrence of Fenton-like reaction and enhances the dye degradation according to the below reactions:

$$Fe^{2+} + H_2O_2 \rightarrow Fe^{3+} + OH^{\cdot} + OH^- \quad (5-2)$$

$$Fe^{3+} + H_2O_2 \leftrightarrow H^+ + Fe(HO_2)^{2+} \quad (5-3)$$

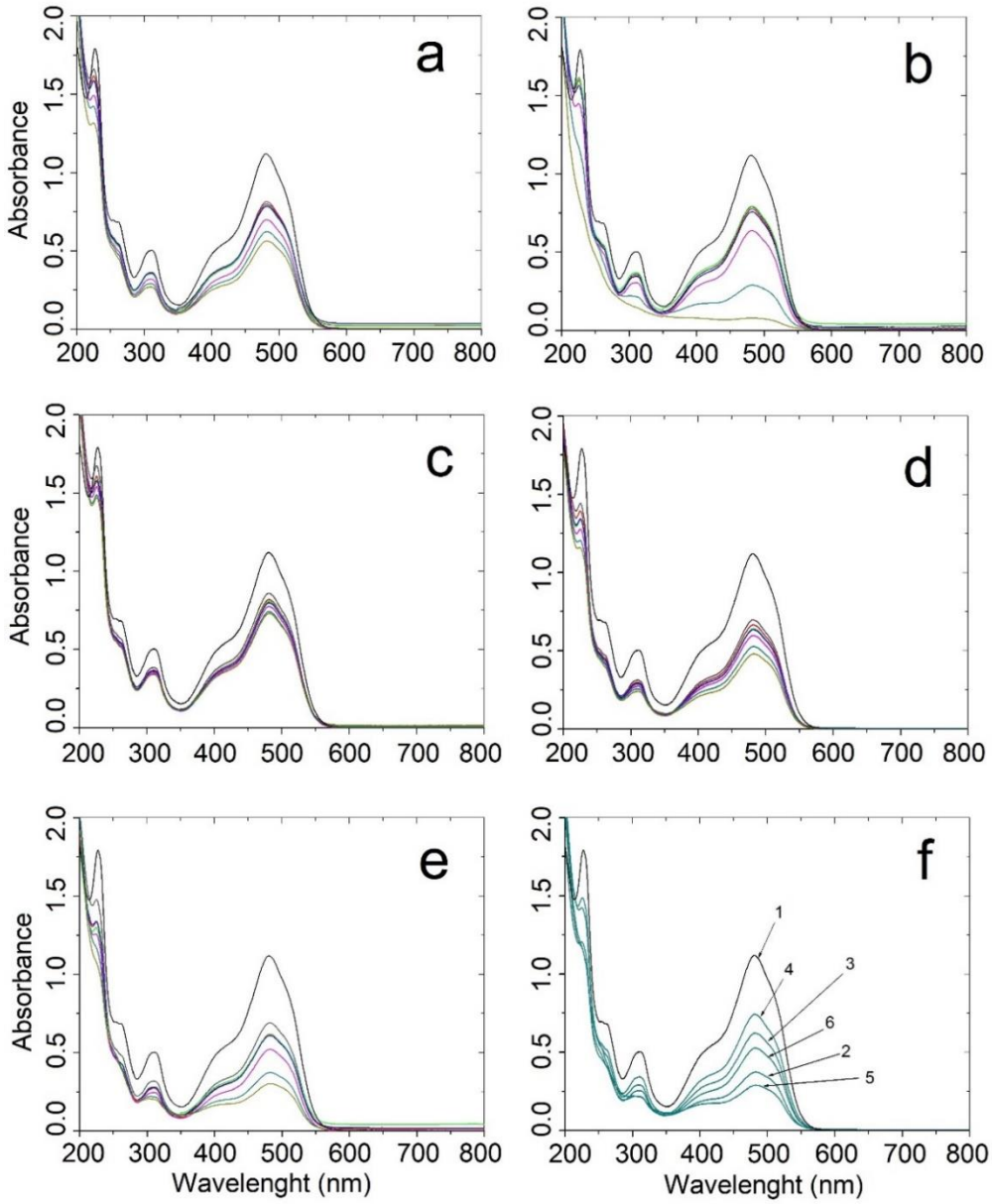

Figure 5-7:UV-Vis spectra of starting 0.67 mM AO7 solution (bold black curve) and of the supernatant solution after different time intervals in contact with 0.03M H_2O_2 and Fe-0.7-MeIMO-IE (a), Fe-1.4-MeIMO-IE (b), Fe-0.7-MeIMO-DS (c), Fe-1.4-MeIMO-DS (d) and MeIMO (e). (f) Comparison between UV-Vis spectra of starting AO7 solution (curve 1) and of the supernatant solution obtained after 72h in contact with 0.03 M H_2O_2 and MeIMO (curve 2), Fe-0.7-MeIMO-IE (curve 3), Fe-0.7-MeIMO-DS (curve 4), Fe-1.4-MeIMO-IE (curve 5) and Fe-1.4-MeIMO-DS (curve 6). The colors of spectra are assign to 10 min (gray), 1 h (red), 2 h (green), 5h (blue), 24 h (purple), 72 h (dark cyan) 96 h (dark yellow)

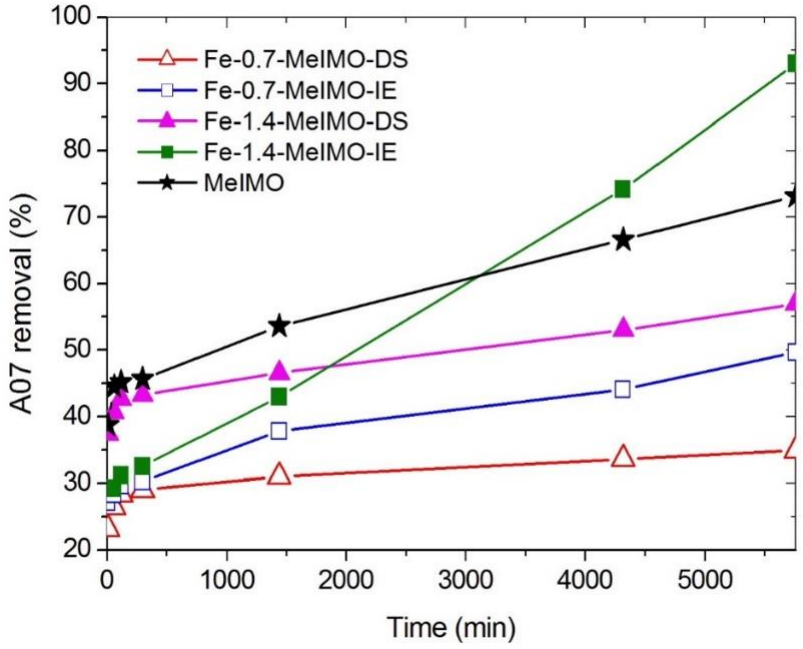

Figure 5-8: Percentage of AO7 conversion obtained by MeIMO (stars), Fe-0.7-MeIMO-DS (hollow triangles), Fe-0.7-MeIMO-IE (hollow squares), Fe-1.4-MeIMO-DS (triangles) and Fe-1.4-MeIMO-IE (squares)

Table 5-2: Catalytic conversions as obtained with 0.030 M H_2O_2 and 0.67 mM AO7 in water

Catalyst	**Conversion with 0.030 M H_2O_2 (%)**
MeIMO	73
Fe-0.7-MeIMO-IE	45
Fe-1.4-MeIMO-IE	93
Fe-0.7-MeIMO-DS	35
Fe-1.4-MeIMO-DS	57
γ-Al_2O_3	35
None	5.0

5.4 Conclusions

MeIMO and Fe-doped MeIMO NTs present strong and mild acidic sites, according to IR spectra of adsorbed pyridine on different Lewis and Brønsted sites and reversible desorption up to 250 °C for MeIMO and 150 °C for Fe-doped MeIMO ones. The thermally collapsed samples (samples preheated up to 500 °C) exhibit stronger acidic properties due to Lewis and Brønsted sites. The strong acidic sites of collapsed samples are ascribed to the formation of Al-related sites, and different Al coordination with respect to NTs.

Studying the reactivity of MeIMO and Fe-doped samples in water with H_2O_2 for adsorption and degradation of azo-dye, imply the notable reactivity of MeIMO for both adsorption and degradation of dye, due to reactive aluminum sites on the outer surface of NTs. Nonetheless the presence of highly coordinated Fe^{3+} in iron-doped samples negatively affects the reactivity of these samples in the presence of H_2O_2. However, at higher iron loading and especially in ion exchange method, the probability of the presence of some Fe^{3+} ions in solution coming from iron-containing clusters, provokes the Fenton-like reaction and higher reactivity toward dye degradation.

Chapter 6

Photo-Activated Degradation of Tartrazine by H_2O_2 as Catalyzed by Both Bare and Fe-Doped MeIMO Nanotubes and the Related Collapsed Phases

6.1 Introduction

Tartarazine E102 (TRZ, Scheme 6-1) is a synthetic azo dyes, which is widely used as a food coloring agents. TRZ, is recalcitrant to biodegradation under aerobic conditions, and appears to be responsible of the most allergic and/or intolerance reactions in comparison to the other azo dyes. Advanced oxidation processes (AOPs), implying the production of reactive oxygen species (above all the hydroxyl radical HO·), are currently considered a powerful method for the *in situ* remediation of both wastewater and contaminated groundwater [238].

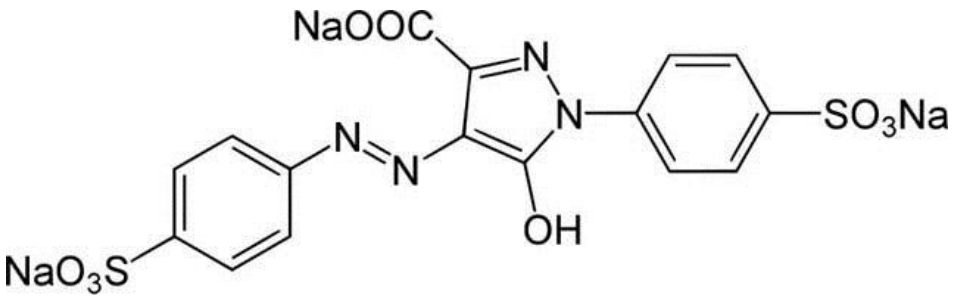

Scheme 6-1: Structure formula of tartrazine (TRZ)

HO· radicals may be produced in contaminated aquifers by the well-known Fenton reaction (eq. 6-1): Fe^{2+} ions are introduced into groundwater, and concentrated hydrogen peroxide (H_2O_2) is added in order to oxidize Fe^{2+} ions to Fe^{3+} ions and to produce HO· species. However, after oxidation of Fe^{2+} to Fe^{3+}, the overall oxidation rate decreases due to (slower) reduction of Fe^{3+} to Fe^{2+} (eq. 6-2 and 6-3) [239, 240]. By applying UV irradiation, the so-called photo-assisted Fenton reaction (or photo-Fenton system) occurs [241], through which Fe^{2+} species are regenerated by photolysis of Fe^{3+} hydroxide complexes yielding additional HO· radicals (eq. 6-4 and 6-5) and, simultaneously, photocatalytic decomposition of H_2O_2 occurs (eq. 6-6):

$$Fe^{2+} + H_2O_2 \rightarrow Fe^{3+} + HO\cdot + OH^- \qquad (6-1)$$

$$Fe^{3+} + H_2O_2 \leftrightharpoons H^+ + Fe(HO_2)^{2+} \qquad (6-2)$$

$$Fe(HO_2)^{2+} \rightarrow Fe^{2+} + HO_2\cdot \qquad (6-3)$$

$$Fe(OH)^{2+} + h\nu \rightarrow Fe^{2+} + OH^{\cdot} \qquad (6-4)$$

$$Fe^{3+} + H_2O + h\nu \rightarrow HO\cdot + Fe^{2+} + H^+ \qquad (6-5)$$

$$H_2O_2 + h\nu \rightarrow 2HO\cdot \qquad (6-6)$$

For an actual application of the photo-Fenton method to wastewater treatment, homogeneous catalysts bring some limitations, due to production of Fe-containing sludge, catalyst deactivation and limited range of operating pH [242]. Several studies have been also carried out on heterogeneous photo-Fenton systems implying, for instance, the use of Fe/HY zeolite for the degradation of polyvinyl alcohol [243], the photo-Fenton oxidation of phenol [244] as catalyzed by Fe species incorporated in different silica supports, and the oxidation of Acid Orange 7 (a model molecule of many azo dyes) by Fe-bentonite and Fe-laponite catalysts [245]. Moreover, Saninno *et al.* studied the application of structured catalysts (namely $LaFeO_3$ and $Pt/LaFeO_3$ perovskites supported on different cordierite or corundum honeycomb monoliths) in the heterogeneous photo-Fenton removal of TRZ [246, 247].

Among nanomaterials with potential application as heterogeneous catalysts, there is a growing interest for imogolite-related materials, as testified by the recent studies on their synthesis [141, 248-251], structure [111, 143, 252], electronic states [62, 253], stability [62, 199], and application as catalyst and/or catalytic support [8, 21].

The subject of this chapter is treated in an article that we have already submitted concerning the catalytic behavior of MeIMO, along with Fe-doped MeIMO obtained by ionic exchange (IE) and of the phases stemming by the thermal collapse of NTs. Two Fe contents were considered: 0.7 and 1.4 wt. % Fe. According to the results of previous chapters and also based on previous studies on Fe-doped imogolite NTs, Fe may isomorphically substitute for Al up to 1 wt. %, whereas at Fe loadings as high as 1.4 wt. % Fe oxo-hydroxide clusters formation occurs along with IS, NTs formation being instead hindered at higher loadings [21, 23, 24, 85].

The specific structure and different porosities in the dry powder of MeIMO NTs with hexagonal packing (Scheme 2-3 and Scheme 5-1) (Intra-tube pores (A) have ≅ 2.0 nm diameter; inter-tube pores (B) among three aligned NTs in a bundle have *ca.* 0.45 nm diameter and larger C mesopores are disordered slit-pores occurring among bundles [11, 78-80], giving rise to potential use of this material for catalysis.

So far, no specific study has been devoted to Fe-doped MeIMO NTs, nor to their application as heterogeneous catalysts in the degradation of TRZ. Shafia *et al.* obtained Fe-doped imogolite NTs by both direct synthesis and post-synthesis ionic exchange [23, 85, 254], the latter result opening the possibility to dope imogolite without perturbing the (delicate) hydrolysis equilibria leading to NTs formation. Furthermore, the band gap (E_g) of imogolite, an insulator with E_g = 4.9 eV,

decreased to 2.4-2.8 eV in Fe-doped NTs that ultimately show semiconducting properties [23, 24, 254]. Moreover, the outer surface of imogolite NTs forms reactive Al-OOH groups in the presence of H_2O_2 [85] and show remarkable catalytic properties in the degradation of Acid Orange 7 under dark conditions. The reactive Al-OOH groups also have been observed for MeIMO NTs in particular, for the degradation of NaAO7 in previous chapter. Indeed, it is expected that such groups (Al-OOH) be photo-catalytically active under UV light when MeIMO is used as photo-catalyst. Moreover, in the presence of UV light Fe-doped MeIMO could trigger a photo-Fenton process (eq. 1-6).

A further aspect considered in the present chapter was the catalytic activity of the structure stemming from NTs thermal degradation: previous chapters showed that after thermal treatment at 500 °C MeIMO NTs collapse into a buckled structure (Scheme 4-3), which retains high surface area and porosity remaining suitable for catalytic purposes [25]. The photo-catalytic activity of such collapsed phases was also addressed in this paper, with particular attention to the effect of the new environments surrounding both Al and Fe in the buckled structure as discussed in Chapter 4. After MeIMO NTs thermal collapse, the Al coordination changes from octahedral to both tetrahedral and pentacoordinated Al [25], which could led to the formation of more reactive Al-OOH groups, whereas the new environment surrounding Fe in the collapse phase is expected to affect its photo-Fenton performance, when the material is exposed to H_2O_2 and UV light.

6.2 Experimental Section

6.2.1 Materials synthesis

The as-synthesis MeIMO was obtained according to synthesis procedure discussed in chapter 2. Two Fe-x-MeIMO samples (x= 0.7 and 1.4 wt. % Fe) were obtained by ionic exchange of MeIMO NTs, as discussed briefly in chapter 3.

Thermally collapsed samples were obtained by calcining aliquots of both MeIMO and Fe-0.70-MeIMO-IE at 500 °C for 4 h in air [25] (the collapsing procedure did not concern Fe-1.4-MeIMO-IE sample, which showed a poorer catalytic activity (*vide infra*), and therefore its collapsed phase was not considered). The collapsed samples are hereafter labeled with an ending –c (*e.g.* MeIMO-c stands for the collapsed phase obtained from MeIMO).

6.2.2 TRZ degradation tests

Tests were carried out on 160 ml aqueous solution of TRZ (purity grade > 99.0%; initial concentration = 40 ppm; initial pH = 6.4) in a stainless-steel sealed batch photoreactor designed by Sannino *et al.* (Scheme 6-2) [255]. After catalyst addition (0.25 g L^{-1}), the suspension was continuously stirred by nitrogen fine bubbling and external recirculation by a peristaltic pump (Watson Marlow). Before re-entering the reactor, the solution was cooled down by means of a cold trap in order to maintain a constant temperature of 25 °C. The outlet gases pass through a cold trap (0 °C) in order to assure water condensation, prior entering the gas analyzer (Uras 14, ABB) for CO_2 concentration measurement.

In order to investigate the effect of pH, the initial pH of the solution was changed to either acidic conditions (pH = 3.0, by addition of HCl) or basic conditions (pH = 10.0, by addition of NH_3).

A Perkin Elmer UV-Vis spectrophotometer (λ_{max} = 426 nm) was used to measure TRZ concentration, in order to study discoloration. TRZ initial concentration C_0 (without catalyst) was measured at time t = 0, the 8 W mercury vapor lamp emitting at 254 nm was then placed inside the photoreactor with tight connections. The system was kept in dark conditions for 3 h, in order to reach adsorption/desorption equilibrium of TRZ at catalyst surface. During the tests, TRZ concentration was analyzed by monitoring changes in absorbance at λ_{max}=426 nm at different time intervals. After 3 h, UV irradiation started and, simultaneously, H_2O_2 was continuously dosed by means of a peristaltic pump (Miniplus 3-GILSON). Three different H_2O_2 flow rates were adopted (0.019, 0.038 and 0.057 mol h^{-1}).

The catalytic performance was evaluated in terms of Total Organic Carbon (TOC) removal:

$$TOC_{(removal\%)} = \frac{TOC_0 - TOC_t}{TOC_0} \qquad (6-7)$$

where TOC_0 is the initial TOC ($t = 0$) and TOC_t is the TOC value after a given irradiation time t.

The TOC_0 of the reference aqueous solution (solely containing 40 ppm TRZ as initial concentration C_0) corresponds to 17 ppm. The TOC as a function of time (TOC_t) was evaluated by means of high temperature catalytic combustion in a tubular flow microreactor operating at 953 K, with a stream of hydrocarbon-free air to oxidize the organic carbon (catalyst: Pt/Al_2O_3).

The reaction products in the gas phase were monitored by continuous gas analyzers (Uras 14, ABB) measuring the gaseous concentration of CO, CO_2 at the outlet of the photo-reactor.

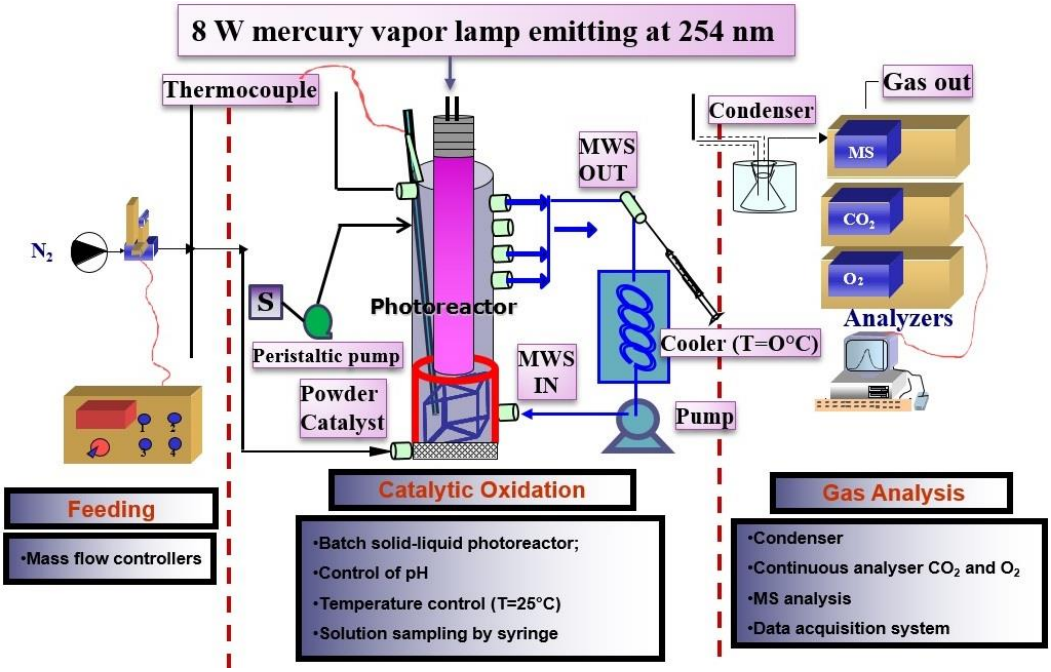

Scheme 6-2: Laboratory apparatus for the catalytic photo-Fenton oxidation [255]

6.3 Results and discussions

6.3.1 Powders characterization

The X-ray Powder Diffraction (XRD), BET surface area and UV-Vis spectroscopy have been performed for analyzing the structure of all powder samples (MeIMO, Fe-0.7-MeIMO-IE and Fe-1.4-MeIMO-IE), even in as-synthesis form or collapsed form. Nevertheless, all characterization have been discussed in chapter three and four. In order to avoid unnecessary repetition, surface characterization presented earlier are not reproduced in this chapter.

Figure 6-1 reports ζ-potential curves obtained with MeIMO, Fe-0.7-MeIMO-IE and Fe-1.4-MeIMO samples. MeIMO NTs (stars) are positively charged at low pH values, and the point of zero charge (PZC) is found at pH 8.8, a value close to

that of both imogolite [136] and transition aluminas [256], in agreement with the chemical composition of NTs outer surface. The ζ-potential curves and PZC values of MeIMO and Fe-0.70-MeIMO-IE are very close, due to the low Fe content in the latter sample [23, 85]: with both samples, the outer surface of NTs is positively charged below pH 8.8, and therefore prone to interact with TRZ anions. Conversely, the PZC of Fe-1.4-MeIMO sample (Table 1) is found at lower pH, most likely due to a higher amount of Fe oxo-hydroxide clusters (as observed in the UV-Vis spectrum, Fig 4-11), which affect PZC value, although the presence of some residual chloride ions coming from the Fe-precursor could contribute to PZC lowering as well [257]. The ζ-potential curves of collapsed samples differ from those of the parent samples: both MeIMO-c and Fe-0.70-MeIMO-IE-c are negatively charged in a wide range of pH. Their lower PZC values, close to that of amorphous silica (between 1.9 – 3.5), indicate the occurrence of a new phase, where the surface accessible after NTs collapse likely contains silicon oxide patches, in agreement with eq. 8 and 9 and with the literature [257, 258]. The remarkable change in ζ-potential curves after collapsing is also in agreement with the UV-Vis spectral features of Fe-0.7-MeIMO-IE-c, indicating that Fe species reacted with the alumino-silicate phase resulting embedded in the buckled structure in a different environment with respect to the parent sample.

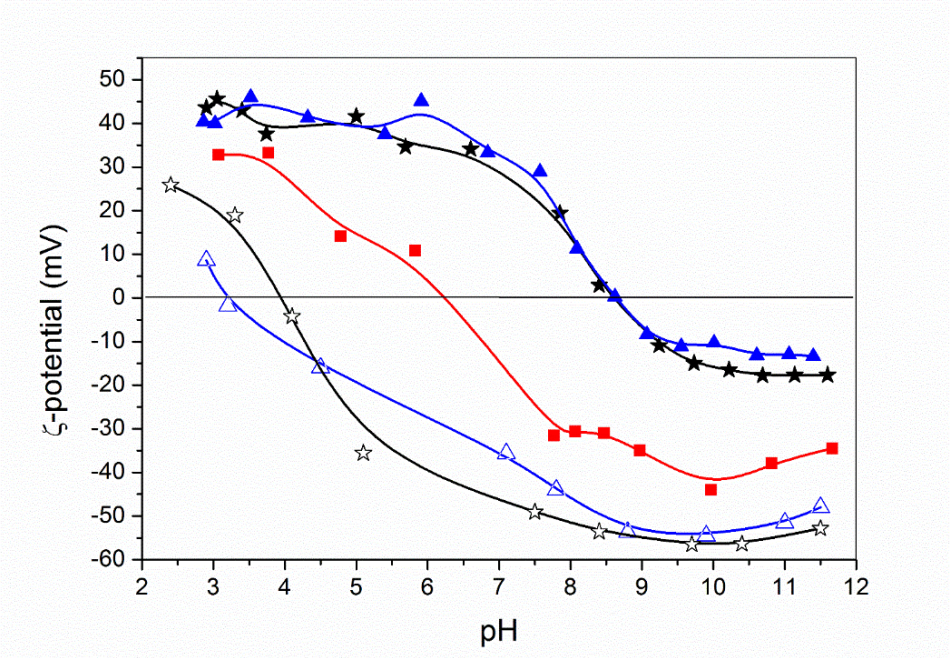

Figure 6-1: ζ-potential curves of MeIMO (full stars), MeIMO-c (hollow stars), Fe-0.70-MeIMO-IE (full triangles), Fe-0.70-MeIMO-IE-c (hollow triangles) and Fe-1.4-MeIMO-IE (full squares)

6.3.2 Results of TRZ degradation

Figure 6-2a and 6-2b report curves of TRZ discoloration and mineralization, respectively: measurements were carried out at natural pH of the solution (pH = 6.4) and H_2O_2 was continuously dosed with the constant 0.038 mol h^{-1} rate after starting UV irradiation. TRZ discoloration (Figure 6-2a) is reported as C/C_0 where C_0 is the initial absorbance ($t = 0$) and C is the absorbance at reaction time *t*.

In the absence of UV irradiation, the curves of as-synthesized samples in Figure 6-2a show *ca.* 10-20 % rapid discoloration during the first 10 min, due to some non-equilibrium adsorption/diffusion phenomena likely followed by some desorption, until equilibrium is reached after *ca.* 2 h. Collapsed samples did not show an appreciable TRZ adsorption, in agreement with their surface charge (*vide supra*).

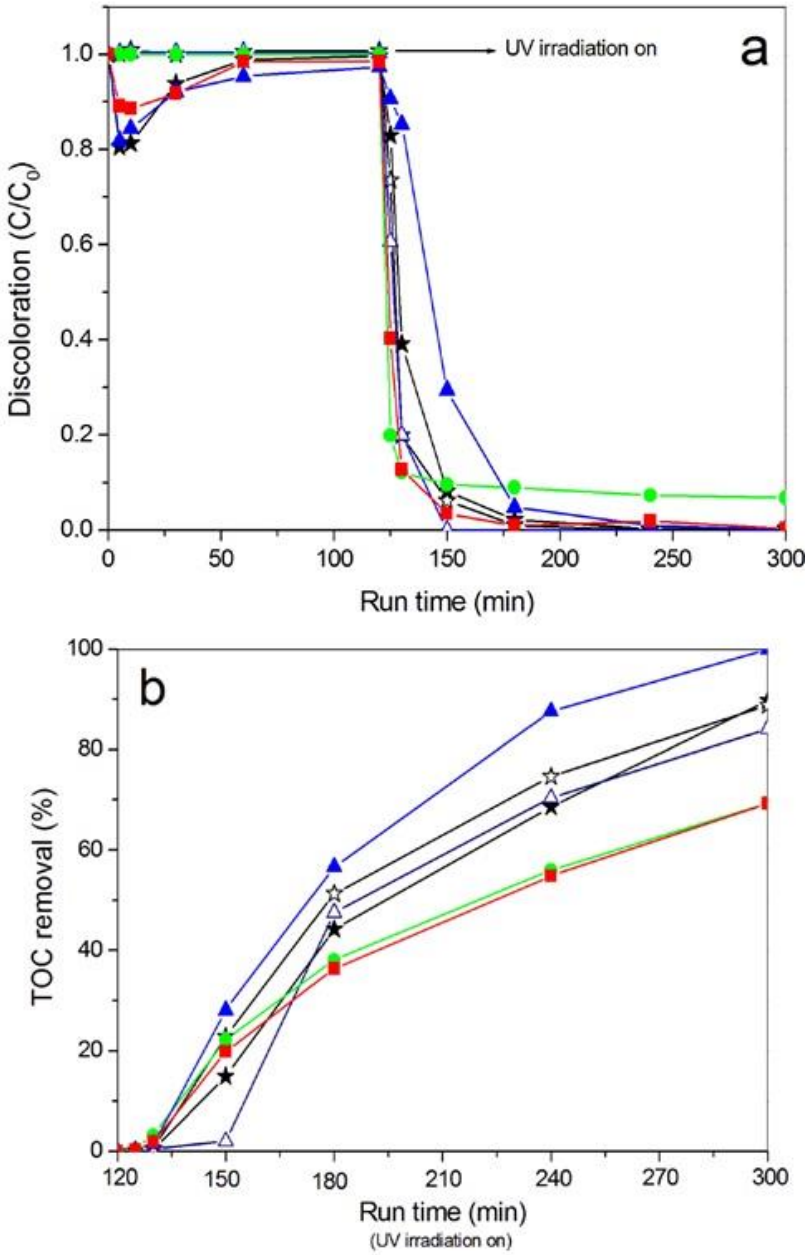

Figure 6-2: Discoloration (a) and mineralization (b) of TRZ by photolysis (circles) and in the presence of MeIMO (full stars), MeIMO-c (hollow stars), Fe-0.7-MeIMO-IE (full triangles), Fe-0.7-MeIMO-IE-c (hollow triangles) and Fe-1.4-MeIMO-IE (squares)

After starting UV irradiation, in the absence of catalyst (green circles in Figure 6-2a) TRZ discoloration by mere photolysis reached 90 %, remaining constant at longer irradiation time, meaning that UV light alone was ineffective in the degradation of TRZ intermediates. Conversely, in the presence of the studied catalysts total discoloration occurred after almost 2 h under UV irradiation.

Inspection of Figure 6-2a shows that Fe-0.70-MeIMO-IE-c was very effective towards UV-induced discoloration: after thermal collapse Fe is mostly embedded in the alumino-silicate matrix as the species absorbing at 270 nm n UV-Vis spectra of powder samples (Figure 4-11), reducing the amount of Fe oxo-hydroxide species, which have a detrimental effect on photo-degradation (*vide infra*). Fe-1.4-MeIMO reached 100 % discoloration before MeIMO and Fe-0.70-MeIMO-IE, likely due to the higher amount of IS Fe^{3+} sites active in the photo-Fenton process. Interestingly, MeIMO was also effective, due to reactive Al-OOH groups formed by reaction with H_2O_2 and which, under UV light, promptly release HO· species able to attack organic moieties.

Summarizing, TRZ discoloration occurs through different mechanisms. Concerning non-reactive pathways, electrostatic interaction plays a role, as already observed between anions of the azo dye Acid Orange 7 and (positively charged) imogolite NTs [23, 85]. The dye moieties may also adsorb/diffuse within the pores of as-synthesized materials and, finally, N atoms of TRZ may coordinate Fe^{3+} sites in Fe-doped samples, through a ligand displacement mechanism [23, 85]. Concerning reactive pathways, though photo-Fenton reaction occurs with all the Fe-containing samples, also very reactive Al-OOH groups form in the presence of H_2O_2 [85].

Concerning TRZ mineralization (Figure 6-2b), after 3 h under UV irradiation TOC removal decreases as follows: Fe-0.70-MeIMO-IE (100%) > MeIMO ≅ MeIMO-c (90%) > Fe-0.7-MeIMO-IE-c (83%) and Fe-1.4-MeIMO (69%). The interaction between TRZ ions and accessible Fe3+ ions in Fe-0.70-MeIMO-IE (full triangles) likely results in a more effective mineralization of TRZ by photo-Fenton process (eq. 4-6). This is in agreement with previous work by Shafia *et al.* showing that Acid Orange 7 anions may also adsorb at the surface of Fe-doped imogolite NTS through a ligand displacement mechanism, with N atoms coordinating Fe^{3+} ions [23, 85].

Conversely, Fe^{3+} sites in the buckled structure of Fe-0.70-MeIMO-IE-c (the most active sample towards discoloration) seems less active towards TRZ mineralization with respect to Fe^{3+} sites in Fe-0.70-MeIMO-IE: such result could

be ascribed to some hindered diffusion of TRZ intermediates within the micropores of the buckled structure, which hampers mineralization. All this notwithstanding, the TOC removal obtained with Fe-0.70-MeIMO-IE-c was higher than with Fe-1.4-MeIMO. A higher Fe content has a detrimental effect on TRZ removal, in that with Fe-1.4-MeIMO sample the TOC removal almost equals mere photolysis (Figure 6-2b, squares): this may be due to the Fe oxo-hydroxide clusters having a lower photo-Fenton reactivity as compared to IS Fe^{3+}sites. Such clusters may also catalyze the decomposition of H_2O_2 to water and oxygen [259, 260], a process that decreases the production rate of HO· radicals. Nonetheless, the electric field surrounding Fe oxo-hydroxide clusters may negatively affect the separation of photo-induced electron–hole pairs.

The remarkable activity of MeIMO towards TRZ mineralization can be accounted for by the formation of the aforementioned Al-OOH groups. The same reactivity towards H_2O_2 was already observed with some transition aluminas [234-236] and imogolite NTs, the latter being able to degrade Acid Orange 7 in the presence of H_2O_2 even in dark conditions [23, 85]. Concerning MeIMO-c, previous Solid State NMR study showed that the coordination of some *Oh* Al^{3+} sites in MeIMO changes [8, 25, 143] to tetra- and pentacoordinated Al sites in the buckled structure, as also observed with amorphous aluminosilicates with similar Si/Al ratio [261], with the likely formation of some oxygen vacancies [262]. Such tetra- and pentacoordinated Al sites present in MeIMO-c can produce reactive HO· radicals in the presence of H_2O_2 and UV irradiation, finally explaining the sizeable catalytic activity of the collapsed material.

The best catalyst in terms of TOC removal (*i.e.* Fe-0.70-MeIMO-IE sample) was then used for further experiments testing stability and the effects of H_2O_2 dosing rate, catalyst dosage and initial pH.

6.3.3 Stability experiments on Fe-0.70-MeIMO-IE sample

With the aim to evaluate the stability of the Fe-0.70-MeIMO-IE sample, recycling experiments under UV light irradiation were performed for five cycles under the same experimental conditions. After 180 min reaction, the sample was separated by centrifugation and the recovered catalyst powder was washed several times with distilled water, before being re-dispersed into a (fresh) aqueous solution of TRZ. After five recycling tests, Fe-0.70-MeIMO-IE sample did not show significant loss in activity, since TRZ discoloration and TOC removal remained constant at about 98 and 97%, respectively, as shown in Figure 6-3. Accordingly, the results of leaching test showed that Fe concentration, as determined by ICP-AES, in the

treated solutions after the fifth photo-Fenton test was very low, *i.e.* about 0.3 mg L^{-1}, indicating a nearly negligible, and therefore acceptable, Fe dissolution from the Fe-0.70-MeIMO-IE sample. Such results indicate that the Fe-0.70-MeIMO-IE sample is a stable photocatalyst confirming the reproducibility of the photo-Fenton process in the treatment of aqueous solutions containing the target dye.

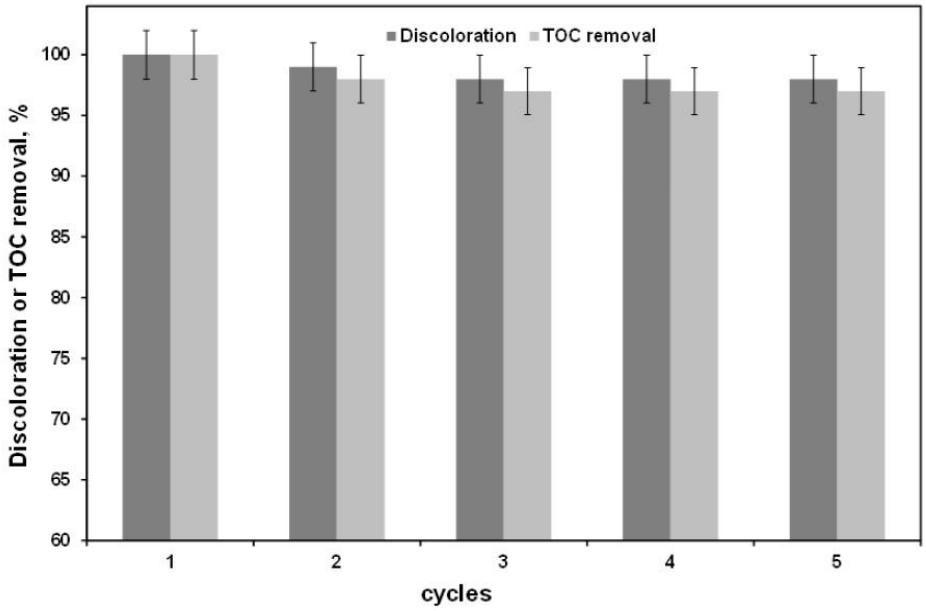

Figure 6-3: TRZ discoloration and TOC removal after 180 min under UV irradiation as obtained with the Fe-0.70-MeIMO-IE catalyst for five cycles. H_2O_2 dosage rate 0.038 mol h^{-1}; catalyst dosage: 0.25 g L^{-1}; initial dye concentration: 40 ppm; initial pH of solution: 6.4.

6.3.4 Effect of continuous H_2O_2 dosage rate

Previous studies showed that H_2O_2 dosage rate directly affects the efficiency of photo-Fenton reaction; furthermore, in the presence of continuous H_2O_2 dosage, the maximum value of CO_2 production, contributing to TOC removal, is higher than a H_2O_2 dosage with the same amount once at the beginning of the test [263].

The effect of H_2O_2 continuous dosage on photo-Fenton removal of TRZ at a constant pH of 6.4 was studied at three different flow rates (0.019 mol h^{-1}, 0.038 mol h^{-1} and 0.057 mol h^{-1}) in the presence of Fe-0.70-MeIMO-IE (the best catalyst in terms of TOC removal). The corresponding results of discoloration and TOC removal are reported in Figure 6-4a and 6-4b, respectively.

According to Figure 6-4a, the decrease in H_2O_2 flow rate from 0.038 mol h^{-1} to 0.019 mol h^{-1} improves discoloration, whereas at both rates total TOC removal was reached in 3 h. A rate increase to 0.057 mol h^{-1} did not affect much discoloration (Figure 6-4a) and negatively affected mineralization, as the TOC removal decreased (Figure 6-4b). Such results underline the fact that TRZ discoloration mainly occurred through reaction between HO· radicals (produced from H_2O_2 under UV light) and TRZ moieties, both species being in liquid phase, whereas the heterogeneous catalytic process played an important role in TOC removal (Figure 6-4b), as already observed in the heterogeneous photo-Fenton removal of the azo dye Orange D [264]. At low and intermediate H_2O_2 flow rate, Fe^{3+} species resulted in the production of more HO· radicals, which accelerated the mineralization of TRZ (eq.1, 5 and 6) [260]. Conversely, a further increase in H_2O_2 flow rate to 0.057 mol h^{-1} resulted in worsening the overall TOC removal performance, likely due to HO· radical consumption, through the following "parasitic" reactions [265]:

$$HO\cdot + H_2O_2 \rightarrow HO_2.\ + H_2O \qquad (6-8)$$

$$HO_2\cdot + HO\cdot \rightarrow O_2 + H_2O \qquad (6-9)$$

The reaction reported in eq. (6-8) produces HO_2· radicals, which are weaker oxidizing species with respect to HO· radicals and, nonetheless, may also react with HO· radicals (eq. (6-9)) consuming the latter species.

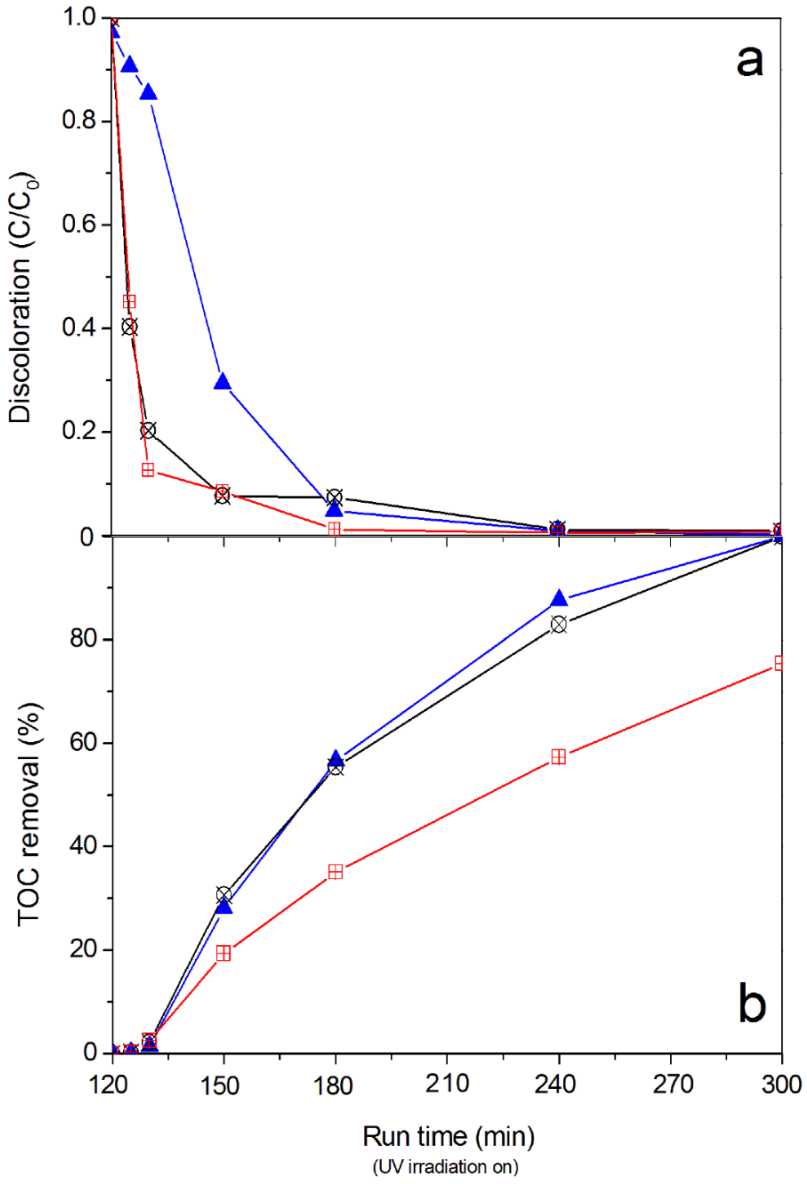

Figure 6-4: Influence of continuous H_2O_2 dosage rate on TRZ discoloration (a) and mineralization (b): 0.019 mol h^{-1} (circles), 0.038 mol h^{-1} (triangles) and 0.057 mol h^{-1} (squares). Catalyst: Fe-0.70-MeIMO-IE; initial dye concentration: 40 ppm; initial pH of solution: 6.4

6.3.5 Effect of Fe-0.70-MeIMO-IE dosage on the photo-Fenton reaction

The effect of catalyst concentration on the photo-Fenton process was studied with Fe-0.70-MeIMO-IE: results concerning TRZ discoloration and TOC removal at 0.25 and 1 g L^{-1} catalyst concentration are reported in Figure 6-5a and 6-5b, respectively.

As discussed before, at lower catalyst dosage, both discoloration and mineralization occurred gradually, and 100 % TOC removal was reached after 3 h under UV irradiation (Figure 6-5a, triangles). By increasing the catalyst dosage to 1 g L^{-1}, instead, *ca.* all TRZ was adsorbed at the photocatalyst surface in the first 10 min in dark conditions (Figure 6-5a, diamonds) and, consequently, 100 % TOC removal was reached almost immediately under UV irradiation (Figure 6-5b, diamonds). Comparison of the amount of carbon consumed during reaction (as assessed by TOC analysis with 1 g L^{-1} Fe-0.70- MeIMO-IE) and the amount of carbon released as CO_2 (as measured by catalytic combustion) leads to carbon mass balance very close to 100%. Such result supports the conclusion that adsorbed TRZ is selectively converted to CO_2 in the presence of 1 g L^{-1} Fe-0.70-MeIMO-IE, as previously observed in the photo-Fenton removal of acetic acid carried out in the same photoreactor [265].

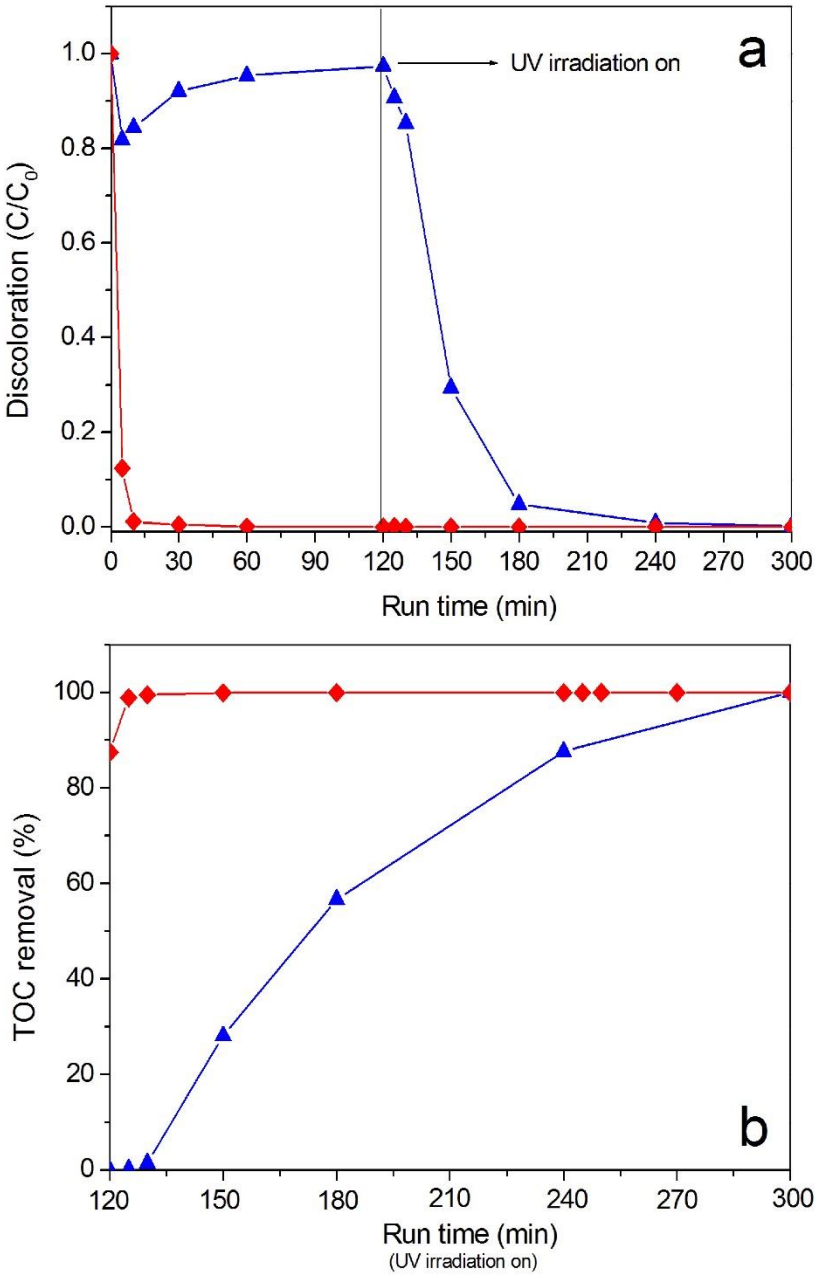

Figure 6-5: Influence of catalyst concentration on (a) discoloration and (b) mineralization of TRZ with Fe-0.70-MeIMO-IE catalyst: 0.25 g L^{-1} (triangles) and 1 g L^{-1} (diamonds)

6.3.6 Effect of pH on the photo-Fenton reaction

Figure 6-6 reports the effect of pH on both discoloration (a) and TOC removal (b) during photo-Fenton tests carried out with 0.25 g L^{-1} Fe-0.70-MeIMO-IE and 0.038 mol h^{-1} H_2O_2 flow rate at three different initial pH values (3.0, 6.4 and 10.0). As expected, pH modifies NTs adsorption properties, and therefore their discoloration behavior in dark conditions (Figure 6-6a): pH plays an important role on the amount of TRZ adsorbed at Fe-0.70-MeIMO-IE surface, in that the equilibrium adsorption capacity of the catalyst is lower at pH 10.0, when the surface is negatively charged, whereas maximum TRZ adsorption is achieved at pH 3.0, in agreement with ζ-potential measurements. At higher pH the amount of positive charges at Fe-0.70-MeIMO-IE surface decreases, hampering adsorption of TRZ ions [266] and ultimately leading to electrostatic repulsion at pH = 10 [267], when also OH^- ions likely compete with TRZ ions for positively charged adsorbing sites [266]. Accordingly, after 30 min under UV light, discoloration (Figure 6-6a) was *ca.* 95, 70 and 25 % at pH = 3.0, 6.4 and 10.0, respectively. Such behavior agrees with previous results regarding TRZ discoloration by photo-Fenton reaction with perovskites-based photocatalysts [268].

After 3h under UV irradiation, TOC removal was *ca.* 55, 100 and 3.0 % at pH = 3.0, 6.4 and 10.0, respectively (Figure 6-6b). The decrease in TOC observed at acidic pH has to be ascribed to a negative effect of low pH values on the Fenton reaction, in that excess H^+ species "consume" HO· radicals producing water [266]:

$$HO\cdot + H^+ + e^- \rightarrow H_2O \qquad (6-10)$$

On the other hand, by increasing pH to 10.0, H_2O_2 concentration in the liquid increases due to the higher stability of H_2O_2 in alkaline conditions, and consequently the photo-Fenton performance decreases, due to a limited photolytic production of HO· radicals [234, 260].

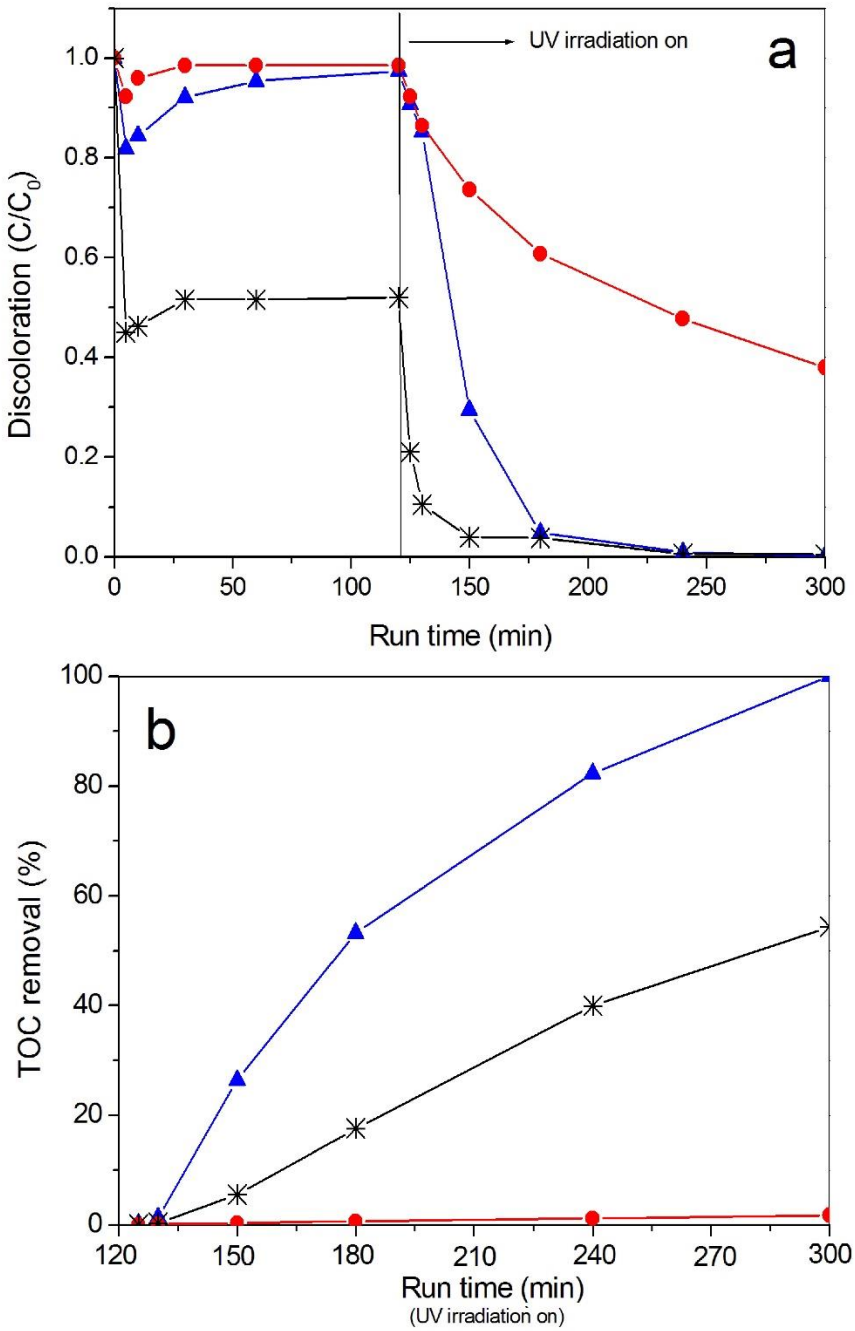

Figure 6-6: Influence of initial pH on a) discoloration and (b) mineralization of TRZ at pH = 6.4 (triangles), pH = 3.0 (stars) and pH = 10.0 (circles) with 0.25 g L^{-1} Fe-0.70-MeIMO-IE catalyst (initial dye concentration: 40 ppm; H_2O_2 flow rate: 0.038 mol h^{-1})

6.4 Conclusions

Fe-doping of methyl-imogolite has been obtained by ionic exchange of preformed nanotubes. Such process led to enhanced properties towards the photo-Fenton oxidation of tartrazine, an important pollutant of both wastewater and groundwater, as the moieties is a common food dye recalcitrant to biodegradation.

At low Fe content (*i.e.* 0.70 wt. % Fe), isomorphic substitution of Al^{3+} by Fe^{3+} is the main process occurring during ionic exchange, leading to a material containing isolated Fe^{3+} sites within the nanotube structure, able to provide total discoloration and mineralization of tartrazine after 3 h under UV irradiation, when a catalyst concentration of 0.25 g L^{-1} is used.

At higher Fe content (*i.e.* 1.4 wt. % Fe) the higher amount of Fe oxo-hydroxide clusters, likely located at the outer surface of nanotubes, has a detrimental effect on tartrazine mineralization. This is due to both a lower photo-Fenton activity of the clusters with respect to isolated Fe^{3+} species and their ability to catalyze the (undesired) decomposition of H_2O_2 to oxygen and water.

Interestingly, bare methyl-imogolite is also active towards tartrazine removal in the presence of H_2O_2, due to the formation of reactive Al-OOH groups (after reaction of H_2O_2 with the outer surface of nanotubes), which under UV irradiation promptly release HO· radicals able to attack the dye.

Tartrazine removal was studied also in the presence of the buckled phases stemming from nanotubes thermal collapse: they still showed a remarkable surface area, mainly due to micropores volume, and reached a TOC removal of *ca.* 80-90 % after 3h under UV irradiation. Such result was ascribed to the presence of new coordination environments for both Al and Fe sites, leading in the latter case to new Fe^{3+} sites embedded in the microporous aluminosilicate, which resulted active towards the photo-Fenton reaction.

Appendix

7.1 Methods of Analysis

XRD (Powder X-ray diffraction)

Place of analysis: Polytechnic University of Turin (Italy)

Powder X-Ray Diffraction (XRD) patterns were obtained on a X'Pert Phillips diffractometer operating with Cu Ka radiation (1.541874 Å) in the 2.5 – 25° 2θ range (step width = 0.02˚; time per step = 2.00 s).

BET (Brunauer- Emmett-Teller Specific Surface Area**)**

Place of analysis: Polytechnic University of Turin (Italy)

To determine BET SSA (Brunauer- Emmett-Teller Specific Surface Area) and porous volume, N_2 isotherms were measured at -196 °C on samples previously outgassed at 250 °C, a temperature allowing the removal of water (and other atmospheric contaminants) preserving NTs structure [8, 25, 143]. Microporous volume was calculated according to the *t*-plot method. NL-DFT (Non Local Density Functional Theory) method was used to determine Pores Size Distributions (PSDs), by applying a N_2-silica kernel for cylindrical pores on isotherms adsorption branch, microporous surface area and total SSA.

UV-vis spectroscopy (Ultraviolet–visible spectroscopy)

Place of analysis: Polytechnic University of Turin (Italy)

Diffuse Reflectance (DR) UV-Vis spectra of out-gassed samples were measured on a Cary 5000 UV-Vis-NIR spectrophotometer (Varian instruments).

Zeta Potential

Place of analysis: Polytechnic University of Turin (Italy)

Samples electrophoretic mobility as a function of pH was measured at 25°C by means of electrophoretic light scattering technique on a Zetasizer Nano-ZS (Malvern Instruments, Worcestershire, UK). The ζ-potential curves were measured by Henry's equation: $U_E = 2\varepsilon \zeta f(Ka)/3\eta$, where U_E is the electrophoretic mobility, ε is the dielectric constant, ζ is the zeta potential, f(Ka) is the Henry's function and η is the viscosity. In aqueous solutions of moderate electrolyte concentration, a value of f(Ka) equal to 1.5 is adopted, in agreement with the Smoluchowski's approximation. Water suspensions were sonicated for 2 min with an ultrasonic probe (400 W, 24kHz, UP400S, Hielscher; Germany); the pH of the suspension was then adjusted by adding either 0.10 M HCl or 0.10 M NaOH.

FE-SEM (Field Emission Scanning Electron Microscope)

Place of analysis: polytechnique University of Turin (Italy)

FESEM pictures were collected with a high resolution SEM instrument (LEO 1525) equipped with a Gemini field emission column.

Solid State NMR (Nuclear Magnetic Resonance Spectroscopy)

Place of analysis: ETH University of zürich (Switzerland)

TGA (Thermogravimetric Analysis)

Place of analysis: ETH University of zürich (Switzerland)

TGA analysis was performed on 10 mg sample powder, under Ar flow (rate of Ar flow), with the temperature increasing rate of 10 °C min^{-1} Under Ar flow by SDT 2960 DTA/TGA-MS instrument.

FTIR (Fourier Transform Infrared Spectroscopy)

Place of analysis: ETH University of zürich (Switzerland)

Bruker FT-IR Alpha spectrometer, equipped with OPUS software. Spectra are recorded at resolution <2 cm^{-1}, A typical experiment consisted of the measurement of transmission in 32 scans in the region from 4000 to 1000 cm^{-1}.

Since KBr is ionic compounds does not have any peaks in the related IR spectrum range. The Sample/KBr ratio was used according to standards. About 5 wt% of sample used to make a mixture of KBr and sample powder of about 80 mg. The mixture were well grinded, however it should be noted that an excessive grinding of the potassium bromide is not required. The finely powdered potassium bromide will absorb more humidity (=hygroscopic) from the air and therefore lead to an increased background in certain ranges. The sample powder then treated in 80 °C, 150 °C and 500 °C for 4 h in high vacuum line ($<10^{-4}$ mbar), and transfers to glove box with Ar atmosphere in order to make KBr pellet for FTIR analysis.

HR-TEM (High Resolution Transmission Electron Microscopy)

Place of analysis: ETH University of zürich (Switzerland)

HR-TEM microscopy was carried out using a JEOL 2200FS microscope operated at 200 kV with a point resolution of 0.23nm

EPR (Electron Paramagnetic Resonance)

Place of analysis: ETH University of zürich (Switzerland)

The EPR spectra were recorded with an X-band Bruker EMX (Bruker BioSpin, Rheinstetten, Germany) continuous wave instrument, equipped with a TM (transverse magnetic) type cavity. The spectra were measured at ≈9.7 GHz with a modulation frequency of 100 kHz, modulation amplitudes of 1 G and resolution of 2048. The microwave power applied was 20 mW. The sample temperature in the cavity was controlled with a Eurotherm liquid nitrogen evaporator and heater. *In situ* experiments were carried out in 1 mm quartz tubes at a temperature of -153 °C with the same substrate concentrations as in the batch.

7.2 Post modification of Methyl-imogolite nanotubes with plasma

A simple test on post modification of MeIMO nanotubs, done during my collaboration research with ETH university of Zürich. The process performed on MeMO samples, preheated at 200 °C for 4 h under vacuum, to insure the total surface dehydration of NTs. About 15 mg of dried powder was placed on the Ar plasma cell and the cell purged with Ar for about 30 min in order to remove the residual air. The instrument then programmed for using the Ar plasma with 200 V power on two samples, once for 80 seconds and another time for 240 seconds.

After plasma treatment, samples were analyzed by EPR after about an hour. The organic radicals were observed in both samples with higher intensity in sample exposed for 240 s to Ar plasma (arrows in the Figure 7-1).

The samples then analyzed with XRD, which confirmed the structure of NTs were maintained due to the presence of three characteristic peaks of imogolite type nanotubes.

This observation opens the possibility for selective surface modification of NTs by exposing the plasma treated NTs to corresponding modification agent.

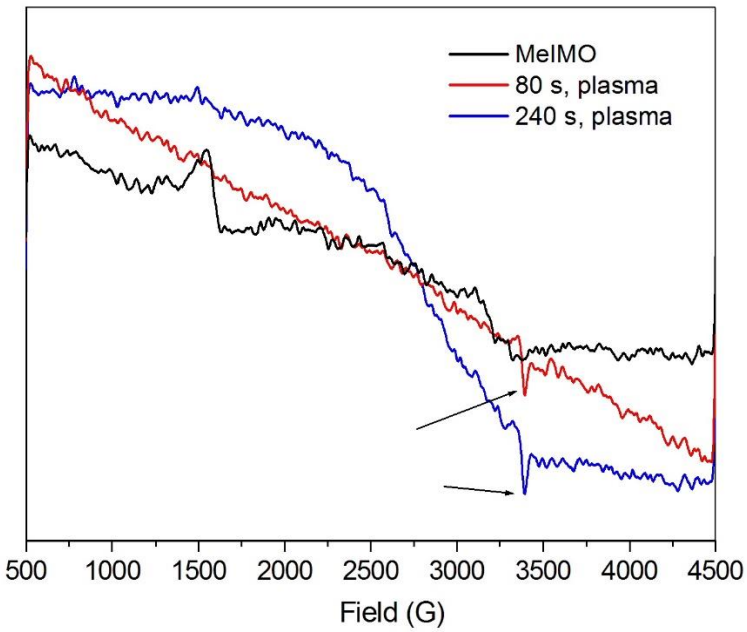

Figure 7-1: EPR spectra of MeIMO (black curve), MeMO exposed to Ar plasma for 80 s (red curve) and MeIMO exposed to Ar plasma for 240 s (blue curve) at -153 °C

7.3 Index

3-APTES: 3-aminopropylsilane, $NH_2–(CH_2)_3–Si(OEt)_3$

AO7: acid orange 7 dye (NaAO7)

AOPs: Advanced oxidation processes

ATRP: Atom Transfer Radical Polymerization)

ATSB: aluminum-tri-*sec*-butoxide

BET SSA: Brunauer- Emmett-Teller Specific Surface Area

CBE: Conduction Band Energy

CNTs: Carbon Nanotubes

CT: Charge-Transfer

DTG: Derivative Thermogravimetric

DWNT: Double Wall Nanotube

e-h separation: electron-hole separation

EDX: Energy Dispersive X-Ray

EPR: Electron Paramagnetic Resonance

FE-SEM: Field Emission Scanning Electron Microscope

FTIR spectroscopy: Fourier Transform Infrared spectroscopy

Fe-x-MeIMO-DS: Fe-doped MeIMO NTs, by Direct Synthesis (x= 0.7 and 1.4 wt% of Fe)

Fe-x-MeIMO-IE: Fe-doped MeIMO NTs, by Ion Exchange (x= 0.7 and 1.4 wt% of Fe)

Fe-x-MeIMO-DS-c: Fe-doped MeIMO NTs, by Direct Synthesis (x= 0.7 and 1.4 wt% of Fe), collapsed

Fe-x-MeIMO-IE-c: Fe-doped MeIMO NTs, by Ion Exchange (x= 0.7 and 1.4 wt% of Fe), collapsed

HB: Hydrogen Bonded

HR-TEM: High resolution-transition electron microscopy

ICP-AES: Inductively coupled plasma atomic emission spectroscopy

Imo: Imogolite:

IS: Isomorphic Substitution

LFO perovskite: Lanthanum ferrite perovskite

l.t. : low temperature

MeIMO: Methy-imogolite

MeIMO-c: Methy-imogolite-collapsed

MAS NMR: Magnetic Angles Spinning- Nuclear Magnetic Resonance

NT(s): Nanotube(s)

NL-DFT: Non Local Density Functional Theory Method

NH_2-MeIMO: (MeIMO react with 3-APTES)

ODPA: Octadecyl Phosphonic Acid

Oh: Octahedral

PZC: Point of Zero Charge

PZNC: Point of Zero Net Charge

PSDs: Pores Size Distributions

r.t. : room temperature

SAED pattern: Selected Area Electron Diffraction

SSA: Specific surface area

SWNT: Single Wall Nanotube

Tartarazine: TRZ dye

Td: Tetrahedral

TEOG: Tetraethoxygermanium

TEOS : Tetraethyl orthosilicate

TEMS : Triethoxymethylsilane

TGA: Thermogravimetric Analysis

TDPA:. Tetradecyl Phosphonic Acid

TOC: Total Organic Carbon

UV-Vis spectroscopy: Ultraviolet–visible spectroscopy

VBE: Valance Band Energy

X XRD: Powder X-ray diffraction

ZFS: Zero-Field Splitting

References

1. Bates, T.F., Sand, L.B., and Mink, J.F., (1950), Tubular crystals of chrysotile asbestos. *Science*. 111: pages 512-513.
2. Cradwick, P.D.G., Farmer, V.C., Russell, J.D., Masson, C.R., Wada, K., and Yoshinaga, N., (1972), Imogolite, a Hydrated Aluminium Silicate of Tubular Structure. *Nat Phys Sci Nature Physical Science*. 240: pages 187-189.
3. Iijima, S., (1991), Helical microtubules of graphitic carbon. *Nature*. 354: pages 56-58.
4. Annabi-Bergaya, F., (2008), Layered clay minerals. Basic research and innovative composite applications. *Microporous and Mesoporous Materials*. 107: pages 141-148.
5. Schoonheydt, R.A. and Bergaya, F., (2011), Advances in the Characterization of Industrial Minerals. Industrial clay minerals as nanomaterials. Vol. 9, Ireland: The Europeans Mineralogical Union and the Mineralogical Society of Great Britain.
6. Ma, W., Otsuka, H., and Takahara, A., (2011), Preparation and properties of PVC/PMMA-g-imogolite nanohybrid via surface-initiated radical polymerization. *Polymer*. 52: pages 5543-5550.
7. Yah, W.O., Yamamoto, K., Jiravanichanun, N., Otsuka, H., and Takahara, A., (2010), Imogolite Reinforced Nanocomposites: Multifaceted Green Materials. *Materials*. 3: pages 1709-1745.
8. Bonelli, B., Bottero, I., Ballarini, N., Passeri, S., Cavani, F., and Garrone, E., (2009), IR spectroscopic and catalytic characterization of the acidity of imogolite-based systems. *Journal of Catalysis*. 264: pages 15-30.
9. Bottero, I., Bonelli, B., Ashbrook, S.E., Wright, P.A., Zhou, W., Tagliabue, M., Armandi, M., and Garrone, E., (2011), Synthesis and characterization of hybrid organic/inorganic nanotubes of the imogolite type and their behaviour towards methane adsorption. *Phys Chem Chem Phys*. 13: pages 744-50.

10. Kang, D.-Y., Zang, J., Jones, C.W., and Nair, S., (2011), Single-Walled Aluminosilicate Nanotubes with Organic-Modified Interiors. *The Journal of Physical Chemistry C*. 115: pages 7676-7685.

11. Zanzottera, C., Vicente, A., Celasco, E., Fernandez, C., Garrone, E., and Bonelli, B., (2012), Physico-Chemical Properties of Imogolite Nanotubes Functionalized on Both External and Internal Surfaces. *The Journal of Physical Chemistry C*. 116: pages 7499-7506.

12. Yoshinaga, N. and Aomine, S., (1962), Imogolite in some ando soils. *Soil Science and Plant Nutrition*. 8: pages 22-29.

13. Su, B.L., Roussel, M., Vause, K., Yang, X.Y., Gilles, F., Shi, L., Leonova, E., Edén, M., and Zou, X., (2007), Organic group-bridged hybrid materials with a Faujasite X zeolite structure (ZOF-X). *Microporous and Mesoporous Materials*. 105: pages 49-57.

14. Park, S., Lee, Y., Kim, B., Lee, J., Jeong, Y., Noh, J., Takahara, A., and Sohn, D., (2007), Two-dimensional alignment of imogolite on a solid surface. *Chemical Communications*: pages 2917-2919.

15. Denaix, L., Lamy, I., and Bottero, J.Y., (1999), Structure and affinity towards Cd^{2+}, Cu^{2+}, Pb^{2+} of synthetic colloidal amorphous aluminosilicates and their precursors *Colloids and Surfaces A*. 158: pages 315-325.

16. Clark, C.J. and McBride, M.B., (1984), Chemisorption of Cu(II) and Co(II) on allophane and imogolite. *Clays and Clay Minerals*. 32: pages 300-311.

17. Parfitt, R.L., Thomas, A.D., Atkinson, R.J., and Smart, R.S.C., (1974), Adsorption of Phosphate on Imogolite. *Clays and Clay Minerals*. 22: pages 1.

18. Arai, Y., McBeath, M., Bargar, J.R., Joye, J., and Davis, J.A., (2006), Uranyl adsorption and surface speciation at the imogolite–water interface: Self-consistent spectroscopic and surface complexation models. *Geochimica et Cosmochimica Acta*. 70: pages 2492-2509.

19. Harsh, J.B., Traina, S.J., Boyle, J., and Yang, Y., (1992), Adsorption of cations on imogolite and their effect on surface charge characteristics. *Clays and Clay Minerals*. 40: pages 700-706.

20. Alvarez-Ramírez, F., (2009), First Principles Studies of Fe-Containing Aluminosilicate and Aluminogermanate Nanotubes. *Journal of Chemical Theory and Computation*. 5: pages 3224-3231.

21. Ookawa, M., (2012), Synthesis and Characterization of Fe-Imogolite as an Oxidation Catalyst. Clay Minerals in Nature - Their Characterization, Modification and Application. InTech.

22. Ookawa, M., Inoue, Y., Watanabe, M., Suzuki, M., and Yamaguchi, T., (2006), Synthesis and Characterization of Fe Containing Imogolite(Soil and

Non-Crystalline Clays,Proceedings of the 13th International Clay Conference). *Clay science*. 12: pages 280-284.

23. Shafia, E., Esposito, S., Armandi, M., Manzoli, M., Garrone, E., and Bonelli, B., (2016), Isomorphic substitution of aluminium by iron into single-walled alumino-silicate nanotubes: A physico-chemical insight into the structural and adsorption properties of Fe-doped imogolite. *Microporous and Mesoporous Materials*. 224: pages 229-238.

24. Shafia, E., Esposito, S., Manzoli, M., Chiesa, M., Tiberto, P., Barrera, G., Menard, G., Allia, P., Freyria, F.S., Garrone, E., and Bonelli, B., (2015), Al/Fe isomorphic substitution versus Fe_2O_3 clusters formation in Fe-doped aluminosilicate nanotubes (imogolite). *Journal of Nanoparticle Research*. 17.

25. Zanzottera, C., Vicente, A., Armandi, M., Fernandez, C., Garrone, E., and Bonelli, B., (2012), Thermal Collapse of Single-Walled Alumino-Silicate Nanotubes: Transformation Mechanisms and Morphology of the Resulting Lamellar Phases. *The Journal of Physical Chemistry C*. 116: pages 23577-23584.

26. da Silva, M.C., dos Santos, E.C., Lourenço, M.P., Gouvea, M.P., and Duarte, H.A., (2015), Structural, Electronic, and Mechanical Properties of Inner Surface Modified Imogolite Nanotubes. *Frontiers in Materials*. 2.

27. Allaoui, A., Bai, S., Cheng, H.M., and Bai, J.B., (2002), Mechanical and electrical properties of a MWNT/epoxy composite. *Composites Science and Technology*. 62: pages 1993-1998.

28. Avouris, P., (2002), Carbon nanotube electronics. *Chemical Physics*. 281: pages 429-445.

29. Balasubramanian, K. and Burghard, M., (2006), Biosensors based on carbon nanotubes. *Analytical and Bioanalytical Chemistry*. 385: pages 452-468.

30. Baughman, R.H., Zakhidov, A.A., and de Heer, W.A., (2002), Carbon Nanotubes--the Route Toward Applications. *Science*. 297: pages 787-792.

31. Ismail, A.F., Goh, P.S., Sanip, S.M., and Aziz, M., (2009), Transport and separation properties of carbon nanotube-mixed matrix membrane. *Separation and Purification Technology*. 70: pages 12-26.

32. Wang, J., Chen, Y., and Blau, W.J., (2009), Carbon nanotubes and nanotube composites for nonlinear optical devices. *Journal of Materials Chemistry*. 19: pages 7425-7443.

33. Popov, V.N., (2004), Carbon nanotubes: properties and application. *Materials Science and Engineering: R: Reports*. 43: pages 61-102.

34. Allen, B.L., Kichambare, P.D., and Star, A., (2007), Carbon nanotube field-effect-transistor-based biosensors. *Advanced Materials*. 19: pages 1439-1451.

35. Zhang, H., Cao, G., and Yang, Y., (2009), Carbon nanotube arrays and their composites for electrochemical capacitors and lithium-ion batteries. *Energy & Environmental Science*. 2: pages 932-943.

36. Whitby, M. and Quirke, N., (2007), Fluid flow in carbon nanotubes and nanopipes. *Nat Nano*. 2: pages 87-94.

37. Holt, J.K., Park, H.G., Wang, Y., Stadermann, M., Artyukhin, A.B., Grigoropoulos, C.P., Noy, A., and Bakajin, O., (2006), Fast Mass Transport Through Sub-2-Nanometer Carbon Nanotubes. *Science*. 312: pages 1034.

38. Zhao, Y.-L. and Stoddart, J.F., (2009), Noncovalent Functionalization of Single-Walled Carbon Nanotubes. *Accounts of Chemical Research*. 42: pages 1161-1171.

39. Singh, S. and Kruse, P., (2008), Carbon nanotube surface science. *International Journal of Nanotechnology*. 5: pages 900-929.

40. Vaisman, L., Wagner, H.D., and Marom, G., (2006), The role of surfactants in dispersion of carbon nanotubes. *Advances in Colloid and Interface Science*. 128–130: pages 37-46.

41. Yuan, P., Tan, D., and Annabi-Bergaya, F., (2015), Properties and applications of halloysite nanotubes: recent research advances and future prospects. *Applied Clay Science*. 112–113: pages 75-93.

42. Lee, D., Maeda, H., Obata, A., Inukai, K., Kato, K., and Kasuga, T., (2013), Aluminum Silicate Nanotube Modification of Cotton-Like Siloxane-poly(L-lactic acid)-vaterite Composites. *Advances in Materials Science and Engineering*. 2013: pages 1-6.

43. Singh, P., Campidelli, S., Giordani, S., Bonifazi, D., Bianco, A., and Prato, M., (2009), Organic functionalisation and characterisation of single-walled carbon nanotubes. *Chemical Society Reviews*. 38: pages 2214-2230.

44. Sun, Y.-P., Fu, K., Lin, Y., and Huang, W., (2002), Functionalized Carbon Nanotubes: Properties and Applications. *Accounts of Chemical Research*. 35: pages 1096-1104.

45. Tenne, R., (2014), Recent advances in the research of inorganic nanotubes and fullerene-like nanoparticles. *Frontiers of Physics*. 9: pages 370-377.

46. Rao, C.N.R. and Govindaraj, A., (2009), Synthesis of Inorganic Nanotubes. *Advanced Materials*. 21: pages 4208-4233.

47. Ferrante, F., Armata, N., and Lazzara, G., (2015), Modeling of the Halloysite Spiral Nanotube. *The Journal of Physical Chemistry C*. 119: pages 16700-16707.

48. Mukherjee, S., Kim, K., and Nair, S., (2007), single-walled mixed-oxide nanotubes assemble from amorphous nanoparticles. *Journal of the American Chemical Society*. 129: pages 6820–6826.

49. Yucelen, G.I., Kang, D.-Y., Guerrero-Ferreira, R.C., Wright, E.R., W., B.H., and Nair, S., (2012), Shaping Single-Walled Metal Oxide Nanotubes from Precursors of Controlled Curvature. *Nano Lett*. 12: pages 5.

50. Kang, D.-Y., Zang, J., Wright, E.R., McCanna, A.L., Jones, C.W., and Nair, S., (2010), Dehydration, Dehydroxylation, and Rehydroxylation of Single-Walled Aluminosilicate Nanotubes. *ACS Nano*. 4: pages 4897-4907.

51. Zang, J., Konduri, S., Nair, S., and Sholl, D.S., (2009), Self-Diffusion of Water and Simple Alcohols in Single-Walled Aluminosilicate Nanotubes. *ACS Nano*. 3: pages 1548-1556.

52. Borrego, T., Andrade, M., Pinto, M.L., Silva, A.R., Carvalho, A.P., Rocha, J., Freire, C., and Pires, J., (2010), Physicochemical characterization of silylated functionalized materials. *Journal of colloid and interface science*. 344: pages 603-610.

53. Liu, J., Wu, S., Zou, M., Zheng, X., and Cai, Z., (2012), Surface modification of silica and its compounding with polydimethylsiloxane matrix: interaction of modified silica filler with PDMS. *Iranian Polymer Journal*. 21: pages 583-589.

54. McMorn, P. and Hutchings, G.J., (2004), Heterogeneous enantioselective catalysts: strategies for the immobilisation of homogeneous catalysts. *Chemical Society Reviews*. 33: pages 108-122.

55. De Vos, D.E., Dams, M., Sels, B.F., and Jacobs, P.A., (2002), Ordered Mesoporous and Microporous Molecular Sieves Functionalized with Transition Metal Complexes as Catalysts for Selective Organic Transformations. *Chemical Reviews*. 102: pages 3615-3640.

56. Choi, J.H., Cho, Y.W., Ha, W.S., Lyoo, W.S., Lee, C.J., Ji, B.C., Han, S.S., and Yoon, W.S., (1998), Preparation and Characterization ofSyndiotacticity-rich Ultra-high MolecularWeight Poly(vinyl alcohol)/ImogoliteBlend Film. *Polymer International* 47: pages 5.

57. Joussein, E., Petit, S., Churchman, J., Theng, B., Righi, D., and Delvaux, B., (2005), Halloysite clay minerals-a review. *Clay Minerals*. 40: pages 383-426.

58. Norrish, R., (1995), An unusual fibrous halloysite. Clays Control the Environment-Proceedings of the 10th international Clay conference Churchman.

59. Yuan, P., Southon, P.D., Liu, Z., Green, M.E.R., Hook, J.M., Antill, S.J., and Kepert, C.J., (2008), Functionalization of Halloysite Clay Nanotubes by Grafting with γ-Aminopropyltriethoxysilane. *The Journal of Physical Chemistry C*. 112: pages 15742-15751.

60. Pasbakhsh, P., Churchman, G.J., and Keeling, J.L., (2013), Characterisation of properties of various halloysites relevant to their use as nanotubes and microfibre fillers. *Applied Clay Science*. 74: pages 47-57.

61. Kamble, R., Ghag, M., Gaikawad, S., and Panda, B.K., (2012), Halloysite nanotubes and applications: A review. *Journal of Advanced Scientific Research*. 3: pages 4.

62. Guimarães, L., Enyashin, A.N., Frenzel, J., Heine, T., Duarte, H.A., and Seifert, G., (2007), Imogolite Nanotubes: Stability, Electronic, and Mechanical Properties. *ACS Nano*. 1: pages 362-368.

63. Bailey, S.W., *Structures of layer silicates*, in *Structures of Clay Minerals and Their X-ray Identification*, G.W. Brindley and G. Brown, Editors. 1980, Mineralogical Society. p. 1-124.

64. Piperno, S., Kaplan-Ashiri, I., Cohen, S.R., Popovitz-Biro, R., Wagner, H.D., Tenne, R., Foresti, E., Lesci, I.G., and Roveri, N., (2007), Characterization of Geoinspired and Synthetic Chrysotile Nanotubes by Atomic Force Microscopy and Transmission Electron Microscopy. *Advanced Functional Materials*. 17: pages 8.

65. Yada, K., (1971), Study of microstructure of chrysotile asbestos by high-resolution electron microscopy. *Acta Crystallographica Section A*. 27: pages 5.

66. Anderson, H.A., Berrow, M.L., Farmer, V.C., Hepburn, A., Russell, J.D., and Walker, A.D., (1982), A reassessment of podzol formation processes. *Journal of Soil Science*. 33: pages 11.

67. Farmer, V.C., (1982), Significance of the presence of allophane and imogolite in podzol bs horizons for podzolization mechanisms: A review. *Soil Science and Plant Nutrition*. 28: pages 571-578.

68. Farmer, V.C., Adams, M.G., Fraser, A.R., and Palmieri, F., (1983), Synthetic Imogolite: Properties, Synthesis, and Possible applications. *Clay Minerals*. 18: pages 459-472.

69. Farmer, V.C., Russell, J.D., and Berrow, M.L., (1980), Imogolite and proto-imogolite allophane in spodic horizons: evidence for a mobile aluminium silicate complex in podzol formation. *Journal of Soil Science*. 31: pages 11.

70. Lumsdon, D.G. and Farmer, V.C., (1997), Solubility of a proto-imogolite sol in oxalate solutions. *European Journal of Soil Science*. 48: pages 5.

71. Wada, K., (1989), Allophane and imogolite. In Minerals in Soil Environments. 2, ed. J.B. Dixon and S.B. Weed. Madison, WI: Soil Science Society of America.

72. Gustafsson, J., Bhattacharya, P., Bain, D., Fraser, A., and McHardy, W., (1995), Podzolisation mechanisms and the synthesis of imogolite in northern Scandinavia. *Geoderma*. 66: pages 167-184.

73. Jongmans, A.G., Verburg, P., Nieuwenhuyse, A., and van Oort, F., (1995), Allophane, imogolite, and gibbsite in coatings in a Costa Rican Andisol. *Geoderma*. 64: pages 327-342.

74. Hoshino, H., Urakawa, H., Donkai, N., and Kajiwara, K., (1996), Simulation of mesophase formation of rodlike molecule, imogolite. *Polymer Bulletin*. 36: pages 257-264.

75. Pohl, P.I., Faulon, J.-L., and Smith, D.M., (1996), Pore Structure of Imogolite Computer Models. *Langmuir*. 12: pages 4463-4468.

76. Barron, P.F., Wilson, M.A., Campbell, A.S., and Frost, R.L., (1982), Detection of imogolite in soils using solid state ^{29}Si NMR. *Nature*. 299: pages 616-618.

77. Karube, J., (1998), Hysteresis of the colloidal stability of imogolite. *Clays and Clay Minerals*. 46: pages 583-585.

78. Ackerman, W.C., Smith, D.M., Huling, J.C., Kim, Y.W., Bailey, J.K., and Brinker, C.J., (1993), Gas/vapor adsorption in imogolite: a microporous tubular aluminosilicate. *Langmuir*. 9: pages 1051-1057.

79. Wilson, M.A., Lee, G.S.H., and Taylor, A.C., (2002), Benzene displacement by water on imogolite. *Clays Clay Minerals*. 50: pages 348-351.

80. Bonelli, B., Armandi, M., and Garrone, E., (2013), Surface properties of alumino-silicate single-walled nanotubes of the imogolite type. *Phys Chem Chem Phys*. 15: pages 13381-90.

81. Wada, S.-i. and Wada, K., (1982), Effects on substitution of germanium for silicon in imogolite. *Clays and Clay Minerals*. 30: pages 123.

82. Wada, S.I., Eto, A., and Wada, K., (1979), Synthetic allophane and imogolite. *Journal of Soil Science*. 30: pages 347-355.

83. Parfitt, R.L. and Henmi, T., (1980), Structure of some allophanes from New Zealand. *Clays and Clay Minerals*. 28: pages 285.

84. Su, C., Harsh, J.B., and Bertsch, P.M., (1992), Sodium and chloride sorption by imogolite and allophanes. *Clays and Clay Minerals*. 40: pages 280.

85. Shafia, E., Esposito, S., Armandi, M., Bahadori, E., Garrone, E., and Bonelli, B., (2015), Reactivity of bare and Fe-doped alumino-silicate nanotubes (imogolite) with H_2O_2 and the azo-dye Acid Orange 7. *Catalysis Today*.

86. Shoji, S., Nanzyo, M., and Dahlgren, R.A., (1994), Volcanic Ash Soils: Genesis, Properties and Utilization. Vol. 21: Elsevier. 287.

87. Gustafsson, J., Lumsdon, D., and Simonsson, M., (1998), Aluminium solubility characteristics of spodic B horizons containing imogolite-type materials. *Clay Minerals*. 33: pages 77-86.

88. Parfitt, R.L., (1990), Allophane in New Zealand - a review. *Australian Journal of Soil Research* 28: pages 17.

89. Henmi, T. and Wada, K., (1976), Morphology and composition of allophane. *American Mineralogist*. 61: pages 379-390.

90. Childs, C.W., Parfitt, R.L., and Newman, R.H., (1990), Structural Studies of Silica Springs Allophane. *Clay Minerals*. 25: pages 12.

91. Childs, C.W., Inoue, K., Seyama, H., Soma, M., Theng, B.K.G., and Yuan, G., (1997), X-Ray Photoelectron Spectroscopic Characterization of Silica Springs Allophane. *Clay Minerals* 32: pages 7.

92. Childs, C.W., Hayashi, S., and Newman, R.H., (1999), Five-Coordinate Aluminum in Allophane. *Clays and Clay Minerals*. 47: pages 5.

93. Koch, C.B., (1998), Structures and properties of anionic clay minerals. *Hyperfine Interactions*. 117: pages 131-157.

94. Farmer, V.C. and Russell, J.D., *Structures and Genesis of Allophanes and Imogolite and their Distribution in Non-Volcanic Soils*, in *Soil Colloids and Their Associations in Aggregates*, M.F. De Boodt, et al., Editors. 1990, Springer US: Boston, MA. p. 165-178.

95. Goodman, B.A., Russell, J.D., Montez, B., Olfield, E., and Kirkpatrick, R.J., (1985), *Phys. Chem. Miner.* .

96. Khan, H., Matsue, N., and Henmi, T., (2007), Adsorption of Water on Nano-Ball Allophane as Affected by Dry Grinding. *International Journal of Soil Science*. 2: pages 10.

97. Montarges-Pelletier, E., Bogenez, S., Pelletier, M., Razafitianamaharavo, A., Ghanbaja, J., Lartiges, B., and Michot, L., (2005), Synthetic allophane-like particles: textural properties. *Colloids and Surfaces A: Physicochemical and Engineering Aspects*. 255: pages 1-10.

98. Yang, H., Wang, C., and Su, Z., (2008), Growth Mechanism of Synthetic Imogolite Nanotubes. *Chemistry of Materials*. 20: pages 4484-4488.

99. Mukherjee, S., Kim, K., and Nair, S., (2007), Short, Highly Ordered, Single-Walled Mixed-Oxide Nanotubes Assemble from Amorphous Nanoparticles. *Journal of the American Chemical Society*. 129: pages 6820-6826.

100. Lee, S.U., Choi, Y.C., Youm, S.G., and Sohn, D., (2011), Origin of the Strain Energy Minimum in Imogolite Nanotubes. *The Journal of Physical Chemistry C*. 115: pages 5226-5231.

101. Lee, H., Jeon, Y., Lee, Y., Lee, S.U., Takahara, A., and Sohn, D., (2014), Thermodynamic Control of Diameter-Modulated Aluminosilicate Nanotubes. *The Journal of Physical Chemistry C*. 118: pages 8148-8152.

102. Levard, C., Rose, J., Thill, A., Masion, A., Doelsch, E., Maillet, P., Spalla, O., Olivi, L., Cognigni, A., Ziarelli, F., and Bottero, J.Y., (2010), Formation and Growth Mechanisms of Imogolite-Like Aluminogermanate Nanotubes. *Chemistry of Materials*. 22: pages 2466-2473.

103. Farmer, V.C., Smith, B.F.L., and Tait, J.M., (1979), The stability, free energy and heat of formation of imogolite. *Clay Minerals*. 14: pages 103-107.

104. Wada, S.I., (1987), Imogolite Synthesis at 25°C. *Clays Clay Minerals*. 35: pages 5.

105. Arancibia-Miranda, N., Escudey, m., Molina, M., and García-González, M.T., (2013), Kinetic and Surface Study of Single-Walled Aluminosilicate Nanotubes and Their Precursors. *Nanomaterials*. 3: pages 4.

106. Farmer, V.C. and Fraser, A.R., *Synthetic Imogolite, A Tubular Hydroxyaluminium Silicate*, in *Developments in Sedimentology*, M.M. Mortland and V.C. Farmer, Editors. 1979, Elsevier. p. 547-553.

107. Zanzottera, C., Armandi, M., Esposito, S., Garrone, E., and Bonelli, B., (2012), CO_2 Adsorption on Aluminosilicate Single-Walled Nanotubes of Imogolite Type. *The Journal of Physical Chemistry C*. 116: pages 20417-20425.

108. Konduri, S., Tong, H.M., Chempath, S., and Nair, S., (2008), Water in Single-Walled Aluminosilicate Nanotubes: Diffusion and Adsorption Properties. *The Journal of Physical Chemistry C*. 112: pages 15367-15374.

109. Ohashi, F., Tomura, S., Akaku, K., Hayashi, S., and Wada, S.I., (2004), Characterization of synthetic imogolite nanotubes as gas storage. *Journal of Materials Science*. 39: pages 1799-1801.

110. Thill, A., Maillet, P., Guiose, B., Spalla, O., Belloni, L., Chaurand, P., Auffan, M., Olivi, L., and Rose, J., (2012), Physico-chemical control over the single- or double-wall structure of aluminogermanate imogolite-like nanotubes. *J Am Chem Soc*. 134: pages 3780-6.

111. Mukherjee, S., Bartlow, V.M., and Nair, S., (2005), Phenomenology of the Growth of Single-Walled Aluminosilicate and Aluminogermanate Nanotubes of Precise Dimensions. *Chemistry of Materials*. 17: pages 4900-4909.

112. Konduri, S., Mukherjee, S., and Nair, S., (2007), Controlling Nanotube Dimensions: Correlation between Composition, Diameter, and Internal Energy of Single-Walled Mixed Oxide Nanotubes. *ACS Nano*. 1: pages 393-402.

113. Amara, M.-S., Paineau, E., Bacia-Verloop, M., Krapf, M.-E.M., Davidson, P., Belloni, L., Levard, C., Rose, J., Launois, P., and Thill, A., (2013), Single-step formation of micron long $(OH)_3Al_2O_3Ge(OH)$ imogolite-like nanotubes. *Chemical Communications*. 49: pages 11284-11286.

114. Lourenço, M.P., Guimarães, L., da Silva, M.C., de Oliveira, C., Heine, T., and Duarte, H.A., (2014), Nanotubes With Well-Defined Structure: Single- and Double-Walled Imogolites. *The Journal of Physical Chemistry C*. 118: pages 5945-5953.

115. Bonelli, B., Zanzottera, C., Armandi, M., Esposito, S., and Garrone, E., (2013), IR spectroscopic study of the acidic properties of alumino-silicate single-walled nanotubes of the imogolite type. *Catalysis Today*. 218-219: pages 3-9.

116. Kang, D.-Y., Brunelli, N.A., Yucelen, G.I., Venkatasubramanian, A., Zang, J., Leisen, J., Hesketh, P.J., Jones, C.W., and Nair, S., (2014), Direct synthesis of single-walled aminoaluminosilicate nanotubes with enhanced molecular adsorption selectivity. *Nat. Commun.* 5.

117. Amara, M.S., Paineau, E., Rouzière, S., Guiose, B., Krapf, M.-E.M., Taché, O., Launois, P., and Thill, A., (2015), Hybrid, Tunable-Diameter, Metal Oxide Nanotubes for Trapping of Organic Molecules. *Chemistry of Materials*. 27: pages 1488-1494.

118. Ma, W., Yah, W.O., Otsuka, H., and Takahara, A., (2012), Application of imogolite clay nanotubes in organic-inorganic nanohybrid materials. *Journal of Materials Chemistry*. 22: pages 11887-11892.

119. Yamamoto, K., Otsuka, H., Wada, S.-I., Sohn, D., and Takahara, A., (2005), Preparation and properties of [poly(methyl methacrylate)/imogolite] hybrid via surface modification using phosphoric acid ester. *Polymer*. 46: pages 12386-12392.

120. Johnson, L.M. and Pinnavaia, T.J., (1991), Hydrolysis of (.gamma.-aminopropyl)triethoxysilane-silylated imogolite and formation of a silylated tubular silicate-layered silicate nanocomposite. *Langmuir*. 7: pages 2636-2641.

121. Qi, X., Yoon, H., Lee, S.-H., Yoon, J., and Kim, S.-J., (2008), Surface-modified imogolite by 3-APS–OsO_4 complex: Synthesis, characterization and its application in the dihydroxylation of olefins. *Journal of Industrial and Engineering Chemistry*. 14: pages 136-141.

122. Johnson, L.M. and Pinnavaia, T.J., (1990), Silylation of a tubular aluminosilicate polymer (imogolite) by reaction with hydrolyzed (.gamma.-aminopropyl)triethoxysilane. *Langmuir*. 6: pages 307-311.

123. Ma, W., Yah, W.O., Otsuka, H., and Takahara, A., (2012), Surface functionalization of aluminosilicate nanotubes with organic molecules. *Beilstein journal of nanotechnology*. 3: pages 82-100.

124. Bonelli, B., Bottero, I., and Garrone, E. Italy.

125. Park, G., Lee, H., Lee, S.U., and Sohn, D., (2014), Strain Energy and Structural Property of Methyl Substituted Imogolite. *Molecular Crystals and Liquid Crystals*. 599: pages 68-71.

126. Elliott, J.D., Poli, E., Scivetti, I., Ratcliff, L.E., Andrinopoulos, L., Dziedzic, J., Hine, N.D.M., Mostofi, A.A., Skylaris, C.-K., Haynes, P.D., and Teobaldi, G., (2016), Chemically Selective Alternatives to Photoferroelectrics for Polarization-Enhanced Photocatalysis: The Untapped Potential of Hybrid Inorganic Nanotubes. *Advanced Science*

127. Gustafsson, J.P., (2001), The surface chemistry of imogolite. *Clays and Clay Minerals*. 49: pages 73.

128. Zhao, M., Xia, Y., and Mei, L., (2009), Energetic Minimum Structures of Imogolite Nanotubes: A First-Principles Prediction. *The Journal of Physical Chemistry C*. 113.

129. Gilberto, T., Nikolaos, S.B., Andrew, J.F., Francesco, Z., and Werner, A.H., (2009), Hydroxyl vacancies in single-walled aluminosilicate and aluminogermanate nanotubes. *Journal of Physics: Condensed Matter*. 21: pages 195301.

130. Bard, A.J., (1979), Photoelectrochemistry and heterogeneous photo-catalysis at semiconductors. *Journal of Photochemistry*. 10: pages 59-75.

131. Maeda, K., (2013), Z-Scheme Water Splitting Using Two Different Semiconductor Photocatalysts. *ACS Catalysis*. 3: pages 1486-1503.

132. Scanlon, D.O., Dunnill, C.W., Buckeridge, J., Shevlin, S.A., Logsdail, A.J., Woodley, S.M., Catlow, C.R.A., Powell, M.J., Palgrave, R.G., Parkin, I.P., Watson, G.W., Keal, T.W., Sherwood, P., Walsh, A., and Sokol, A.A., (2013), Band alignment of rutile and anatase Ti_{O2}. *Nat Mater*. 12: pages 798-801.

133. Li, G. and Gray, K.A., (2007), The solid–solid interface: Explaining the high and unique photocatalytic reactivity of TiO_2-based nanocomposite materials. *Chemical Physics*. 339: pages 173-187.

134. Cheng, J. and Sprik, M., (2010), Aligning electronic energy levels at the TiO_2/H_2O interface. *Physical Review B*. 82: pages 081406.

135. Bursill, Peng, and Bourgeois, (2000), Imogolite: an aluminosilicate nanotube material. *Philosophical Magazine A*. 80: pages 105-117.

136. Rotoli, B.M., Guidi, P., Bonelli, B., Bernardeschi, M., Bianchi, M.G., Esposito, S., Frenzilli, G., Lucchesi, P., Nigro, M., Scarcelli, V., Tomatis, M., Zanello, P.P., Fubini, B., Bussolati, O., and Bergamaschi, E., (2014), Imogolite: An Aluminosilicate Nanotube Endowed with Low Cytotoxicity and Genotoxicity. *Chemical Research in Toxicology*. 27: pages 1142-1154.

137. Farmer, V.C., Fraser, A.R., and Tait, J.M., (1977), Synthesis of imogolite: a tubular aluminium silicate polymer. *Journal of the Chemical Society, Chemical Communications*: pages 462-463.

138. Zanzottera, C., *Hybrid organic/inorganic nanotubes of imogolite type*, in *Department of Applied Science and Technology*. 2011, Politecnico di Torino: Torino.

139. Sidorkin, V.F., Shagun, V.A., and Pestunovich, V.A., (1999), Stereoelectronic effects and the problem of the choice of model compounds for organic derivatives of a pentacoordinated silicon atom (taking silatranes as an example). *Russian Chemical Bulletin*. 48: pages 1049-1053.

140. Inoue, K. and Huang, P.M., (1984), Influence of citric acid on the natural formation of imogolite. *Nature*. 308: pages 58-60.

141. Koenderink, G.H., Kluijtmans, S.G.J.M., and Philipse, A.P., (1999), On the Synthesis of Colloidal Imogolite Fibers. *Journal of Colloid and Interface Science*. 216: pages 429-431.

142. Karube, J., (1998), Hysteresis of the colloidal stability of imogolite. *Clays and Clay Minerals*. 46: pages 583.

143. MacKenzie, K.J.D., Bowden, M.E., Brown, I.W.M., and Meinhold, R.H., (1989), Structure and Thermal Transformations of Imogolite Studied by ^{29}Si and ^{27}Al High-Resolution Solid-State Nuclear Magnetic Resonance. *Clays and Clay Minerals*. 37: pages 317-324.

144. Thommes, M., Kaneko, K., Neimark Alexander, V., Olivier James, P., Rodriguez-Reinoso, F., Rouquerol, J., and Sing Kenneth, S.W., *Physisorption of gases, with special reference to the evaluation of surface area and pore size distribution (IUPAC Technical Report)*, in *Pure and Applied Chemistry*. 2015. p. 1051.

145. Wada, K., (1977), Minerals in Soil Environments, ed. J.B. Dixon and S.B. Weed. Madison, USA: Soil Science Society of America.

146. Violante, A. and Huang, P.M., (1993), Formation mechanism of aluminium hydroxide polymorphs. *Clays and Clay Minerals*. 41: pages 7.

147. Violante, P., Violante, A., and Tait, J.M., (1982), Morphology of Nordstrandite. *Clays and Clay Minerals*. 30: pages 6.

148. Klinowski, J., Thomas, J.M., Fyfe, C.A., and Hartman, J.S., (1981), Applications of magic-angle-spinning silicon-29 nuclear magnetic resonance. Evidence for two different kinds of silicon-aluminum ordering in zeolitic structures. *The Journal of Physical Chemistry*. 85: pages 2590-2594.

149. Lippmaa, E., Maegi, M., Samoson, A., Tarmak, M., and Engelhardt, G., (1981), Investigation of the structure of zeolites by solid-state high-resolution silicon-^{29}NMR spectroscopy. *Journal of the American Chemical Society*. 103: pages 4992-4996.

150. de Jong, B.H.W.S., Schramm, C.M., and Parziale, V.E., (1984), Polymerization of silicate and aluminate tetrahedra in glasses, melts, and aqueous solutions—V. The polymeric structure of silica in albite and anorthite composition glass and the devitrification of amorphous anorthite. *Geochimica et Cosmochimica Acta*. 48: pages 2619-2629.

151. Kinsey, R.A., Kirkpatrick, R.J., Hower, J., Smith, K.A., and Oldfield, E., (1985), High resolution aluminum-27 and silicon-29 nuclear magnetic resonance spectroscopic study of layer silicates, including clay minerals. *American Mineralogist*. 70: pages 537-548.

152. Fitzgerald, J.J., Murali, C., Nebo, C.O., and Fuerstenau, M.C., (1992), Synthesis, chemical analyses, and solid-state NMR studies of aluminum silicate hydrosols. *Journal of Colloid and Interface Science*. 151: pages 299-316.

153. Amara, M.S., Rouzière, S., Paineau, E., Bacia-Verloop, M., Thill, A., and Launois, P., (2014), Hexagonalization of Aluminogermanate Imogolite Nanotubes Organized into Closed-Packed Bundles. *The Journal of Physical Chemistry C*. 118: pages 9299-9306.

154. Kazuya, Y., Hideyuki, O., Shin-Ichiro, W., and Atsushi, T., (2001), Surface Modification of Aluminosilicate Nanofiber "Imogolite". *Chemistry Letters*. 30: pages 1162-1163.

155. Avellan, A., Levard, C., Kumar, N., Rose, J., Olivi, L., Thill, A., Chaurand, P., Borschneck, D., and Masion, A., (2014), Structural incorporation of iron into Ge–imogolite nanotubes: a promising step for innovative nanomaterials. *RSC Adv*. 4: pages 49827-49830.

156. Shafia, E., *Synthesis and Characterization Of Fe-modified Imogolite Nanotubes*, in *Department of Science and Technology*. 2015, Politecnico di Torino - University of Toronto (Canada). p. 165.

157. Santhosh Kumar, M., Schwidder, M., Grünert, W., Bentrup, U., and Brückner, A., (2006), Selective reduction of NO with Fe-ZSM-5 catalysts of low Fe content: Part II. Assessing the function of different Fe sites by spectroscopic in situ studies. *Journal of Catalysis*. 239: pages 173-186.

158. Masaoki, I., Yamazaki, K., Banno, K., and Shinjoh, H., (2008), Characterization of Fe/ZSM-5 DeNO$_x$ Catalysts Prepared by Different Methods: Relationships between Active Fe Sites and NH3-SCR Performance. *Journal of Catalysis*. 260: pages 205-216.

159. Ma, L., Li, J., Arandiyan, H., Shi, W., Liu, C., and Fu, L., (2012), Influence of calcination temperature on Fe/HBEA catalyst for the selective catalytic reduction of NO$_x$ with NH$_3$. *Catalysis Today*. 184: pages 145-152.

160. Wang, Y., Zhang, Q., Shishido, T., and Takehira, K., (2002), Characterizations of Iron-Containing MCM-41 and Its Catalytic Properties in Epoxidation of Styrene with Hydrogen Peroxide. *Journal of Catalysis*. 209: pages 186-196.

161. Kumar, M.S., Schwidder, M., Grünert, W., and Brückner, A., (2004), On the nature of different iron sites and their catalytic role in Fe-ZSM-5 DeNOx catalysts: new insights by a combined EPR and UV/VIS spectroscopic approach. *Journal of Catalysis*. 227: pages 384-397.

162. Pérez-Ramírez, J., Santhosh Kumar, M., and Brückner, A., (2004), Reduction of N_2O with CO over FeMFI zeolites: influence of the preparation method on the iron species and catalytic behavior. *Journal of Catalysis*. 223: pages 13-27.

163. Kucherov, A.V., Montreuil, C.N., Kucherova, T.N., and Shelef, M., (1998), In situ high-temperature ESR characterization of FeZSM-5 and FeSAPO-34 catalysts in flowing mixtures of NO, C_3H_6, and O_2. *Catalysis Letters*. 56: pages 173-181.

164. Berlier, G., Spoto, G., Bordiga, S., Ricchiardi, G., Fisicaro, P., Zecchina, A., Rossetti, I., Selli, E., Forni, L., Giamello, E., and Lamberti, C., (2002), Evolution of Extraframework Iron Species in Fe Silicalite. *Journal of Catalysis*. 208: pages 64-82.

165. Arieli, D., Vaughan, D.E.W., Strohmaier, K.G., Thomann, H., Bernardo, M., and Goldfarb, D., (1999), Studies of Fe(III) incorporated into $AlPO_4$-20 by X- and W-band EPR spectroscopies. *Magn. Reson. Chem.* 37.

166. Goldfarb, D., Bernardo, M., Stoheimer, K.G., Vaughan, D.E.W., and Tomann, H., (1994), Characterization of iron in zeolites by X-band and Q-

band ESR, pulsed ESR, and UV-Visible spectroscopies. *Journal of the American Chemical Society*. 116: pages 9.

167. Joshi, P.N., Bandyopadhyay, R., Awate, S.V., Shiralkar, V.P., and Rao, B.S., (1994), Influence of physico-chemical parameters on n-hexane dehydrocyclization over Pt/LTL zeolites. *Reaction Kinetics and Catalysis Letters*. 53: pages 231-236.

168. Inui, T., Nagata, H., Takeguchi, T., Iwamoto, S., Matsuda, H., and Inoue, M., (1993), Environments of Iron in Fe-Silicates Synthesized by the Rapid Crystallization Method. *Journal of Catalysis*. 139: pages 482-489.

169. Bruckner, A., Lohse, U., and Mehner, H., (1998), The incorporation of iron ions in $AlPO_4$-5 molecular sieves after microwave synthesis studied by EPR and Mössbauer spectroscopy. *Microporous and Mesoporous Materials*. 20: pages 207-215.

170. Verberckmoes, A.A., Weckhuysen, B.M., Pelgrims, J., and Schoonheydt, R.A., (1995), Diffuse Reflectance Spectroscopy of Dehydrated Cobalt-Exchanged Faujasite-Type Zeolites: A New Method for Co^{2+} Siting. *The Journal of Physical Chemistry*. 99: pages 15222-15228.

171. Borghi, E., Occhiuzzi, M., Foresti, E., Lesci, I.G., and Roveri, N., (2010), Spectroscopic characterization of Fe-doped synthetic chrysotile by EPR, DRS and magnetic susceptibility measurements. *Physical Chemistry Chemical Physics*. 12: pages 227-238.

172. Aasa, R., (1970), Powder Line Shapes in the Electron Paramagnetic Resonance Spectra of High-Spin Ferric Complexes. *The Journal of Chemical Physics*. 52: pages 3919-3930.

173. Wichterlová, B. and Jiru, P., (1980), ESR study of Fe^{3+}-zeolites. *Reaction Kinetics and Catalysis Letters*. 13: pages 197-201.

174. Zysler, R., Fiorani, D., Dormann, J.L., and Testa, A.M., (1994), Magnetic properties of ultrafine α-Fe_2O_3 antiferromagnetic particles. *Journal of Magnetism and Magnetic Materials*. 133: pages 71-73.

175. Suber, L., Fiorani, D., Imperatori, P., Foglia, S., Montone, A., and Zysler, R., (1999), Effects of thermal treatments on structural and magnetic properties of acicular α-Fe_2O_3 nanoparticles. *NanoStructured Materials*. 11: pages 797-803.

176. Kumar, M.S., (2005), On the Nature of Different Fe Sites on Fe Containing Micro and Mesoporous Materials and Their Catalytic Role in the Abatement of Nitrogen Oxides from Exhaust Gases.

177. Mansilla, M.V., Zysler, R., Fiorani, D., and Suber, L., (2002), Annealing effects on magnetic properties of acicular hematite nanoparticles. *Physica B: Condensed Matter*. 320: pages 206-209.

178. Bordiga, S., Buzzoni, R., Geobaldo, F., Lamberti, C., Giamello, E., Zecchina, A., Leofanti, G., Petrini, G., Tozzola, G., and Vlaic, G., (1996), Structure and Reactivity of Framework and Extraframework Iron in Fe-Silicalite as Investigated by Spectroscopic and Physicochemical Methods. *Journal of Catalysis*. 158: pages 486-501.

179. Wilcoxen, J., Arragain, S., Scandurra, A.A., Jimenez-Vicente, E., Echavarri-Erasun, C., Pollmann, S., Britt, R.D., and Rubio, L.M., (2016), Electron Paramagnetic Resonance Characterization of Three Iron–Sulfur Clusters Present in the Nitrogenase Cofactor Maturase NifB from Methanocaldococcus infernus. *Journal of the American Chemical Society*. 138: pages 7468-7471.

180. *Index*, in *Developments in Clay Science*, A.T. Peng Yuan and B. Faïza, Editors. 2016, Elsevier. p. 739-754.

181. Farinha, I., Duarte, P., Pimentel, A., Plotnikova, E., Chagas, B., Mafra, L., Grandfils, C., Freitas, F., Fortunato, E., and Reis, M.A.M., (2015), Chitin–glucan complex production by Komagataella pastoris: Downstream optimization and product characterization. *Carbohydrate Polymers*. 130: pages 455-464.

182. Haddix, G.W., Narayana, M., Gillespie, W.D., Georgellis, M.B., and Wu, Y., (1994), Double rotation and magic-angle spinning NMR study of an ultrastable Y zeolite. *Journal of the American Chemical Society*. 116: pages 672-674.

183. Schmücker, M., MacKenzie, K.J.D., Schneider, H., and Meinhold, R., (1997), NMR studies on rapidly solidified SiO_2-Al_2O_3 and SiO_2-Al_2O_3-Na_2O-glasses. *Journal of Non-Crystalline Solids*. 217: pages 99-105.

184. Akitt, J.W., (1989), Multinuclear studies of aluminium compounds. *Progress in Nuclear Magnetic Resonance Spectroscopy*. 21: pages 1-149.

185. Gilson, J.-P., Edwards, G.C., Peters, A.W., Rajagopalan, K., Wormsbecher, R.F., Roberie, T.G., and Shatlock, M.P., (1987), Penta-co-ordinated aluminium in zeolites and aluminosilicates. *Journal of the Chemical Society, Chemical Communications*: pages 91-92.

186. Farnan, I., Dupree, R., Forty, A.J., Jeong, Y.S., Thompson, G.E., and Wood, G.C., (1989), Structural information about amorphous anodic alumina from ^{27}Al MAS NMR. *Philosophical Magazine Letters*. 59: pages 189-195.

187. Ingram-Jones, V.J., Slade, R.C.T., Davies, T.W., Southern, J.C., and Salvador, S., (1996), Dehydroxylation sequences of gibbsite and boehmite: study of differences between soak and flash calcination and of particle-size effects. *Journal of Materials Chemistry*. 6: pages 73-79.

188. Vitzthum, V., Mieville, P., Carnevale, D., Caporini, M.A., Gajan, D., Coperet, C., Lelli, M., Zagdoun, A., Rossini, A.J., Lesage, A., Emsley, L., and Bodenhausen, G., (2012), Dynamic nuclear polarization of quadrupolar nuclei using cross polarization from protons: surface-enhanced aluminium-27 NMR. *Chemical Communications*. 48: pages 1988-1990.

189. Wischert, R., Florian, P., Copéret, C., Massiot, D., and Sautet, P., (2014), Visibility of Al Surface Sites of γ-Alumina: A Combined Computational and Experimental Point of View. *The Journal of Physical Chemistry C*. 118: pages 15292-15299.

190. Lee, S.K., Park, S.Y., Yi, Y.S., and Moon, J., (2010), Structure and Disorder in Amorphous Alumina Thin Films: Insights from High-Resolution Solid-State NMR. *The Journal of Physical Chemistry C*. 114: pages 13890-13894.

191. Valla, M., Rossini, A.J., Caillot, M., Chizallet, C., Raybaud, P., Digne, M., Chaumonnot, A., Lesage, A., Emsley, L., van Bokhoven, J.A., and Copéret, C., (2015), Atomic Description of the Interface between Silica and Alumina in Aluminosilicates through Dynamic Nuclear Polarization Surface-Enhanced NMR Spectroscopy and First-Principles Calculations. *Journal of the American Chemical Society*. 137: pages 10710-10719.

192. Smith, M.E., Neal, G., Trigg, M.B., and Drennan, J., (1993), Structural characterization of the thermal transformation of halloysite by solid state NMR. *Applied Magnetic Resonance*. 4: pages 157-170.

193. Stebbins, J.F. and Xu, Z., (1997), NMR evidence for excess non-bridging oxygen in an aluminosilicate glass. *Nature*. 390: pages 60-62.

194. Lippmaa, E., Maegi, M., Samoson, A., Engelhardt, G., and Grimmer, A.R., (1980), Structural studies of silicates by solid-state high-resolution silicon-^{29}NMR. *Journal of the American Chemical Society*. 102: pages 4889-4893.

195. Gambuzzi, E., Pedone, A., Menziani, M.C., Angeli, F., Caurant, D., and Charpentier, T., (2014), Probing silicon and aluminium chemical environments in silicate and aluminosilicate glasses by solid state NMR spectroscopy and accurate first-principles calculations. *Geochimica et Cosmochimica Acta*. 125: pages 170-185.

196. Sato, S., Sodesawa, T., Nozaki, F., and Shoji, H., (1991), Solid-state NMR of silica—alumina prepared by chemical vapor deposition. *Journal of Molecular Catalysis*. 66: pages 343-355.

197. Maciel, G.E. and Sindorf, D.W., (1980), Silicon-^{29}NMR study of the surface of silica gel by cross polarization and magic-angle spinning. *Journal of the American Chemical Society*. 102: pages 7606-7607.

198. Moon, J., Taha, M.M.R., Youm, K.-S., and Kim, J.J., (2016), Investigation of Pozzolanic Reaction in Nanosilica-Cement Blended Pastes Based on Solid-State Kinetic Models and ^{29}Si MAS NMR. *Materials*. 9.

199. Tamura, K. and Kawamura, K., (2002), Molecular Dynamics Modeling of Tubular Aluminum Silicate: Imogolite. *The Journal of Physical Chemistry B*. 106: pages 271-278.

200. Creton, B., Bougeard, D., Smirnov, K.S., Guilment, J., and Poncelet, O., (2008), Molecular dynamics study of hydrated imogolite 2. Structure and dynamics of confined water. *Physical Chemistry Chemical Physics*. 10: pages 4879-4888.

201. Iwasaki, M., Yamazaki, K., Banno, K., and Shinjoh, H., (2008), Characterization of Fe/ZSM-5 $DeNO_x$ catalysts prepared by different methods: Relationships between active Fe sites and NH_3-SCR performance. *Journal of Catalysis*. 260: pages 205-216.

202. Blanck, D., Schön, A., Mamede, A.-S., Dujardin, C., Dacquin, J.-P., Granger, P., Paul, J.-F., and Berrier, E., (2017), In situ Raman spectroscopy evidence of an accessible phase potentially involved in the enhanced activity of La-deficient lanthanum orthoferrite in 3-way catalysis (TWC). *Catalysis Today*. 283: pages 151-157.

203. Xin, H., Koekkoek, A., Yang, Q., van Santen, R., Li, C., and Hensen, E.J.M., (2009), A hierarchical Fe/ZSM-5 zeolite with superior catalytic performance for benzene hydroxylation to phenol. *Chemical Communications*: pages 7590-7592.

204. Adebowale, K.O., Unuabonah, E.I., and Olu-Owolabi, B.I., (2008), Kinetic and thermodynamic aspects of the adsorption of Pb^{2+} and Cd^{2+} ions on tripolyphosphate-modified kaolinite clay. *Chemical Engineering Journal*. 136: pages 99-107.

205. Busca, G., (1999), The surface acidity of solid oxides and its characterization by IR spectroscopic methods. An attempt at systematization. *Physical Chemistry Chemical Physics*. 1: pages 723-736.

206. Kalevaru, V.N., Benhmid, A., Radnik, J., Pohl, M.M., Bentrup, U., and Martin, A., (2007), Marked influence of support on the catalytic performance of PdSb acetoxylation catalysts: Effects of Pd particle size, valence states, and acidity characteristics. *Journal of Catalysis*. 246: pages 399-412.

207. Busca, G., (1998), Spectroscopic characterization of the acid properties of metal oxide catalysts. *Catalysis Today*. 41: pages 191-206.

208. Volckmar, C.E., Bron, M., Bentrup, U., Martin, A., and Claus, P., (2009), Influence of the support composition on the hydrogenation of acrolein over $Ag/SiO_2–Al_2O_3$ catalysts. *Journal of Catalysis*. 261: pages 1-8.

209. Baraton, M.I., Merle-Mejean, T., Quintard, P., and Lorenzelli, V., (1990), Surface characterization by FT-IR spectroscopy of an aerogel precursor to cordierite. *The Journal of Physical Chemistry*. 94: pages 5930-5934.

210. Zaki, M., I., Hasan, M., A., Sagheer, F., AL., and Pasupulety, L., (2001), In situ FTIR spectra of pyridine adsorbed on SiO_2-Al_2O_3, TiO_2, ZrO_2 and CeO_2: general considerations for the identification of acid sites on surfaces of finely divided metal oxides. *Colloids and Surfaces A: Physicochemical and Engineering Aspects*. 190.

211. Jankovič, Ľ. and Komadel, P., (2003), Metal cation-exchanged montmorillonite catalyzed protection of aromatic aldehydes with Ac_2O. *Journal of Catalysis*. 218: pages 227-233.

212. Djomgoue, P. and Njopwouo, D., (2013), FT-IR Spectroscopy Applied for Surface Clays Characterization. *Journal of Surface Engineered Materials and Advanced Technology*. 3: pages 7.

213. Madejová, J. and Komadel, P., (2001), baseline studies of the clay minerals society source clays: infrared methods. *Clays and Clay Minerals*. 49: pages 410-432.

214. Parry, E.P., (1963), An infrared study of pyridine adsorbed on acidic solids. Characterization of surface acidity. *Journal of Catalysis*. 2: pages 371-379.

215. (2016), Nanosized Tubular Clay Minerals: Halloysite and Imogolite, ed. A. Thill, P. Yuan, and F. Bergaya. Vol. 7, Developments in Clay Science: Elsevier. 739.

216. Al-Khatib, L., Fraige, F., Al-Hwaiti, M., and Al-Khashman, O., (2012), adsorption from aqueous solution onto natural and acid activated bentonite. *American Journal of Environmental Science*. 5: pages 12.

217. Mall, I.D., Srivastava, V.C., Agarwal, N.K., and Mishra, I.M., (2005), Removal of congo red from aqueous solution by bagasse fly ash and activated carbon: Kinetic study and equilibrium isotherm analyses. *Chemosphere*. 61: pages 492-501.

218. Hsiu-Mei, C., Ting-Chien, C., San-De, P., and Chiang, H.-L., (2009), Adsorption characteristics of Orange II and Chrysophenine on sludge adsorbent and activated carbon fibers. *Journal of hazardous materials*. 161: pages 1384-1390.

219. Khosla, E., Kaur, S., and Dave, P.N., (2013), Mechanistic Study of Adsorption of Acid Orange-7 over Aluminum Oxide Nanoparticles. *Journal of Engineering*. 2013: pages 8.

220. Chiou, M.S. and Li, H.Y., (2003), Adsorption behavior of reactive dye in aqueous solution on chemical cross-linked chitosan beads. *Chemosphere*. 50: pages 1095-1105.

221. Pirillo, S., Pedroni, V., Rueda, E., and Luján Ferreira, M., (2009), Elimination of dyes from aqueous solutions using iron oxides and chitosan as adsorbents: a comparative study. *Química Nova*. 32: pages 1239-1244.

222. Baskaralingam, P., Pulikesi, M., Ramamurthi, V., and Sivanesan, S., (2006), Equilibrium studies for the adsorption of Acid dye onto modified hectorite. *Journal of Hazardous Materials*. 136: pages 989-992.

223. Lata, H., Garg, V.K., and Gupta, R.K., (2008), Adsorptive removal of basic dye by chemically activated Parthenium biomass: equilibrium and kinetic modeling. *Desalination*. 219: pages 250-261.

224. dos Santos, T.C., Zocolo, G.J., Morales, D.A., Umbuzeiro, G.d.A., and Zanoni, M.V.B., (2014), Assessment of the breakdown products of solar/UV induced photolytic degradation of food dye tartrazine. *Food and Chemical Toxicology*. 68: pages 307-315.

225. Gupta, V.K., Jain, R., Nayak, A., Agarwal, S., and Shrivastava, M., (2011), Removal of the hazardous dye—Tartrazine by photodegradation on titanium dioxide surface. *Materials Science and Engineering: C*. 31: pages 1062-1067.

226. Seshadri, S., Bishop, P.L., and Agha, A.M., (1994), Anaerobic-aerobic treatment of selected azo dyes in wastewater. *waste water managment*. 14: pages 10.

227. Jayalakshmi, L., Devadoss, V., and Ananthakumar, K., (2013), Adsorption of Acid Orange-7 Dye onto Activated Carbon Produced from Bentonite - A Study of Equilibrium Adsorption Isotherm. *Chemical Science Transactions*. 2.

228. Abo-Farha, S.A., Badawy, N.A., Emam, A.A., and Moursy, N.M., (2010), *journal of american society*. 10: pages 11.

229. Piumetti, M., Freyria, F.S., Armandi, M., Saracco, G., Garrone, E., Gonzalez, G.E., and Bonelli, B., (2015), Catalytic degradation of Acid Orange 7 by H_2O_2 as promoted by either bare or V-loaded titania under UV light, in dark conditions, and after incubating the catalysts in ascorbic acid. *Catalysis, Structure & Reactivity*. 1: pages 183-191.

230. Freyria, F.S., Bonelli, B., Sethi, R., Armandi, M., Belluso, E., and Garrone, E., (2011), Reactions of Acid Orange 7 with Iron Nanoparticles in Aqueous Solutions. *The Journal of Physical Chemistry C*. 115: pages 24143-24152.

231. Piumetti, M., Freyria, F.S., Armandi, M., Saracco, G., Garrone, E., and Bonelli, B., (2015), Anti-oxidant/pro-oxidant activity of ascorbic acid:

Effect in the degradation of Acid Orange 7 with H_2O_2 catalyzed by transition metal ions *Chemistry Today*. 33: pages 5.

232. Mielczarski, J.A., Atenas, G.M., and Mielczarski, E., (2005), Role of iron surface oxidation layers in decomposition of azo-dye water pollutants in weak acidic solutions. *Applied Catalysis B: Environmental*. 56: pages 289-303.

233. Bauer, C., Jacques, P., and Kalt, A., (2001), Photooxidation of an azo dye induced by visible light incident on the surface of TiO_2. *Journal of Photochemistry and Photobiology A: Chemistry*. 140: pages 87-92.

234. Lane, B.S. and Burgess, K., (2003), Metal-Catalyzed Epoxidations of Alkenes with Hydrogen Peroxide. *Chemical Reviews*. 103: pages 2457-2474.

235. Sepulveda, J., Teixeira, S., and Schuchardt, U., (2007), Alumina-catalyzed epoxidation of unsaturated fatty esters with hydrogen peroxide. *Applied Catalysis A: General*. 318: pages 213-217.

236. Mandelli, D., van Vliet, M.C., Arnold, U., Sheldon, R.A., and Schuchardt, U., (2001), Epoxidation of alkenes with hydrogen peroxide catalyzed by ReO_4–SiO_2· Al_2O_3 and ReO_4–Al_2O_3. *Journal of Molecular Catalysis A: Chemical*. 168: pages 165-171.

237. Wawrzkiewiczi, M. and Hubiki, Z., (2009), Kinetic studies of dyes sorption from aqueous solutions onto the strongly basic anion-exchanger Lewatit MonoPlus M-600. *Chemical Engineering Journal*. 150.

238. Gogate, R.P., Mujumdar, S., and Pandit, B.A., (2002), A Sonophotochemical Reactor for the Removal of Formic Acid from Wastewater. *Industrial & Engineering Chemistry Research*. 41.

239. Laat, J.D. and Gallard, H., (1999), Catalytic Decomposition of Hydrogen Peroxide by Fe(III) in Homogeneous Aqueous Solution: Mechanism and Kinetic Modeling. *Environmental science & technology*. 33: pages 2726.

240. Kwan, W.P. and Voelker, B.M., (2002), Decomposition of hydrogen peroxide and organic compounds in the presence of dissolved iron and ferrihydrite. *Environmental science & technology*. 36: pages 1467-76.

241. Oancea, P. and Meltzer, V., (2013), Photo-Fenton process for the degradation of Tartrazine (E102) in aqueous medium. *Journal of the Taiwan Institute of Chemical Engineers*. 44: pages 990-994.

242. Segneanu, A.E., Lazau, C., Sfirloaga, P., Vlazan, P., Bandas, C., Grozescu, I., and Orbeci, C., (2013), Waste Water Treatment Methods. Water Treatment.

243. Bossmann, S., Oliveros, E., Göb, S., Kantor, M., Göppert, A., Lei, L., Yue, P., L., and Braun, A., M., (2001), Degradation of polyvinyl alcohol (PVA)

by homogeneous and heterogeneous photocatalysis applied to the photochemically enhanced Fenton reaction. *Water Science & Technology*. 44.

244. Martínez, F., Calleja, G., Melero, J.A., and Molina, R., (2007), Iron species incorporated over different silica supports for the heterogeneous photo-Fenton oxidation of phenol. *Applied Catalysis B: Environmental*. 70: pages 452-460.

245. Feng, J., Wong, R., Hu, X., and Yue, P.L., (2004), Discoloration and mineralization of Orange II by using Fe^{3+}-doped TiO_2 and bentonite clay-based Fe nanocatalysts. *Catalysis Today*. 98: pages 5.

246. Sannino, D., Vaiano, V., Isupova, L.A., and Ciambelli, P., (2012), Heterogeneous Photo-Fenton Oxidation of Organic Pollutants on Structured Catalysts. *Journal of Advanced Oxidation Technologies*. 15: pages 294-300.

247. Vaiano, V., Iervolino, G., Sannino, D., Rizzo, L., Sarno, G., Ciambelli, P., and Isupova, L.A., (2015), Food Azo-Dyes Removal from Water by Heterogeneous Photo-Fenton with $LaFeO_3$ Supported on Honeycomb Corundum Monoliths. *Journal of Environmental Engineering*. 141: pages 04015038.

248. Hu, J., Kamali Kannangara, G.S., Wilson, M.A., and Reddy, N., (2004), The fused silicate route to protoimogolite and imogolite. *Journal of Non-Crystalline Solids*. 347: pages 224-230.

249. Suzuki, M., Ohashi, F., Inukai, K., Maeda, M., and Tomura, S., (2000), Synthesis of Allophane and Imogolite from Inorganic Solution Influence of Co-Existing lon Concentration and Titration Rate on Forming Precursor. *Journal of the Clay Science Society of Japan (in Japanese)*. 40: pages 1-14.

250. Levard, C., Masion, A., Rose, J., Doelsch, E., Borschneck, D., Dominici, C., Ziarelli, F., and Bottero, J.-Y., (2009), Synthesis of Imogolite Fibers from Decimolar Concentration at Low Temperature and Ambient Pressure: A Promising Route for Inexpensive Nanotubes. *Journal of the American Chemical Society*. 131: pages 17080-17081.

251. Abidin, Z., Matsue, N., and Henmi, T., (2007), A new method for nano-tube imogolite synthesis. in *Microprocesses and Nanotechnology, 2007 Digest of papers*.

252. Donkai, N., Miyamoto, T., Kokubo, T., and Tanei, H., Preparation of transparent mullite-silica film by heat-treatment of imogolite. *Journal of Materials Science*. 27: pages 6193-6196.

253. Alvarez-Ramírez, F., (2007), Ab initio simulation of the structural and electronic properties of aluminosilicate and aluminogermanate natotubes with imogolite-like structure. *Physical Review B*. 76: pages 125421.

254. Shafia, E., Esposito, S., Bahadori, E., Armandi, M., Manzoli, M., and Bonelli, B., (2016), Synthesis and Characterization of Fe-doped Aluminosilicate Nanotubes with Enhanced Electron Conductive Properties. pages e54758.

255. Sannino, D., Vaiano, V., Ciambelli, P., and Isupova, L.A., (2011), Structured catalysts for photo-Fenton oxidation of acetic acid. *Catalysis Today*. 161: pages 255-259.

256. Singh, B.P., Menchavez, R., Takai, C., Fuji, M., and Takahashi, M., (2005), Stability of dispersions of colloidal alumina particles in aqueous suspensions. *Journal of colloid and interface science*. 291: pages 181-186.

257. Carlson, J. and Kawatra, S., (2013), Factors affecting zeta potential of iron oxides. *Mineral Processing and Extractive Metallurgy Review*. 34: pages 269-303.

258. Kosmulski, M., (2009), pH-dependent surface charging and points of zero charge. IV. Update and new approach. *Journal of Colloid and Interface Science*. 337: pages 439-448.

259. Pardieck, D.L., Bouwer, E.J., and Stone, A.T., (1992), Hydrogen peroxide use to increase oxidant capacity for in situ bioremediation of contaminated soils and aquifers: A review. *Journal of Contaminant Hydrology*. 9: pages 221-242.

260. Kwan, W.P. and Voelker, B.M., (2003), Rates of Hydroxyl Radical Generation and Organic Compound Oxidation in Mineral-Catalyzed Fenton-like Systems. *Environmental Science & Technology* 37.

261. Bonelli, B., Onida, B., Chen, J.D., Galarneau, A., Di Renzo, F., Fajula, F., and Garrone, E., (2004), Spectroscopic characterisation of the strength and stability of the acidic sites of Al-rich microporous micelle-templated silicates. *Microporous and Mesoporous Materials*. 67: pages 95-106.

262. Fu, L., Li, X., Liu, M., and Yang, H., (2013), Insights into the nature of Cu doping in amorphous mesoporous alumina. *Journal of Materials Chemistry A*. 1: pages 14592-14605.

263. Vaiano, V., Isupova, L.A., Ciambelli, P., and Sannino, D., (2014), Photo-fenton Oxidation of t-Butyl methyl ether in Presence of LaFeO3 Supported on Monolithic Structure. *Journal of Advanced Oxidation Technologies*. 17.

264. Wang, Y., Priambodo, R., Zhang, H., and Huang, Y.-H., (2015), Degradation of the azo dye Orange G in a fluidized bed reactor using iron oxide as a heterogeneous photo-Fenton catalyst. *RSC Advances*. 5: pages 45276-45283.

265. Sannino, D., Vaiano, V., Ciambelli, P., and Isupova, L.A., (2013), Mathematical modelling of the heterogeneous photo-Fenton oxidation of

acetic acid on structured catalysts. *Chemical Engineering Journal*. 224: pages 53-58.

266. Banerjee, S. and Chattopadhyaya, M.C., Adsorption characteristics for the removal of a toxic dye, tartrazine from aqueous solutions by a low cost agricultural by-product. *Arabian Journal of Chemistry*.

267. Özcan, A.S., Erdem, B., and Özcan, A., (2004), Adsorption of Acid Blue 193 from aqueous solutions onto Na–bentonite and DTMA–bentonite. *Journal of Colloid and Interface Science*. 280: pages 44-54.

268. Iervolinoa, G., vaiano, V., Sannino, D., Rizzo, L., Sarno, G., Ciambelli, P., and Isupova, L.A., (2015), Influence of operating conditions in the photo-fenton removal of tartrazine on structured catalysts, Chemical Engineering Transactions. *Chemical Engineering Transactions* 43.